

Electronics and Optoelectronics Based on Tellurium

Jiajia Zha, Dechen Dong, Haoxin Huang, Yunpeng Xia, Jingyi Tong, Handa Liu, Hau Ping Chan, Johnny C. Ho, Chunsong Zhao,* Yang Chai,* and Chaoliang Tan*

As a true 1D system, group-VIA tellurium (Te) is composed of van der Waals bonded molecular chains within a triangular crystal lattice. This unique crystal structure endows Te with many intriguing properties, including electronic, optoelectronic, thermoelectric, piezoelectric, chirality, and topological properties. In addition, the bandgap of Te exhibits thickness dependence, ranging from 0.31 eV in bulk to 1.04 eV in the monolayer limit. These diverse properties make Te suitable for a wide range of applications, addressing both established and emerging challenges. This review begins with an elaboration of the crystal structures and fundamental properties of Te, followed by a detailed discussion of its various synthesis methods, which primarily include solution phase, and chemical and physical vapor deposition technologies. These methods form the foundation for designing Te-centered devices. Then the device applications enabled by Te nanostructures are introduced, with an emphasis on electronics, optoelectronics, sensors, and large-scale circuits. Additionally, performance optimization strategies are discussed for Te-based field-effect transistors. Finally, insights into future research directions and the challenges that lie ahead in this field are shared.

1. Introduction

Tellurium (Te) belongs to chalcogenide family, with its discovery dating back to the eighteenth century.^[1,2] While oxygen and sulphur, also members of the chalcogen group, are abundant on Earth, Te is found in extremely small quantities, with its rarity comparable to that of the noble metal platinum (Pt).^[3] Despite its scarcity, Te plays a crucial role in human society. Te has two allotropes that researchers can easily distinguish at a glance: crystalline Te, which appears as a silvery lustrous gray, and amorphous Te, which is brownish-black in color. Bulk Te crystal and crystalline Te nanostructures, including nanobelts, nanoflakes, nanowires, and nanocrystals, have trigonal crystal structures composed of 1D helical Te molecular chains in van der Waals (vdW) stacking. The unique crystal structure of Te compared with those widely available vdW

materials with 2D crystal structures endows Te with many unusual properties and it quickly becomes a hot research topic since its rediscovery. In a single chain, each Te atom covalently bonds with two neighboring atoms, sharing a similar electronic configuration with selenium (Se). Of the six outer electrons distributed in $5s^25p^4$ configurations, two occupy the s-orbital in pair with lower energy, two of the remaining four electrons are distributed at one of the three p-orbitals, while the last two are ready for covalent bonding in half-filled p-orbitals.^[4] Theoretical calculations have predicted three possible crystal phases for monolayer Te: α -Te (1T-MoS₂-like structure), β -Te (metastable tetragonal structure), and γ -Te (2H-MoS₂-like structure). The first two phases have been experimentally demonstrated, while the latter is hypothesized to be unstable at room temperature.^[5–8] Additionally, metallic ϵ - and ζ -phase Te few-layers have been reported in theoretical studies, although they have not yet been synthesized in experiments.^[9,10]

Compared with traditional 3D materials, vdW materials exhibit immunity to surface-induced performance degradation due to the absence of dangling bonds at their surfaces. These materials also provide convenient approaches for constructing functional heterostructures or superlattices for device design and physics research.^[11–18] Furthermore, vdW semiconductors hold great promise for extending Moore's law, thanks to their atomically thin nature.^[19–24] Among vdW semiconductors, the vast majority, represented by the transition metal dichalcogenide (TMD) family, exhibit

J. Zha, D. Dong, C. Tan
Department of Electrical and Electronic Engineering
The University of Hong Kong
Pokfulam Road, Hong Kong, SAR 999077, China
E-mail: chaoltan@cityu.edu.hk, cltan@hku.hk

H. Huang, Y. Xia, J. Tong, H. Liu, H. P. Chan, C. Tan
Department of Electrical Engineering
City University of Hong Kong
Hong Kong, SAR 999077, China

J. C. Ho
Department of Materials Science and Engineering
City University of Hong Kong
Hong Kong, SAR 999077, China

C. Zhao
Huawei Technologies CO., LTD
Shenzhen 518000, China
E-mail: zhaochunsong@hisilicon.com

Y. Chai
Department of Applied Physics
The Hong Kong Polytechnic University
Hung Hom, Kowloon, Hong Kong, SAR 999077, China
E-mail: ychai@polyu.edu.hk

 The ORCID identification number(s) for the author(s) of this article can be found under <https://doi.org/10.1002/adma.202408969>

© 2024 The Author(s). Advanced Materials published by Wiley-VCH GmbH. This is an open access article under the terms of the [Creative Commons Attribution-NonCommercial](#) License, which permits use, distribution and reproduction in any medium, provided the original work is properly cited and is not used for commercial purposes.

DOI: 10.1002/adma.202408969

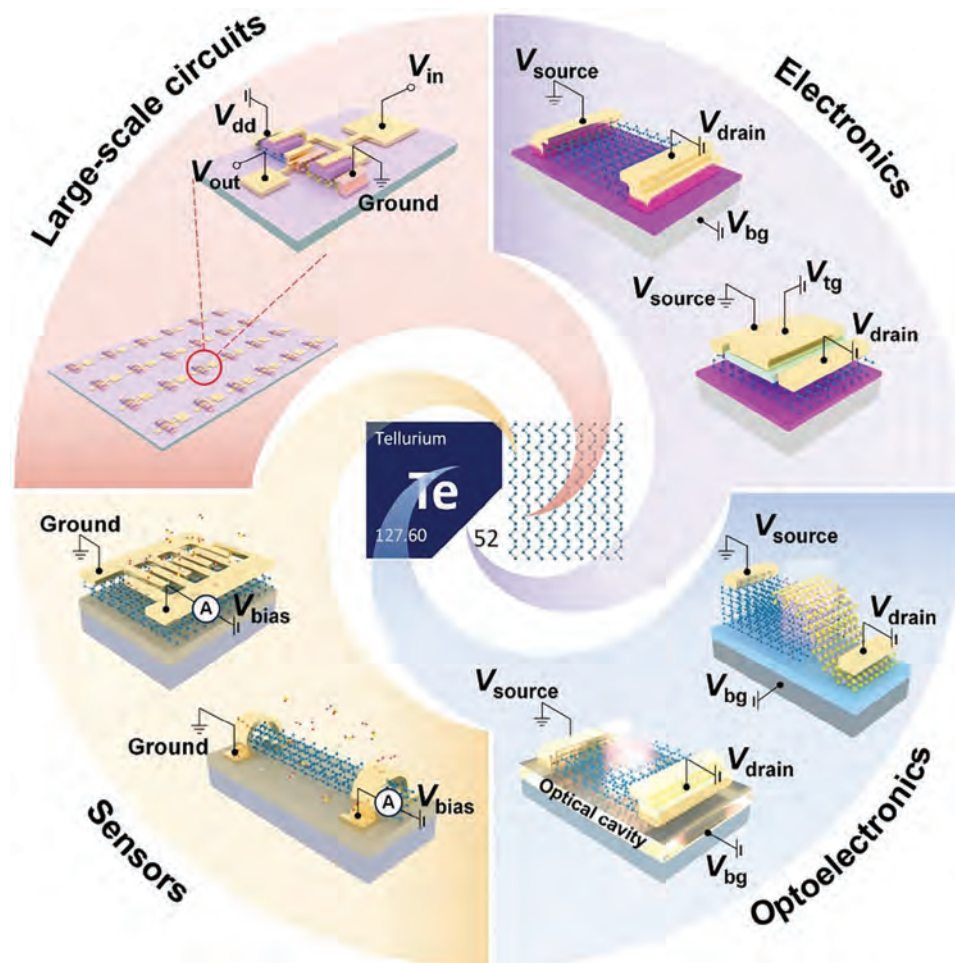


Figure 1. Schematic illustration of advanced electronics and optoelectronics based on Te.

n-type or *p*-type dominant ambipolar transport behaviors at room temperature, while *p*-type counterparts are rarely reported.^[25–28] This significantly hinders the incorporation of vdW materials into commercial integrated circuits. Although black phosphorus (bP) provides an alternative, its application is plagued by rapid degradation under ambient condition.^[29] On the other hand, Te nanostructures, as a stable and natural *p*-type vdW semiconductor with impressive room-temperature hole mobilities up to $\approx 1000 \text{ cm}^2 \text{ V}^{-1} \text{ s}^{-1}$, have been recently re-explored for their potential in future electronics and optoelectronics.^[19,20] In addition to electronic properties,^[30–42] Te nanostructures exhibit a variety of intriguing characteristics, including optoelectronic,^[43–45] optical,^[46–48] thermoelectric,^[49–59] piezoelectric,^[60–64] topological properties,^[65–70] and chirality.^[71–75] Owing to their unique structural features and fascinating properties, various synthesis strategies have been developed to obtain high-quality Te nanostructures, which mainly include hydrothermal method,^[76,77] ultrasonic-assisted synthesis,^[78] liquid-phase exfoliation,^[79] chemical/physical vapor deposition (CVD/PVD) via tubular furnaces,^[80–88] and other PVD methods such as thermal evaporation,^[89–91] molecular beam epitaxy (MBE),^[7,92–94] and magnetron sputtering.^[95,96] The prepared Te nanostructures

have been widely applied in advanced electronics,^[76,80,85,90,97–111] optoelectronics,^[77,81,87,112–124] sensors,^[125–135] and large-scale circuits (Figure 1).^[89,91,95,136,137] In addition, as a special Weyl semiconductor induced by the strong spin-orbit coupling (SOC), Te crystals provide an excellent platform for studying novel physical phenomena.^[102,103] Given the growing interest in Te research, we believe that providing a timely critical Review on this topic for a broad readership will encourage more researchers to engage in this promising field and promote its development.

Herein, we begin by introducing the basic crystal structures and properties of Te, which lay the foundation for subsequent device design. Next, we discuss various synthesis strategies (e.g., hydrothermal method, ultrasonic-assisted synthesis, liquid-phase exfoliation, and CVD/PVD methods) for the preparation of high-quality Te nanostructures, along with their advantages and limitations. Following that, we provide a comprehensive summary of the state-of-the-art Te-based device applications, categorizing them into electronics, optoelectronics, sensors, and large-scale circuits. Finally, taking into account the current progress, we conclude this review by sharing our perspective on the challenges and future prospects in this research field.

2. Properties

Understanding material properties is essential for developing subsequent device designs. The fascinating properties of Te stem from its unique crystal structure. In this section, we begin by elaborating the crystal structures of Te and then introduce its various properties, focusing on the energy band structure and electronic properties, optical properties, piezoelectric properties, thermoelectric properties, and ferroelectric properties. This information will provide our readers with fundamental knowledge and inspire ideas for advanced device designs enabled by Te.

2.1. Crystal Structures

The crystal structure of Te is characterized by Te atomic chains arranged in a triangular helix along the [0001] direction (*z*-axis), where Te atoms form covalent bonds exclusively with their two nearest neighbors (Figure 2a–c). This unique structure results in inherent chirality and high anisotropy in Te. Moreover, the intriguing chain arrangement leads to dangling bonds solely at the (0001) ends of the molecular chains, effectively minimizing carrier recombination at the surfaces and ensuring an extended carrier lifetime.^[138] In the monolayer limit, also known as tellurene, distinct structures emerge, namely α -Te, β -Te, and γ -Te structures (Figure 2d–f). Among these different phases, α -Te and β -Te exhibit room-temperature stability due to their higher cohesive energy (2.62 eV per atom for α -Te and 2.56 eV per atom for β -Te), while γ -Te, with a lower cohesive energy of 2.46 eV per atom, is unstable above 200 K.^[5] Additionally, Yan et al. reported two other ultra-stable novel allotropes of Te few-layers in theoretical calculations, namely metallic ϵ - and ζ -phase Te few layers.^[9,10] These two Te nanocrystals may find applications as the electrodes in vdW devices and offer a platform for studying topological properties once being successfully synthesized in experiments.

The unique trilayer arrangement of Te leads to various intriguing properties of Te atoms in different layers. Te atoms in the central layer, with a higher coordination number (n_c), exhibit metallic characteristics, while the Te atoms in outer layers, with a lower n_c , behave more like a semiconductor.^[5] This nuanced understanding of the structural diversity of Te and the layer number-dependent properties of its constituent Te atoms not only enriches our comprehension of its behavior but also lays the groundwork for leveraging these distinct characteristics in various applications. For a better understanding of lattice vibration in Te, Raman spectra have been studied in different works.^[76,139] Wang et al. fabricated a field-effect transistor (FET) based on single-crystalline Te nanoflakes and studied the thickness-dependent and angle-resolved Raman spectra.^[76] As shown in Figure 2g, the Raman spectra of Te demonstrate distinctive changes with varying thicknesses. Thicker Te nanoflakes (>20.5 nm) exhibit three main Raman-active modes at 92 cm⁻¹ (E_1 transverse (TO) phonon mode), 121 cm⁻¹ (A_1 mode), and 143 cm⁻¹ (E_2 mode), aligning with bulk Te. As thickness decreases (20.5 to 9.1 nm), the E_1 (LO) mode (105 cm⁻¹) appears, originating from the increasing deformation potential and weakening electro-optic effects. Further thickness reduction (<9.1 nm) induces degeneracy in E_1 TO and LO modes with peak broadening, linked to intra-chain atomic displacement, electronic band structure changes, and symmetry assignments.

Thinning also leads to significant blueshifts of A_1 and E_2 modes, distinguishing Te from other vdW materials, by attenuating inter-chain vdW interactions and enhancing intra-chain covalent interactions.^[76] The angle-resolved Raman spectra are depicted in Figure 2h, showing that the intensities of all four modes vary as the incident angle, clearly indicating the reduction of in-plane symmetry in the chiral-chain vdW structure of Te nanoflake. Du et al. further analyzed the Raman spectra under strains at different principle axes.^[139] When applying the strain along the Te atom chain, both A_1 mode and E_2 mode show a blue shift or red shift corresponding to compressive or tensile strains, respectively (Figure 2i–k). However, no significant shift is observed when applying strains perpendicular to the Te atom chain (Figure 2l–n). This direction-dependent phenomenon also can be explained by the anisotropy of the Te crystal structure.

2.2. Energy Band Structure and Electronic Properties

The band structure is a fundamental concept crucial for understanding and predicting the properties of Te. In this section, numerous theoretical calculations, primarily based on first-principles density functional theory (DFT) and ab initio molecular dynamics (MD) simulations, have been conducted to elucidate the layer-dependent, strain-related, and near Dirac-cone shaped bandgap of Te, showcasing its significant potential for applications in electronic and optoelectronic devices. The bandgap of bulk Te was calculated to be 0.21 eV using ab initio MD,^[75] closely matching the experimental result of 0.32 eV.^[42] Additionally, to better understand the properties of low-dimensional Te, Zhu et al. made pioneering predictions on the band structure of monolayer Te using DFT. Their findings, based on Perdew-Burke-Ernzerhof (PBE) + SOC, indicated that α -Te and β -Te exhibit nearly direct or direct band structures at the Γ point, with bandgaps of 0.46 eV and 1.03 eV, respectively, while γ -Te shows metallic properties (Figure 3a).^[5] To deepen the understanding of the band structure of Te, Qiao et al. conducted calculations on the band structure of few-layer α -Te using Vienna ab initio simulations with DFT, employing the screened hybrid functional of Heyd, Scuseria, and Ernzerhof (HSE06) + SOC.^[140] They found that as the layer number of α -Te increased, the bandgap decreased from 1.17 eV for two-layer (2L) α -Te to 0.66 eV for 6L α -Te. Although the bandgap shows variations with different functionals, a consistently common trend has been revealed: The bandgap decreases as the layer number of Te increases (top panel in Figure 3b). This trend has also been confirmed by Wu et al.^[141] Specifically, the valence band maximum (VBM) exhibited significant changes, shifting from -4.98 eV to -4.35 eV, which was roughly three times that of the conduction band minimum (CBM), contributing to the bandgap decrease (bottom panel in Figure 3b). Numerous experimental studies on band structures also align with the calculation results. Chen et al. obtained 5–7-layer β -Te by MBE on highly oriented pyrolytic graphite (HOPG).^[7] Their experimental results, measured by scanning tunneling microscopy (STM), demonstrated that the bandgap decreases from 0.65 eV to 0.53 eV as the layer number increases from 5L to 7L, consistent with previous theoretical calculations. A similar trend was observed in MBE-grown few-layer Te on a graphene/6H-SiC (0001) substrate.^[92] Both

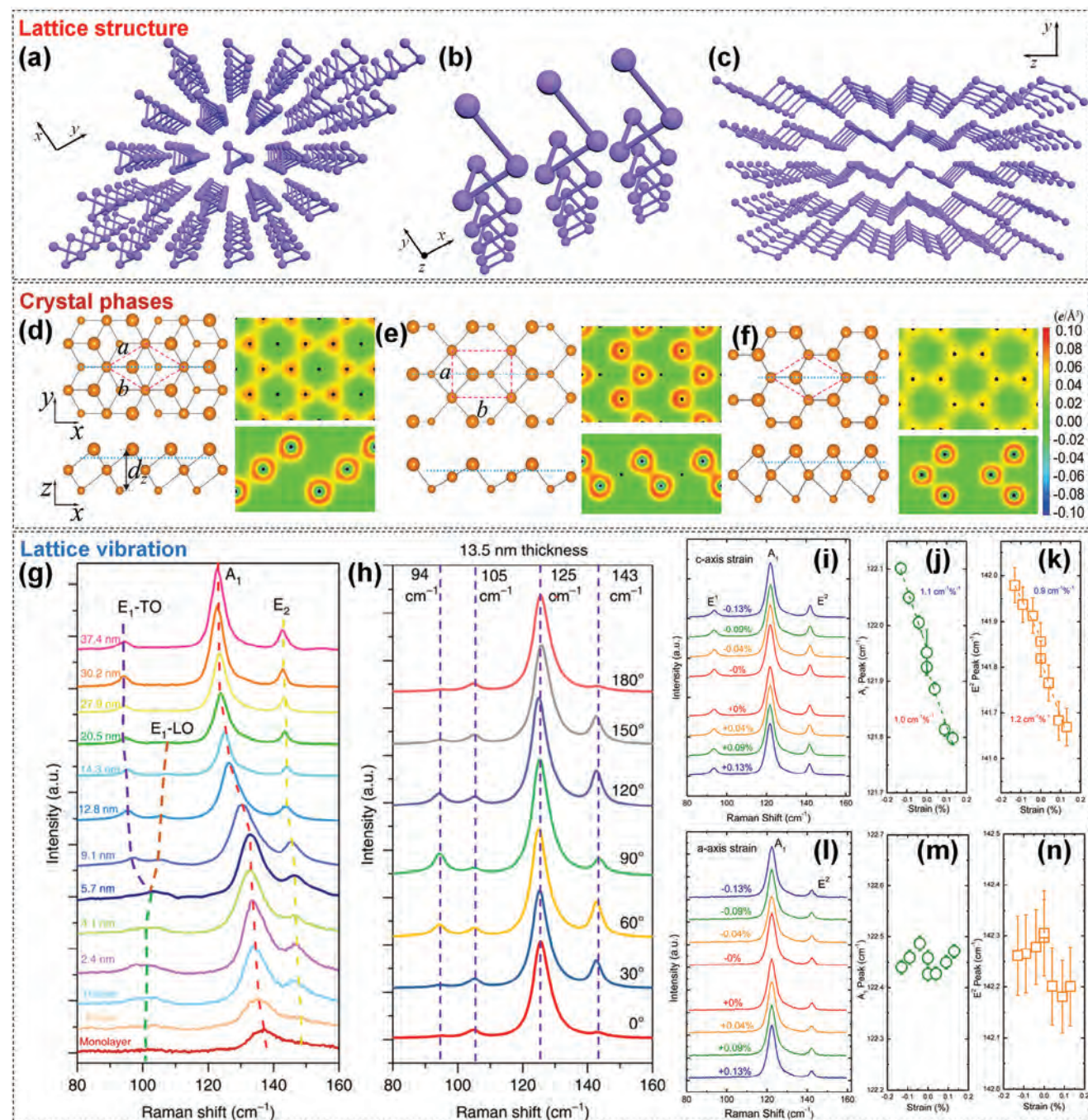


Figure 2. Crystal structures of Te. a–c) Schematic illustration of the Te lattice structure. d–f) Calculated tellurene structures and charge density of α -Te, β -Te, and γ -Te, respectively. Reproduced with permission.^[5] Copyright 2017, The American Physical Society. g) Layer-dependent and h) angle-resolved Raman spectra of a Te nanoflake. Reproduced with permission.^[76] Copyright 2018, Nature Publishing Group. i) Raman spectra of a Te thin film showing Te atom chain strains. Raman shift of j) A_1 and k) E^2 modes in Te under atom chain strain. l) Raman spectra of Te showing vertical atom chain strains. Raman shift of m) A_1 and n) E^2 modes in Te under strain perpendicular to the atom chain. Reproduced with permission.^[139] Copyright 2017, The American Chemical Society.

theoretical calculations and experimental results affirm the same trend, which is the bandgap decreases as the layer number increases. A series of theoretical investigations has consistently projected that strain can induce phase transitions in Te, subsequently influencing its band structure and carrier transport prop-

erties. Xiang et al. delved into the phase transitions of bilayer Te under external strain, uncovering two potential transitions: $\alpha \rightarrow \beta$ and $\alpha \rightarrow \gamma$ phase transition under compressive and tensile strain, respectively, through first-principle calculations.^[142] This strain-induced phase transition illuminates the potential applications

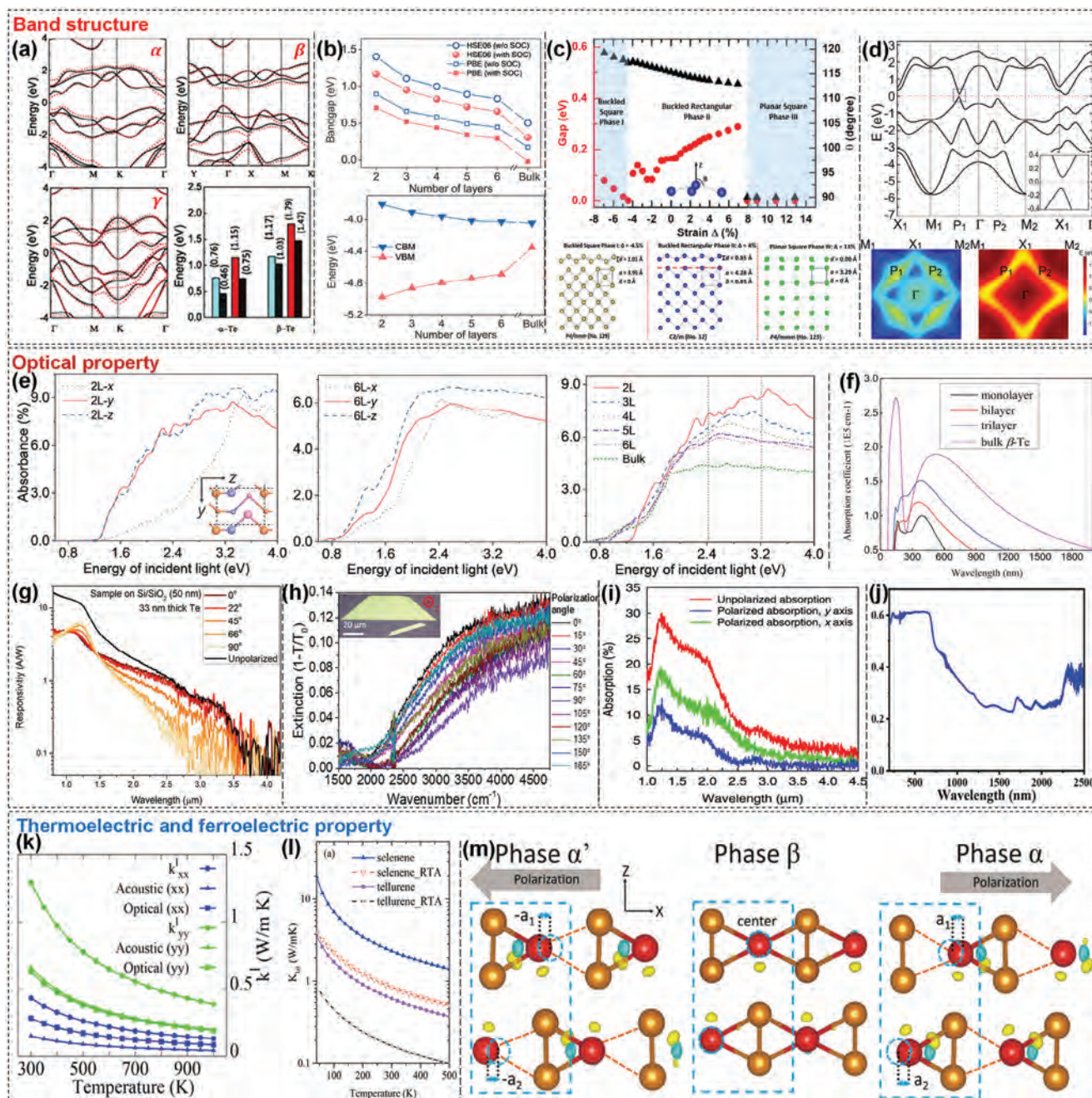


Figure 3. Band structure, optical, thermoelectric, and ferroelectric properties of Te. a) Band structure of α -, β -, γ -Te, with the bandgap illustrated using different functions. Reproduced with permission.^[5] Copyright 2017, The American Physical Society. b) Layer-dependent bandgap and positions of the CBM/VBM. Reproduced with permission.^[140] Copyright 2018, Elsevier. c) Strain-induced bandgap changes due to phase transition. Reproduced with permission.^[143] Copyright 2018, The American Physical Society. d) Band structure of tellurene. Inset: Zoom-in of the band structure in the small region around the semi-Dirac cone at P1, indicated by a blue box. Bottom panel: Band contour for the bottom conduction band and top valence band in the first BZ. Reproduced under the terms of the Creative Commons CC BY license.^[144] Copyright 2017, IOP Publishing Ltd. e) Absorption coefficient of α -Te with varying thicknesses. Reproduced with permission.^[140] Copyright 2018, Elsevier. f) Absorbance of β -Te at different thicknesses. Reproduced with permission.^[141] Copyright 2017, IOP Publishing Ltd. g-j) Absorption spectra of Te thin films from experiments. g) Reproduced with permission.^[77] Copyright 2018, The American Chemical Society. h) Reproduced with permission.^[118] Copyright 2020, The American Chemical Society. i) Reproduced under the terms of the Creative Commons CC BY license.^[151] Copyright 2020, Nature Publishing Group. j) Reproduced with permission.^[152] Copyright 2023, John Wiley & Sons, Inc. k) Lattice thermal conductivity in different directions. Reproduced with permission.^[52] Copyright 2018, The American Chemical Society. l) K_L for Te using the full iterative solution of the Boltzmann equation and the zero-order RTA. Reproduced with permission.^[49] Copyright 2018, The Royal Society of Chemistry. m) Differential charge density of bilayer Te phases, showing layer-center Te atoms (red) and other Te atoms (brown). Reproduced with permission.^[158] Copyright 2018, The Royal Society of Chemistry.

of Te nanostructures as high-performance functional materials in electronics, optoelectronics, and piezoelectronics. Zhang et al. took a step further by directly predicting the feasibility of modulating the bandgap through an external strain-induced phase transition (Figure 3c).^[143] In their work, three different crystal phases of Te have been identified—the buckled square phase I, the buckled rectangular phase II, and the planar square phase III—and they can transition to other phases as the external strain changes. The phase transition and the change of bond length in each phase with the external strain, contribute to the change of bandgap. According to the calculation results provided by Xian et al., tellurene also displays a semi-Dirac cone band structure as shown in top panel in Figure 3d, and anisotropy in ΓP_1 and ΓP_2 direction as shown in bottom panel in Figure 3d, indicating its potential for high mobilities and the polarization-related applications.^[144]

Carrier mobility is another crucial parameter in the study and design of electronic and optoelectronic devices, as it directly influences energy efficiency, speed, thermal noise, and other aspects. Initial calculations have demonstrated that the carrier mobilities of monolayer and few-layer Te can reach thousands of $\text{cm}^2 \cdot \text{V}^{-1} \cdot \text{s}^{-1}$,^[5,140] showcasing an immense potential for the development of high-speed, high-efficiency electronic and optoelectronic devices. Given the anisotropic structure of Te and the calculation results, numerous works report that the carrier mobility exhibits extremely high anisotropic properties along and perpendicular to the Te atom chain.^[37,140] However, there are also theoretical calculation results suggesting that there may be no significant difference in transport properties between directions along and perpendicular to the Te atom chain, which could arise from the comparable effective masses and potentials for charge carriers along different transport directions.^[34,145]

Numerous experimental studies have also been conducted to explore the potential high carrier mobility of Te. In these works, three distinct categories of carrier mobility have been identified: Field-effect mobility, effective mobility, and Hall mobility. Subsequently, we will discuss each of these three distinct types of mobility in detail. Considering the fact that the majority of Te thin films are used in manufacturing FETs, field-effect mobility has become the mainstream characterization method. This characterization is calculated using the following formula.^[146]

$$\mu_{\text{FE}} = \frac{L}{WC_i V_{\text{SD}}} \left(\frac{\partial I_{\text{SD}}}{\partial V_{\text{G}}} \right) \quad (1)$$

at the region of $|V_{\text{G}} - V_{\text{T}}| \gg V_{\text{SD}}$.

L and W are the length and width of the accumulation channel, C_i is the gate-channel capacitance per unit area, V_{SD} , V_{G} , and V_{T} are the source-drain, gate, and threshold voltages, respectively.

For field-effect mobility, various experimental works have been conducted and show a relatively high range of room-temperature field-effect mobility from 700 to 1370 $\text{cm}^2 \cdot \text{V}^{-1} \cdot \text{s}^{-1}$ by selecting proper channel thickness,^[76] forming different morphologies, or choosing dielectric with an atomically flat surface.^[80,93]

Another figure of merit is effective mobility, which can be obtained via the following equation.

$$\mu_{\text{eff}} = \frac{L}{WC_i} \frac{1}{V_{\text{G}} - V_{\text{T}} - V_{\text{SD}}} \left(\frac{\partial I_{\text{SD}}}{\partial V_{\text{SD}}} \right) \quad (2)$$

There are also some reports that apply effective mobility to characterize carrier mobility. Zhao et al. synthesized wafer-scale Te thin films by thermal evaporation at cryogenic temperatures and constructed integrated circuits, achieving an effective mobility of 35 $\text{cm}^2 \cdot \text{V}^{-1} \cdot \text{s}^{-1}$. This relatively low value can be attributed to the abundant defects and grain boundaries in the polycrystalline thin film.^[89] Amani et al. reported a solution-synthesized Te nanoflakes for short-wave infrared (SWIR) photodetectors with an effective mobility of 450 $\text{cm}^2 \cdot \text{V}^{-1} \cdot \text{s}^{-1}$. This significant increase in effective mobility can be explained by the single-crystalline nature of Te nanoflakes.^[77]

Hall mobility refers to a kind of mobility obtained in Hall-effect measurement. Hall mobility can be calculated via Equation 3.^[147]

$$\mu_{\text{Hall}} = \frac{\sigma V_{\text{H}} t}{IB} \quad (3)$$

where V_{H} is the Hall voltage, t is the sample thickness, I and B are the current and magnetic field, which can be measured directly, and σ is the conductivity of the Hall-bar devices. Ren et al. performed an electrolyte-gate transistor and gained a Hall mobility of 500 $\text{cm}^2 \cdot \text{V}^{-1} \cdot \text{s}^{-1}$ in Hall measurements.^[148] We have summarized reported μ_{FE} , μ_{eff} , and μ_{Hall} values in Te thin films in Table 1.

Although field-effect mobilities, effective mobilities, and Hall mobilities are obtained using different methods, all these values can reflect hole transport properties in Te samples under an external electric field. Furthermore, as evidenced in Table 1, the high hole mobility of Te has been consistently verified by various studies. The high carrier mobility reported in Te makes it an ideal candidate for the construction of advanced electronics and optoelectronics with fast response speed.

2.3. Optical Properties

The optical properties of a material are crucial factors to consider when constructing advanced devices, particularly for optoelectronics. Many theoretical studies have been conducted on the absorption spectra of Te to better understand potential device designs based on Te nanostructures. Calculation results reveal a wide absorption spectrum for Te, spanning from ultraviolet to infrared (UV-IR) bands.^[140,141] According to these calculations, α -Te exhibits anisotropic broadband light absorption, reaching up to 1425 nm (0.8 eV) with an extremely high light absorption (as shown in left and middle panels in Figure 3e).^[140] The absorbances of few-layer α -Te (FL- α -Te) are ≈ 2 –3% per layer at 1.6 eV and 6–9% at 3.2 eV (right panel in Figure 3e), respectively, displaying nearly two to three times the absorbance of bP.^[150] Wu et al.'s calculations show that β -Te also has a wide absorption spectrum range, extending to 1100 nm (Figure 3f).^[141] It is worth noting that for both α - and β -Te, as layer thickness increases, the absorbance of each layer decreases; however, the overall light absorption still increases with increasing layer thickness. In experiments, researchers have observed an even broader light absorption band, consistent with the calculated results.^[77,118,151,152] As shown in Figure 3g–j, experimental results indicate that although the cut-off wavelength varies slightly in Te samples

Table 1. Summary of carrier mobilities in Te thin films.

Mobility [$\text{cm}^2 \cdot \text{V}^{-1} \cdot \text{s}^{-1}$]	Mobility category	Synthesis method	Thickness [nm]	Refs.
700	Field-effect mobility	Hydrothermal	16.1	[76]
500	Hall mobility	syntheses	15	[148]
450	Effective mobility		10	[77]
1370	Field-effect mobility	CVD	59	[80]
500	Field-effect mobility		67.6	[87]
145	Field-effect mobility	PVD ^{a)}	—	[85]
35	Effective mobility	Thermal evaporation	8	[89]
182	Effective mobility	Thermal evaporation	19	[90]
30.9	Field-effect mobility	Magnetron sputtering	4	[95]
19	Hall mobility		10	[149]
707	Field-effect mobility	MBE	16	[93]
1000	Field-effect mobility	Solution based	10	[78]

^{a)} PVD used in Table 1, Table 2, and Table 3 refers to the physical vapor deposition in a tubular furnace.

synthesized via different methods, the light absorption capabilities can reach up to 4.6 μm , highlighting the great potential of Te in IR photodetection. Both theoretical calculations and experimental results demonstrate the broad absorption and high absorption coefficient of Te thin films, illustrating the extraordinary potential of Te-based high-performance IR photodetectors with polarization discrimination.

2.4. Piezoelectric Properties

Te displays a significant piezoelectric effect due to its symmetry-breaking nature, which makes it suitable for a wide range of applications in diverse technological fields, such as sensing technologies, energy harvesting, and electronic devices. Comprehensive computational studies reveal that the piezoelectric property is uniquely observed in α -Te with broken symmetry.^[106,153,154] Specifically, Rao's study demonstrates that Te possesses remarkable piezoelectric constants, namely $e_{11} = 130.82 \text{ pC} \cdot \text{m}^{-1}$ and $e_{31} = 5.920 \text{ pC} \cdot \text{m}^{-1}$ for bi-layer Te, as determined by DFT calculations.^[106] These notable piezoelectric constants result from the charge density difference induced by symmetry-breaking. In experimental work, Apet et al. successfully synthesized a $\approx 1\text{-nm}$ Te film and used piezoresponse force microscopy (PFM) to measure the piezoelectric coefficient, obtaining $d_{33} = 1 \text{ pm} \cdot \text{V}^{-1}$.^[154] Both computational and experimental findings highlight exceptional performance of Te in terms of piezoelectric effects, demonstrating its vast potential across various applications, particularly in energy harvesting.

2.5. Thermoelectric Properties

Te also exhibits exceptional thermoelectric properties. To characterize the efficiency of thermoelectric materials, a key parameter known as the figure of merit (ZT) is commonly employed.^[155] The definition of ZT is given by the following equation.

$$ZT = \frac{S^2 \sigma T}{\kappa_E + \kappa_L} \quad (4)$$

where S , σ , κ_E , κ_L , and T are the Seebeck coefficient, electrical conductivity, electronic thermal conductivity, lattice thermal conductivity and absolute temperature, respectively.

It is worth mentioning that since the Seebeck coefficient (S), electrical conductivity (σ), and thermal conductivity (κ_E) are usually correlated through the Wiedemann–Franz law,^[156,157] modifying one parameter often results in compensatory changes in other parameters, presenting a dilemma for significantly enhancing the thermoelectric figure of merit (ZT). Consequently, minimizing lattice thermal conductivity (κ_L) has emerged as a viable strategy for improving ZT.

Several theoretical investigations have explored the exceptional thermoelectric properties of Te, resulting from its low lattice thermal conductivity. Sharma et al. employed first-principles calculations within semiclassical Boltzmann transport theory.^[52] Their findings indicated that monolayer Te exhibited κ_L of 0.43 and $1.29 \text{ W} \cdot \text{m}^{-1} \cdot \text{K}^{-1}$ (Figure 3k), achieving high room-temperature ZT values of 0.80 and 0.38 along the armchair and zigzag directions, respectively. These remarkable thermoelectric properties arise from the effective scattering of acoustic phonons into optical phonons. Anisotropy in thermoelectric properties stems from distinct phonon dispersion and scattering characteristics along different directions.^[52] The calculation results provided by Lin et al. are also consistent with previous work, showing an extremely low room-temperature lattice κ_L (Figure 3l), which is generated from the prominent anharmonic phonon scattering process.^[49] Noteworthy is the observation that the lattice thermal conductivity decreases with increasing temperature due to heightened acoustic-optical phonon scattering at elevated temperatures. Experimental results also confirmed the exceptional thermoelectric properties of Te thin film. By testing the thermoelectrical properties of hydrothermal-synthesized Te thin film, Qiu et al. demonstrated the outstanding thermoelectric performance of Te thin films, with lattice thermal conductivity (κ_L) of $1.50 \text{ W} \cdot \text{m}^{-1} \cdot \text{K}^{-1}$ and ZT value of 0.63, respectively.^[55] The outstanding thermoelectric properties of Te reveal its enormous potential in applications for energy-harvesting devices and photothermoelectric photodetectors.

2.6. Ferroelectric Properties

Te has been predicted to exhibit ferroelectric properties due to its broken symmetry. Theoretical studies, such as the work by Wang et al., have provided insights into the ferroelectric nature of few-layer α -Te using first-principle calculations.^[158] Illustrated in Figure 3m, α -Te displays a significant charge transfer between the central and neighboring Te atoms, along with the separation of positive and negative charge centers resulting from its broken centrosymmetry. This separation of charge centers is a key factor contributing to the ferroelectric property of α -Te. On the other hand, the centrosymmetry of β -Te causes an overlap of positive and negative charge centers, which prevents the material from exhibiting ferroelectric properties. However, it is crucial to note that there is currently a lack of experimental evidence supporting the ferroelectric properties of Te. This gap in knowledge highlights the need for further research efforts to not only validate the ferroelectric aspects of Te but also explore its potential applications.

3. Synthesis Methods

The synthesis of high-quality Te crystals is essential for investigating their physical and chemical properties, as well as enabling their practical applications. In this section, we present a concise overview of six commonly employed synthesis techniques: hydrothermal synthesis, CVD/PVD using a tubular furnace, and other PVD methods such as thermal evaporation, magnetron sputtering, and MBE.

3.1. Hydrothermal Synthesis

Hydrothermal methods have been widely employed for synthesizing Te nanostructures, primarily due to their cost efficiency.^[36,76,77,102,112,118] Figure 4a presents a schematic illustration of the traditional hydrothermal method. Notably, the work by Wang et al. is considered as a seminal study in this field.^[76] Using the hydrothermal method, they successfully synthesized single-crystalline 2D Te nanoflakes and examined the growth mechanism. In their approach, Na_2TeO_3 and polyvinylpyrrolidone (PVP) were initially dissolved in double-distilled water at room temperature under magnetic stirring to form a homogeneous solution. This solution was then transferred into a Teflon-lined stainless-steel autoclave filled with an aqueous ammonia solution and hydrazine hydrate. After a series of heating, cooling, centrifugation, and washing steps, large-sized Te nanoflakes with lengths ranging from 50 to 100 μm and thicknesses from 10 to 100 nm were successfully obtained (Figure 4c,d). Moreover, high-resolution transmission electron microscopy (HRTEM) diffraction patterns (Figure 4e) confirmed that Te nanoflakes tend to grow laterally along the [0001] and [12 $\bar{1}$ 0] directions, while stacking perpendicularly along the [10 $\bar{1}$ 0] direction. The research also revealed that by optimizing the PVP ratio, the width of the nanoflakes can be well controlled. Similarly, Amani et al. successfully synthesized high-quality Te nanoflakes with high effective hole mobility up to 700 $\text{cm}^2\cdot\text{V}^{-1}\cdot\text{s}^{-1}$.^[77] They further demonstrated that the thickness of Te nanoflakes could be controlled by adjusting the reaction time. In addition to the hydrothermal

method, there are also other solution-based synthesis strategies for Te crystals. For example, Qi et al. synthesized surfactant-free Te thin films with high mobility (over 1000 $\text{cm}^2\cdot\text{V}^{-1}\cdot\text{s}^{-1}$) via the ultrasonication-assisted exfoliation of metastable 1T'-MoTe₂.^[78] Although the Te film exhibits an excellent surface condition, the low stability and the difficulty in synthesizing 1T'-MoTe₂ limit the widespread application of this method. Furthermore, Zhao et al. developed an alignment strategy inspired by swimming jellyfish for the wafer-scale alignment of Te nanowires.^[159] The prepared Te thin films exhibit considerable electronic performance and hold great promise for subsequent device applications.

The versatility and simplicity of hydrothermal synthesis make it a promising approach for synthesizing Te nanostructures for various applications in nanoelectronics and other fields. However, further research is needed to obtain a relatively clean surface. Additionally, the limited lateral area of hydrothermal-synthesized Te samples hinders their applications in large-scale circuits.

3.2. Chemical/Physical Vapor Deposition in a Tubular Furnace

Tubular furnaces provide an ideal reaction environment for synthesizing high-quality nanocrystals, particularly single-crystalline thin films. Tubular furnace-based synthesis strategy can be divided into CVD and PVD methods, depending on the reaction type. CVD is a pivotal material growth technology, widely used to produce thin films on a heated substrate through the chemical reaction of gas-phase precursors (Figure 4b). The versatility of CVD is evidenced by its successful synthesis of various high-quality vdW materials, including graphene^[160–162] and MoS₂.^[163,164] suggesting its potential for Te film synthesis as well. Recently, by introducing atomically flat h-BN nanoflakes as the growth substrate, Yang et al. obtained high-quality Te nanobelts and fabricated *p*-type transistors with an ultrahigh hole mobility of $\mu_{\text{FE}} = 1370 \text{ cm}^2\cdot\text{V}^{-1}\cdot\text{s}^{-1}$ at room temperature (Figure 4g).^[80] The HRTEM results in Figure 6f and g illustrate the well-defined and complete crystal lattice with a lattice constant of 0.2 nm for (0001) faces parallel to the helical chains. The high quality of Te nanobelts and clean interface between Te and h-BN dielectric contribute to the high field-effect hole mobility in the subsequent FET. Peng et al. also successfully synthesized high-quality Te nanosheets using the CVD method and applied it to high-performance near-infrared (NIR) photodetectors.^[87] In their work, SnTe₂ powder served as the precursor, placed in a quartz tube, with a silicon (Si) wafer as the substrate located downstream of the carrier gas N₂. By heating SnTe₂ to 650 °C for 30 min, they synthesized high-quality Te nanosheets. HRTEM and selected area electron diffraction (SAED) images demonstrate the highly crystalline hexagonal structure and smooth surface of the Te nanosheet. Notably, their work also showed that Te nanowires could be obtained by adjusting the growing temperature. Based on these experimental results, CVD can be used for growing high-quality, single-crystalline Te nanostructures, but further efforts are needed to precisely control sample thickness and develop the capability to synthesize large-scale Te thin films.

The PVD method in a tubular furnace for synthesizing Te nanocrystals is similar to the CVD method, with the main

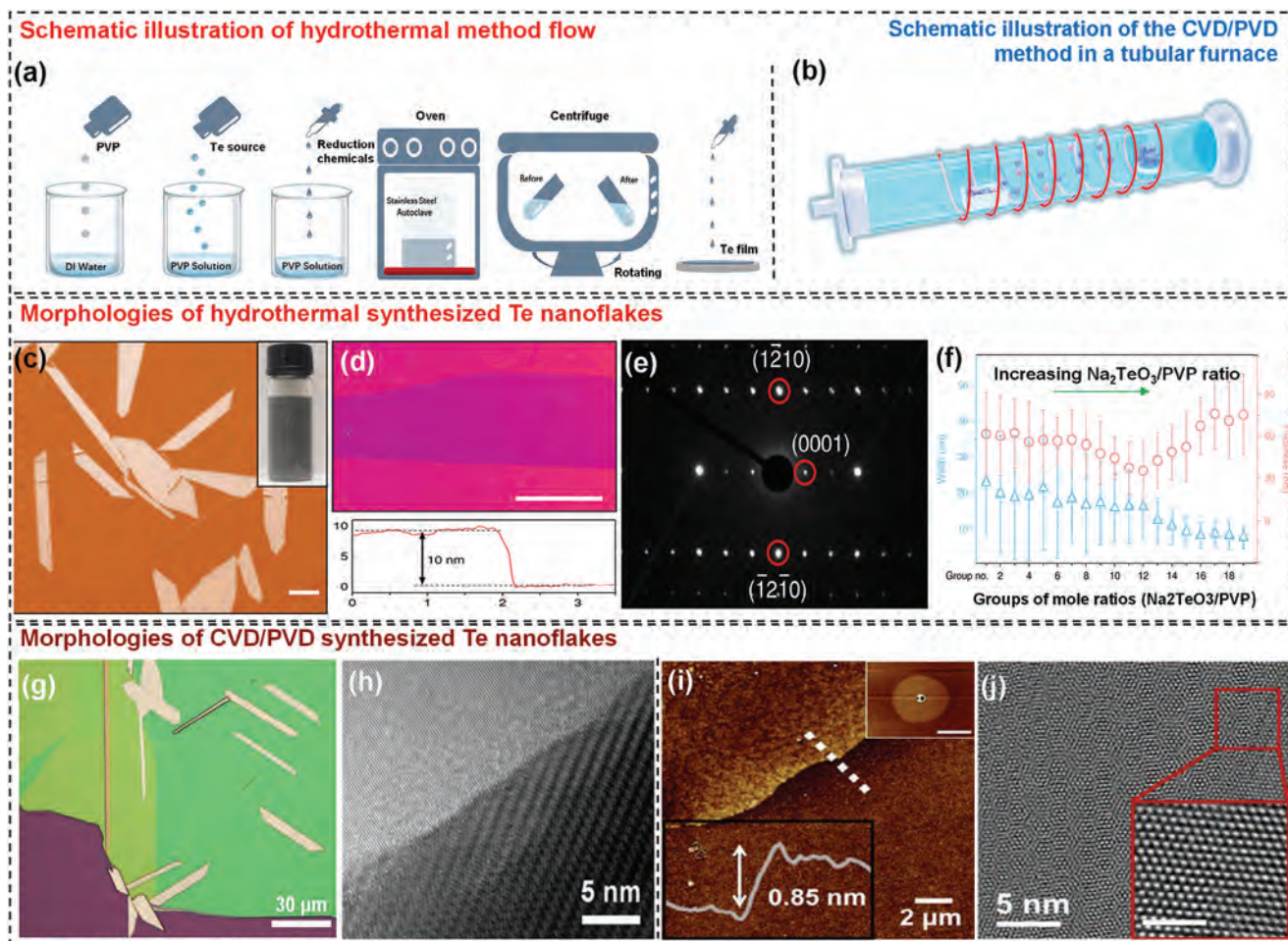


Figure 4. Hydrothermal-synthesized and CVD/PVD-synthesized Te nanostructures in a tubular furnace. a) Schematic illustration of the hydrothermal synthesis process. b) Schematic illustration of CVD/PVD synthesis in a tubular furnace. c) Optical images of hydrothermal-synthesized Te nanoflakes. d) Atomic force microscopy (AFM) characterization of a typical Te nanoflake sample. e) Diffraction pattern of Te nanoflakes. f) Thickness and width modulation of Te nanoflakes. Reproduced with permission.^[76] Copyright 2018, Nature Publishing Group. g) Optical image of Te nanobelts. h) HRTEM image of the boundary between Te and h-BN. Reproduced under the terms of the Creative Commons CC BY license.^[80] Copyright 2022, Springer Science. i) AFM mapping of Te thin films (insets: Low-magnification view of a 0.85-nm thick nanoflake, scale bar: 10 μm (upper right); height profile of the Te thin film (lower left)). j) HRTEM image of Te thin films, scale bar: 2 nm. Reproduced with permission.^[165] Copyright 2019, IOP Publishing Ltd.

difference being the precursors used. Te nanocrystals are typically prepared from Te powders via a physical reaction route. The PVD method in a tubular furnace shares a similar reaction system to CVD, as illustrated in Figure 4b. For the application of PVD in synthesizing Te thin films, Apte et al. initially synthesized ultrathin Te films by evaporating Te source in Ar/H₂ gas flow at 650 °C.^[165] Te thin films with a thickness of 0.85 nm were successfully obtained, and the hexagonal symmetry of Te was also identified (Figure 4i,j). Furthermore, Yang et al. demonstrated the possibility of controlling the orientation of Te atomic chains on a GaSe substrate.^[86] Specifically, the research revealed a well-oriented alignment of Te atomic chains along the GaSe armchair lattice direction. This crystal alignment results from the higher binding energy difference, which acts as an energy barrier, between self-oriented Te along the armchair and zigzag edges of GaSe. Recently, Meng et al. reported an attractive method for large-scale, high-quality Te nanomesh synthesis on various flexible substrates at low temperature.^[85] After the initial growth of Te

nanowires, followed by 2 hours of heating, the Te nanowires self-welded with each other to form nanomeshes. This self-welding property significantly simplifies the synthesis of Te nanomeshes and provides relatively high mobility within the polycrystalline systems. In addition, Wang et al. reported the vdW epitaxy growth of hexagonal Te nanoplates on flexible mica substrate.^[166] In contrast to previous reports, the *c*-axis of the prepared nanoplates in this study is perpendicular to the substrate surface. In their method, a PVD technique in a horizontal vacuum tube furnace was adopted, where Te powder was used as the precursor, and the introduction of mica sheets as the growth substrate facilitated the migration of Te adatoms along the mica surface. The carrier gas was high-purity Ar, and the reaction temperature was maintained above 500 °C. The successful synthesis of high-quality Te thin films, precise control of Te atom chain orientation, and the simplified fabrication of Te nanomeshes make PVD an appealing method for synthesizing Te nanostructures and developing high-performance Te-based electronics and optoelectronics. However,

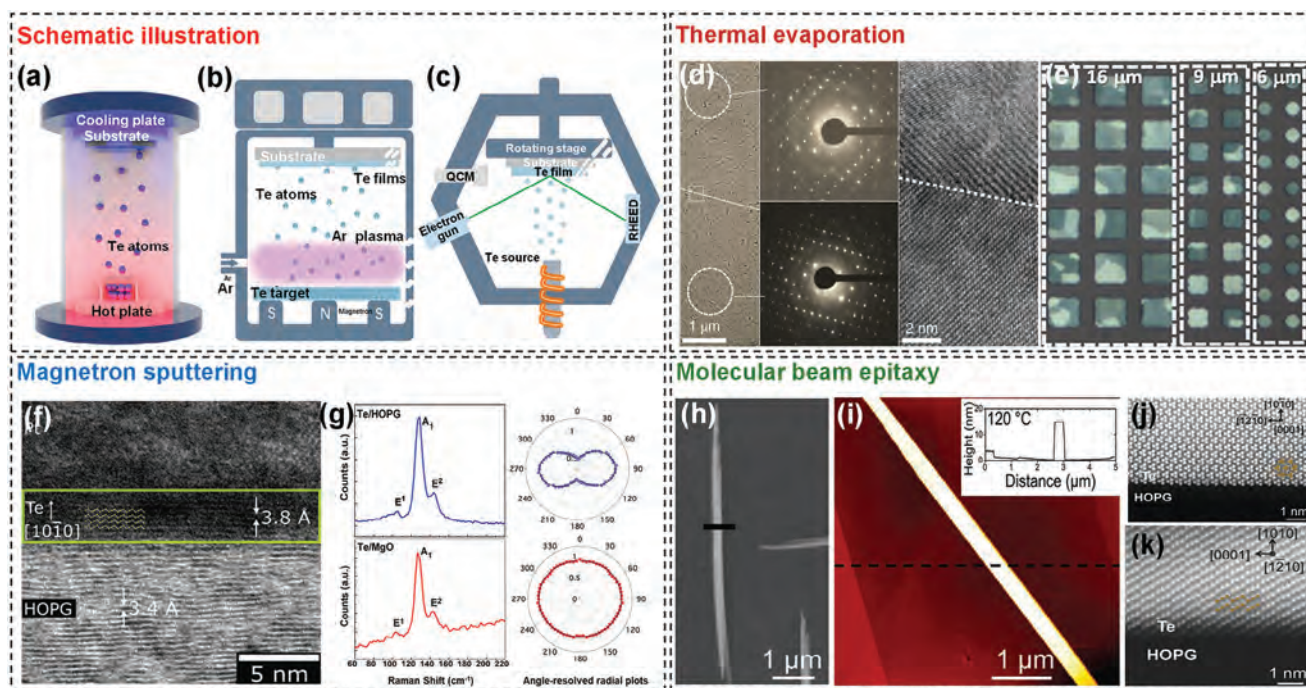


Figure 5. Thermal evaporation, magnetron sputtering, and magnetron sputtering-synthesized Te nanostructures. a–c) Schematic illustration of thermal evaporation, magnetron sputtering, and MBE, respectively. d) Microscopy image of Te nanofilms. Reproduced with permission.^[89] Copyright 2020, Nature Publishing Group. e) Polarized light microscopy image of a patterned crystallized Te array with varying lateral dimensions. Reproduced with permission.^[90] Copyright 2021, John Wiley & Sons, Inc. f) HRTEM image of ultrathin Te on HOPG substrate. g) Polarized Raman spectra (left) and angle-resolved radial plots (right) of the A₁ mode intensities from Te films grown on HOPG (blue) and MgO (red). Reproduced under the terms of the Creative Commons CC BY 3.0 license.^[149] Copyright 2020, The Royal Society of Chemistry. h) Scanning electron microscopy (SEM) image of a Te needle on an HOPG substrate. i) AFM image of a Te needle on HOPG substrate. j, k) HRTEM images of Te. Reproduced with permission.^[133] Copyright 2018, John Wiley & Sons, Inc.

similar to the challenges encountered in CVD methods, meticulous efforts are necessary to attain precise control over the thickness of Te films, especially in the context of ultrathin scenarios.

3.3. Thermal Evaporation

In addition to the PVD in a tubular furnace, high-quality Te thin films can also be prepared using other PVD techniques, such as thermal evaporation, magnetron sputtering, and MBE. Thermal evaporation has been a long-studied method for the preparation of Te thin films (Figure 5a).^[167] Recently, Zhao et al. reported pioneering work on depositing high-quality Te thin films onto cryogenic deposition substrates.^[89] Specifically, they utilized Te particles as the evaporation source and lowered the substrate temperature to -80°C to form high-quality Te thin film, as confirmed by transmission electron microscopy (TEM) and diffraction pattern results (Figure 5d). Subsequently, Zhao et al. obtained large-area crystallized Te nanofilms by selecting an appropriate crystallization temperature to both overcome the kinetic constraints between thermodynamically less-favorable amorphous Te and control a moderate crystallizing speed.^[90] As shown in Figure 5e, when carefully selecting 273.15 K as the crystallization temperature, large-area ($150\ \mu\text{m}^2$) and highly oriented Te thin film was successfully synthesized. Thermal evaporation can be considered as an attractive method for the growth of wafer-scale Te samples;

however, further research is needed to reduce the defect density and grain boundaries in polycrystalline Te thin films.

3.4. Magnetron Sputtering

Magnetron sputtering has emerged as a widely adopted technique for thin film deposition, particularly in the context of large-area 2D thin films.^[168–170] This process utilizes a magnetically enhanced plasma to sputter material from a target source onto a substrate, thereby forming a thin film (Figure 5b). In response to the growing demand for large-area Te thin films, magnetron sputtering has gained increasing prominence in the synthesis of Te films. Significant contributions by Bianco et al. showcased the successful synthesis of ultrathin Te films (2.5 nm) on a HOPG substrate using unbalanced magnetron sputtering (Figure 5f).^[149] The Te structure exhibits a 3.8 Å spacing between (100) planes, signifying the alignment of helical chains in a horizontal orientation, with [0001] parallel to the HOPG surface. Furthermore, by changing the substrate to MgO, they found that the Te [0001] helical chains can grow in the vertical direction on the MgO substrate and display different angle-resolved Raman spectra (Figure 5g). Kim et al. further extended the capabilities of magnetron sputtering to enable the synthesis of single-crystalline Te thin films directly on a Si wafer by introducing an Al_2O_3 encapsulation layer.^[95] The employment of the Al_2O_3 encapsulation

layer played a pivotal role in stabilizing the interfacial energy, thereby significantly promoting the Te crystal size and facilitating the growth of large-area Te thin films. Although magnetron sputtering has proven to be an effective method for synthesizing Te thin films and can control the orientation of Te atomic chains through substrate selection, its difficulty in synthesizing large-area single-crystalline films hinders the achievement of high carrier mobilities (19 and $30.9 \text{ cm}^2 \cdot \text{V}^{-1} \cdot \text{s}^{-1}$ in refs. [95,149], respectively), which restricts its use in high-performance devices.

3.5. Molecular Beam Epitaxy

MBE is widely recognized as an effective technique for the growth of vdW materials due to its exceptional capabilities.^[171–173] This method excels in providing precise control on thickness, ensuring atomic-level precision, and maintaining high purity and cleanliness throughout the growth process. A schematic illustration of the MBE system is shown in Figure 5c. Huang et al. successfully synthesized large-scale, atomically flat monolayer and few-layer Te thin films on a graphene/6H-SiC(0001) substrate, with step heights of 0.15 and 0.39 nm , respectively.^[92] Additionally, Zhou et al. developed a low-temperature MBE method to synthesize high-quality 2D Te nanostructures on different substrates.^[93] This versatile technique is applicable to substrates such as SiO_2/Si , polyethylene terephthalate (PET), and HOPG. The Te growth on all three substrates resulted in compact, needle-like nanostructures, with varying lengths. For further analysis, the longest Te needles, observed on the HOPG substrate, were examined (Figure 5h). AFM analysis revealed that Te nanostructures had a smooth surface with a height of 16 nm (Figure 5i). Scanning transmission electron microscopy (STEM) results (Figure 5j,k) displayed a typical hexagonal lattice and zig-zag chain structure, confirming the high quality of the Te needles. While MBE is an excellent method for achieving precise control over atomic-level thickness, further extensive research is required to explore its potential for producing large-scale Te thin films with high crystallinity. This research is necessary to enhance the method's viability for practical applications, similar to the thermal evaporation and magnetron sputtering methods discussed earlier.

Table 2 summarizes the advantages and disadvantages of various synthesis methods for Te crystals. From this, it can be concluded that achieving both high crystallinity and scalability in a

single method remains challenging at the current stage. We are still in the process of developing a growth strategy capable of producing high-quality Te thin films on a wafer scale for advanced large-scale circuits.

4. Electronics

As a naturally stable, hole-dominated vdW semiconductor, Te nanostructures offer a promising *p*-type option to complement mainstream *n*-FETs based on other vdW materials, particularly those from the extensive TMD family.^[76,80,85,90,93,96,174,175] While vdW semiconducting thin films hold great potential to extend Moore's law as a supplement to the Si industry, the metal-semiconductor contact has long been a significant challenge, often referred to as a "Gordian knot," in 2D FETs. Unlike conventional Si FETs, ion implantation for achieving ohmic contact is nearly impossible in 2D FETs due to the atomically thin nature of vdW channels. To reduce the contact resistance or optimize carrier transport, various contact engineering strategies have been explored to enhance the performance of Te FETs.^[98–101,176–178] Meanwhile, Te FETs typically exhibit low room-temperature on/off current ratios, a limitation caused by the narrow bandgap of the Te channel, which significantly hinders their application in high-performance integrated circuits. Recently, reports on topological phase change transistors (TPCTs) based on Te nanoflakes offer a promising solution. In these devices, the gate-tunable topological phase change in Te enables a significantly higher on/off current ratio, surpassing that of most 2D FETs.^[102,103] Additionally, Te nanostructures have potential application in floating gate (FG) memory devices, nanogenerators, radio frequency (RF) diodes, and electrical switches.^[104–109,111,116,179] In this section, we discuss the application of Te nanostructures in electronics, including FETs, TPCTs, and other devices beyond transistors. Given that FETs operate based on the charge depletion/accumulation, and to better distinguish between Te FETs and TPCTs, we refer to conventional FETs as charge-based transistors in this Review.

4.1. Charge-Based Transistors

The invention of the transistor and its development over the past 75 years are arguably among the most far-reaching technological achievements in human history. With the scaling of

Table 2. Summary of different synthesis methods for Te crystals.

Synthesis strategy	Crystallinity	Scalability	Cost	Substrate compatibility	Representative papers
Hydrothermal	Single-crystalline	Low	Low	High	[76]
Ultrasonication-assisted exfoliation	Single-crystalline	Low	Low	High	[78]
CVD/PVD	Single-crystalline	Middle	Middle	Middle	[80,165]
Thermal evaporation	Polycrystalline	High	High	High	[89]
Magnetron sputtering	Polycrystalline	High	High	Low	[149]
Molecular beam epitaxy	Polycrystalline	High	High	Low	[92]
Biomimetic alignment	N.A.	High	Middle	Middle	[159]

N.A., Not applicable.

3D semiconductor-based transistors approaching its physical limit, the emergence of vdW semiconducting thin films offers a promising solution to extend Moore's law.^[20,22,23] However, among the various 2D FETs, most exhibit *n*-type transport behavior, while *p*-type counterparts with competitive performance have been rarely reported, posing a significant obstacle to the practical application of vdW semiconducting thin films. Black phosphorus, for example, demonstrates high hole mobility but suffers from poor air stability.^[180] The recent resurgence of interest in Te has rekindled enthusiasm among researchers for designing and fabricating high-performance 2D *p*-FETs. This renewed interest was sparked by Wang et al.'s report on the hydrothermal synthesis of ultrathin Te nanoflakes in 2017.^[76] The strong spin-orbit coupling in Te results in a small hole-effective mass, leading to the expectation of high hole mobilities under an external electric field.^[181] The operation of *p*-type Te FETs is based on the accumulation and depletion of hole densities in response to gate voltage. When a negative (positive) gate voltage is applied, the Fermi level in the Te channel moves closer to (further from) the valence band, leading to the accumulation (depletion) of hole density in the channel, which corresponds to the "ON" ("OFF") state of the *p*-type Te FET. **Figure 6a,b** shows the output and transfer curves measured on a typical Te FET fabricated by Wang et al., where the channel thickness and length were 11.1 and 300 nm, respectively. Notably, the maximum on-state current in the Te FET reaches 1 mA/μm under the bias of 1.4 V, which is highly encouraging. This large on-state current indicates a fast switching speed, a crucial figure of merit defined by the International Technology Roadmap for Semiconductors (ITRS) and the International Roadmap for Devices and Systems (IRDS) 2023.^[182] The unique 1D crystal structure of Te leads to anisotropic electrical transport behaviors. As shown in **Figure 6c**, the field-effect hole mobility (μ_{hole}) along the [0001] direction is ≈ 1.4 times higher than that along the [1 $\bar{2}$ 10] direction. Wang et al. also observed that μ_{hole} increases with Te thickness, albeit at the cost of reduced on/off current ratios (**Figure 6d**).

In addition to the hydrothermal method, single-crystalline Te nanobelts can also be synthesized using a CVD system. In 2022, Yang et al. reported the growth of single-crystalline Te nanobelts by introducing h-BN nanoflakes as the deposition substrate in a CVD system.^[80] The atomically flat interface provided by h-BN significantly reduces the scattering centers, enabling an ultrahigh room-temperature field-effect hole mobility of up to 1370 cm² V⁻¹ s⁻¹ (**Figure 6e**). Additionally, the high vapor pressure of $\approx 10^{-5}$ Torr at 250 °C, coupled with the low crystallization temperature, facilitates the sublimation of Te and its recrystallization on nearly any surface.^[183,184] In 2023, Meng et al. reported the vapor-phase growth of Te nanomesh on various substrates, including rigid (sapphire, SiO₂, and mica), flexible (polyimide (PI) and polydimethylsiloxane (PDMS)), vdW nanoflakes (WS₂ and h-BN), and 3D curved (carbon fibers) surfaces.^[85] Even more intriguing is that paper was also used as the growth substrate, with the resulting photoconductor exhibiting a fast switching speed as short as ≈ 3 μs. The conductance of a Te FET made from a Te nanomesh thin film grown on 50-nm SiO₂/p++ Si can be effectively tuned by the gate bias, and μ_{hole} extracted in the linear region reaches 145 cm² V⁻¹ s⁻¹ (**Figure 6f,g**). Additionally, researchers have reported the biomimetic wafer-scale alignment of Te nanowires for use in flexible and stretchable electronics.^[159]

Their fabricated Te nanowire-based thin film transistor (TFT) realized a high on/off current ratio of up to 10⁴ and a field-effect hole mobility exceeding 100 cm² V⁻¹ s⁻¹.

Between 2019 and 2021, Zhao et al. developed and optimized the low-temperature thermal evaporation technique for Te thin films, leading to high-performance Te FETs and logic gates.^[89,90] By lowering the crystallization temperature of Te to 5 °C, they were able to achieve a Te single-crystalline domain size of ≈ 150 μm². The resulting Te FET, based on a single crystal, exhibited an on/off current ratio of $\approx 10^5$ and an effective hole mobility of ≈ 100 cm² V⁻¹ s⁻¹ (**Figure 6h,i**). However, the tendency of Te to sublimate at relatively low temperatures presents a challenge to the thermal stability of Te FETs, necessitating further research to address this issue.^[185] Dielectric doping is a widely used strategy to tune the threshold voltage of metal-oxide-semiconductor field-effect transistor (MOSFETs).^[186–188] The introduction of a dipole via atomic layer deposition (ALD) of HfO₂ at the interface between the metal oxide and Te nanoflakes can effectively dope the Te channel to *n*-type. Based on this approach, Qiu et al. demonstrated *n*-type Te FETs with performance comparable to their *p*-type counterparts, making them suitable for high-performance complementary metal-oxide-semiconductor (CMOS) devices.^[97] Specifically, a representative *n*-type Te FET exhibited a large on-state current of 200 μA·μm⁻¹, a considerable on/off current ratio of $\approx 10^3$, a respectable field-effect electron mobility of ≈ 612 cm² V⁻¹ s⁻¹, and a low contact resistance of 4.3 kΩ·μm (**Figure 6j–l**). Although challenges such as low on/off current ratios and thermal stability remain to be addressed before Te can be commercialized, its *p*-type semiconducting nature, air stability, and high hole mobility make it an attractive vdW material platform for future high-performance electronics.

4.2. Strategies for Performance Optimization of Te FETs

The realization of high-quality contacts in 2D FETs has long been a significant challenge, as the ultrathin nature of vdW semiconducting thin films is incompatible with common doping techniques, such as ion implantation, used in the Si industry. While recent reports have achieved contacts approaching the quantum limit in 2D semiconductors, most of these advances have focused on *n*-FETs, particularly MoS₂-based devices.^[189–191] With the emergence of *p*-type Te, researchers also explored various methods to reduce Schottky barrier heights and tune transport behaviors in Te FET.^[98–101,177,178] To minimize the Fermi level pinning effect, which is typically unavoidable in conventional metal-semiconductor contact, Zhang et al. were the first to report the usage of vdW 1T'-WS₂ semimetal, with a work function of ≈ 4.95 eV, as the electrodes to reduce the Schottky barrier height in *p*-type Te FETs.^[98] By employing this all-vdW semimetal-semiconductor contact strategy, they realized ohmic contact in Te FETs (**Figure 7a**), reducing the Schottky barrier height for hole injection to 3 ± 9 meV (**Figure 7b**). This improved contact quality also led to a high μ_{hole} of ≈ 1304 cm² V⁻¹ s⁻¹. Additionally, Lin et al. studied the transport properties of *p*-type Te FETs using high-work function metal Pt (≈ 5.65 eV) as contact electrodes, reporting a low contact resistance of 400 Ω·μm (**Figure 7c**).^[99] More interestingly, Pt can serve as the photosensitive catalyst to controllably reduce the Te channel thickness in water, leading to larger

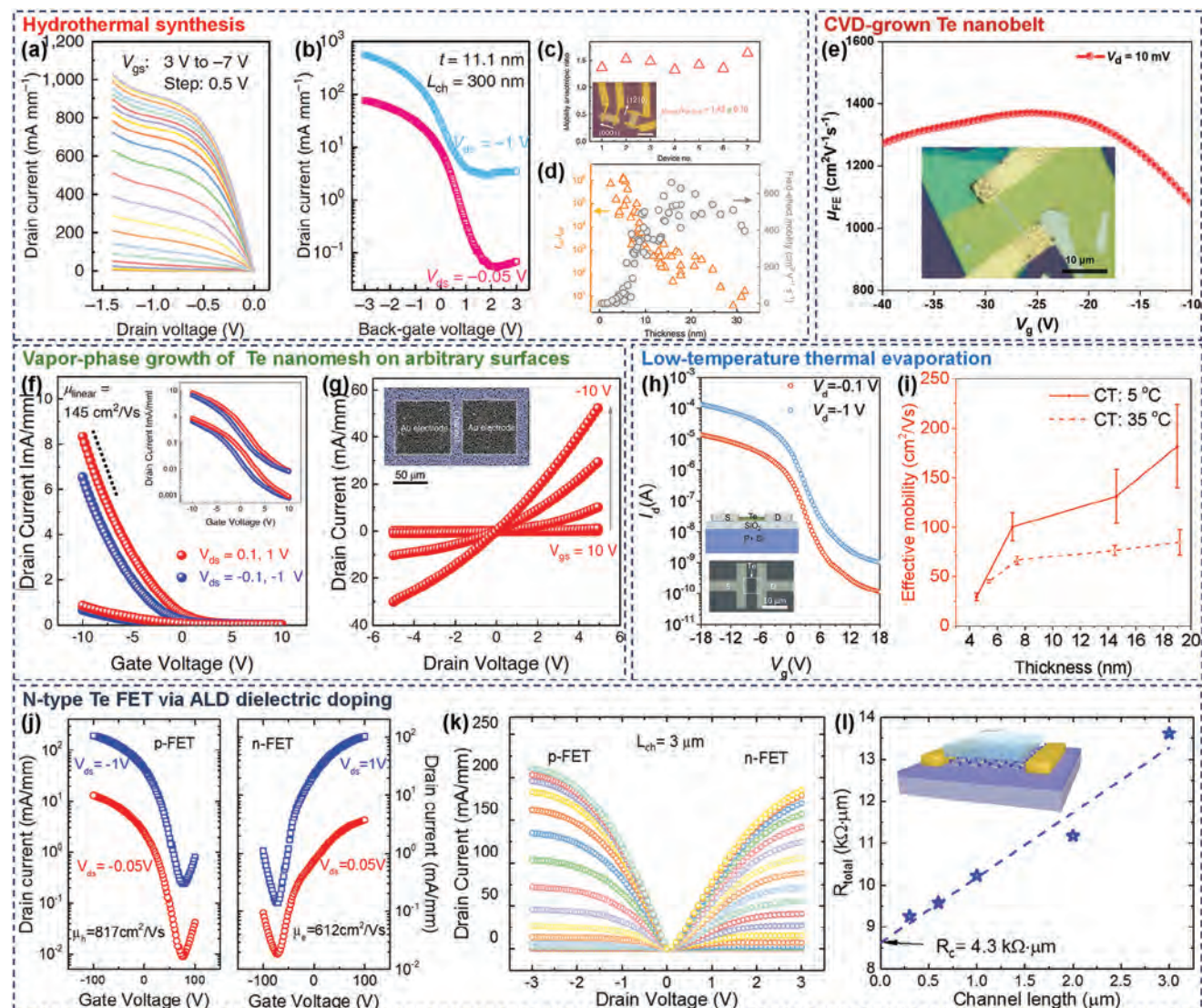


Figure 6. Charge-based FETs enabled by Te nanostructures prepared through various methods. Hydrothermal-synthesized Te nanoflake: a) Output and b) transfer curves of a *p*-type Te FET with a channel thickness of 11.1 nm and length of 300 nm. c) Mobility anisotropy ratio of hole mobility measured along the [0001] direction over the [1210] direction on a batch of devices. Inset: Optical image of a representative device pair for anisotropic transport measurement, with a scale bar of 10 μm . d) Thickness-dependent on/off current ratios and field-effect hole mobilities. Reproduced with permission.^[76] Copyright 2018, Nature Publishing Group. CVD-grown Te nanobelt on h-BN substrate: e) Room-temperature field-effect hole mobilities under different V_g measured in a representative Te FET. Inset: Optical image of the measured device. Reproduced under the terms of the Creative Commons CC BY license.^[80] Copyright 2018, Springer Science. CVD-grown Te nanomesh thin film: f) Transfer and g) output curves of a Te FET. Inset of (f) shows the semi-log-scale transfer curves. Inset of (g) provides the optical image of the measured device. Reproduced under the terms of the Creative Commons CC BY license.^[85] Copyright 2023, Nature Publishing Group. Low-temperature-thermal-evaporation Te single crystal: h) Transfer curves measured on a Te FET. Inset: Schematic and optical image of a representative device. i) Thickness-dependent effective mobility measured on devices based on Te single crystals evaporated at different temperatures. Reproduce with permission.^[90] Copyright 2021, John Wiley & Sons, Inc. N-type Te FET via dielectric doping: j) Transfer and k) output curves of *n*-type/*p*-type (with/without ALD dielectric doping) Te FETs. l) Extracted contact resistance in *n*-type Te FET via transmission line method (TLM). Inset: Schematic illustration of the *n*-type Te FET with ALD dielectric doping. Reproduced with permission.^[97] Copyright 2018, The Institute of Electrical and Electronics Engineers.

on/off current ratios. Conversely, when using Sc, which has a low work function of ≈ 3.58 eV, as the contact metal, Qin et al. transformed the *p*-type transport behavior in Te FET into ambipolar transport, achieving a hole mobility of $648 \text{ cm}^2 \text{ V}^{-1} \text{ s}^{-1}$ and an electron mobility of $489 \text{ cm}^2 \text{ V}^{-1} \text{ s}^{-1}$ (Figure 7d).^[100]

To further enhance carrier injection efficiency, edge contacts have been developed for layered semiconductors and are

expected to play an important role in constructing 2D FETs within the gate-all-around (GAA) architecture.^[192–200] In 2021, Jiang et al. reported the use of edge contacts for Te-nanorod-based FETs (Figure 7e).^[101] Their study confirmed the formation of Pd-Te alloy at the end of the Te nanorod, as evidenced by the HRTEM image (Figure 7f). The linear output curves indicated good contact quality, with a contact resistance

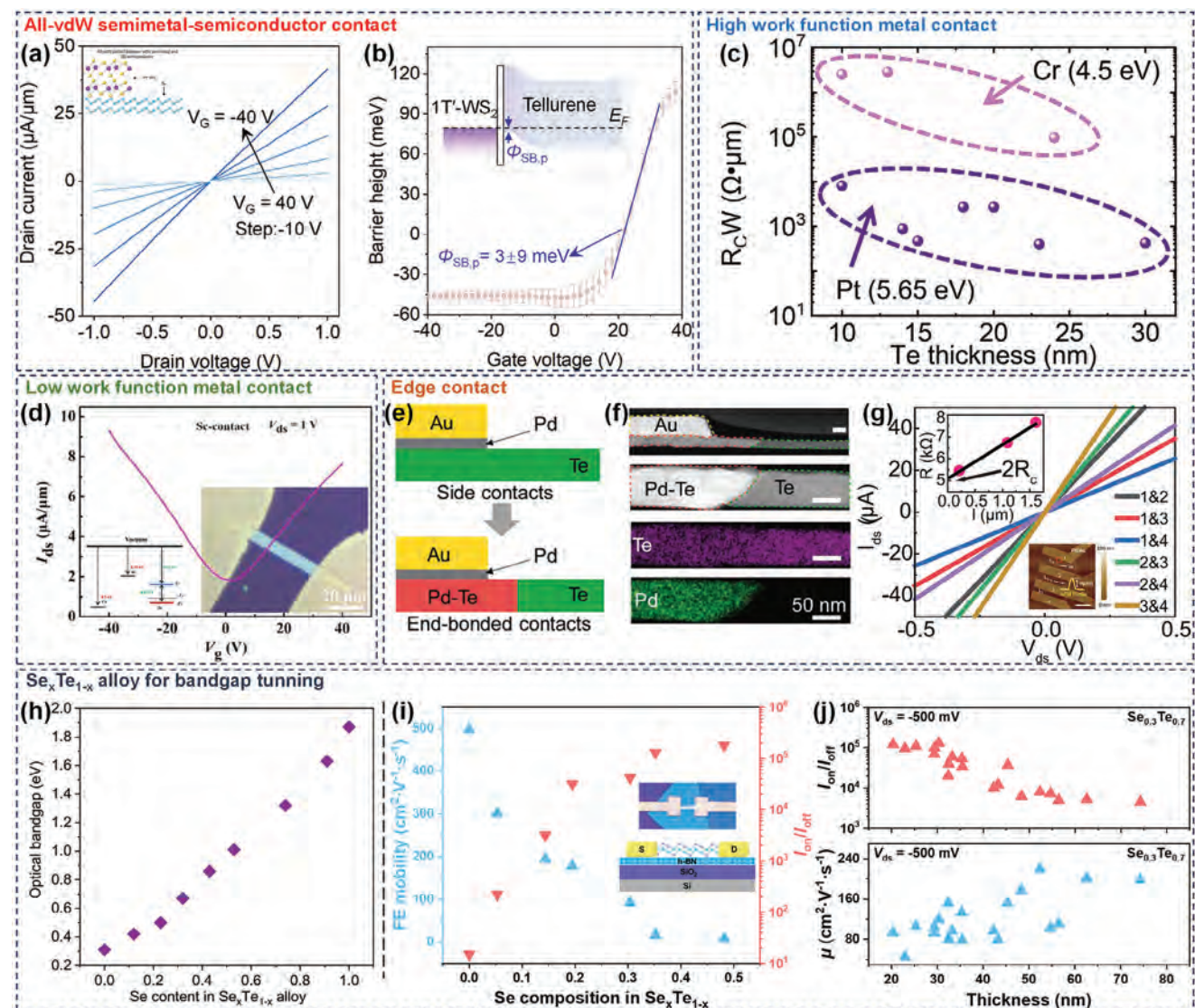


Figure 7. Different strategies for performance optimization of Te FETs. All-vdW semimetal-semiconductor contact: a) Linear output curves measured under different V_g . Inset: Schematic illustration of 1T'-WS₂/Te stacking as a contact. b) Schottky barrier height extracted at flat band condition from Arrhenius plots. Inset: Band diagram of the 1T'-WS₂/Te heterojunction at flat band condition. Reproduced with permission.^[98] Copyright 2022, John Wiley & Sons, Inc. High work-functional metal contact: c) Low contact resistance of Te FET enabled by high-work-function Pt. Reproduced with permission.^[99] Copyright 2022, John Wiley & Sons, Inc. Low work-functional metal contact: d) Ambipolar Te FET enabled by low work function metal Sr. Insets: Energy diagram of Te, Cr, and Sc (left inset); optical image of a representative device (right inset). Reproduced with permission.^[100] Copyright 2019, IOP Publishing Ltd. Edge contact: e) Schematic illustration of end-bonded Pd-Te contact. f) Cross-section HRTEM image of a Te FET enabled by end-bonded contacts. g) Output curves measured on a series of Te FETs with different channel lengths. Insets: Extracted contact resistance from the TLM method (top) and AFM image of the measured devices (bottom). Reproduced with permission.^[101] Copyright 2021, The American Chemical Society. Se_xTe_{1-x} alloy for bandgap tuning: h) Se composition-dependent bandgap of Se_xTe_{1-x} alloy. Reproduced with permission.^[201] Copyright 2020, John Wiley & Sons, Inc. i) Relationship between μ_{hole} and on/off current ratio in Se_xTe_{1-x} alloy-based FETs with varying Se composition. Inset: Optical image (top panel) and schematic illustration (bottom panel) of a Se_xTe_{1-x} alloy-based FET. j) Thickness-dependent on/off current ratio (top panel) and μ_{hole} (bottom panel) in Se_{0.3}Te_{0.7} nanosheet-based FET. Reproduced with permission.^[202] Copyright 2024, The American Chemical Society.

of 2.55 k Ω , as extracted by the TLM, for a channel width of ≈ 16 nm (Figure 7g). More intriguingly, Niu et al. developed gate-controlled superconducting FETs based on the Pd_xTe–Te contacts, achieved by diffusing Pd atoms into the Te channel.^[110] While some progress has been made in optimizing contacts for Te FETs, the contact resistance reported thus far is still far away from the quantum limit. Much more effort is needed in

this field, especially considering that Te is a unique *p*-type vdW semiconductor.

Limited by its narrow bandgap, achieving a moderate on/off current ratio at room temperature is a common challenge for Te FETs. The growth of Se_xTe_{1-x} alloys offers a promising solution to this issue. In 2020, Tan et al. reported the low-temperature evaporation of Se_xTe_{1-x} thin films, which allowed for a tunable

Table 3. Comparison between FETs enabled by Te and other vdW semiconductors.

Channel material (Preparation method)	Channel/gate length [μm]	I_{on} [$\mu\text{A } \mu\text{m}^{-1}$]@ V_{ds}	$I_{\text{on}}/I_{\text{off}}$	SS [mV dec^{-1}]	Contact resistance [$\Omega \cdot \mu\text{m}$]	Refs.
Monolayer MoS_2 (CVD)	0.02 (channel)	1230@1 V	10^8	180	42	[189]
3-layer MoS_2 (CVD)	0.01 (channel)	1220@0.7 V	$\approx 10^8$	74	69	[204]
Monolayer MoS_2 (MOCVD)	0.035 (channel)	1135@1.5 V	$> 10^7$	N.A.	132	[191]
Monolayer MoS_2 (CVD)	0.05 (channel)	1000@2 V	$\approx 10^7$	N.A.	660	[205]
Few-layer MoS_2 (Exfoliated)	0.001 (gate)	> 10 @1 V	10^6	65	N.A.	[206]
Monolayer MoS_2 (CVD)	0.00034 (gate)	0.545@1 V	$\approx 10^5$	117	N.A.	[21]
Monolayer WS_2 (CVD)	0.03 (channel)	414@1.5	$\approx 10^8$	≈ 90	1200	[207]
Monolayer WS_2 (CVD)	0.05 (channel)	325@1 V	1.8×10^8	N.A.	1100	[208]
Few-layer WS_2 (Exfoliated)	0.1 (channel)	380@2 V	$> 4 \times 10^6$	N.A.	700	[209]
2-layer WS_2 (MOCVD)	0.1 (channel)	210@1 V	$> 10^8$	109	2380	[210]
2-layer MoSe_2 (CVD)	0.5 (channel)	65@4 V	10^6	N.A.	60000	[211]
Monolayer WSe_2 (CVD)	0.065 (channel)	300@−1 V	$> 2 \times 10^6$	225	950	[212]
Monolayer WSe_2 (Exfoliated)	3.5 (channel)	210@3 V	10^6	N.A.	7500	[213]
Multilayer MoTe_2 (Exfoliated)	0.6 (channel)	65@−4 V	$\approx 10^4$	N.A.	N.A.	[214]
5-layer MoTe_2 (Exfoliated)	0.1 (channel)	150@1 V	10^5	N.A.	2000	[215]
Multilayer SnS_2 (Exfoliated)	0.4 (channel)	4@5 V	2×10^6	N.A.	N.A.	[216]
Monolayer SnSe_2 (Exfoliated)	≈ 1 (channel)	30@1 V	10^4	N.A.	N.A.	[217]
3-layer ReSe_2 (Exfoliated)	5 (channel)	≈ 1.5 @2 V	$> 10^4$	1300	N.A.	[218]
Few-layer InSe (Exfoliated)	0.02 (channel)	1350@0.5	$> 10^8$	≈ 60	< 62	[219]
Few-layer bP (Exfoliated)	1 (channel)	580@−3 V	$\approx 10^4$	≈ 170	N.A.	[220]
Few-layer bP (Exfoliated)	0.8 (channel)	200@3 V	$> 10^3$	N.A.	N.A.	[221]
Few-layer bP (Exfoliated)	1 (channel)	194@−2 V	10^4	N.A.	N.A.	[222]
Few-layer bP (Exfoliated)	0.3–1.5 (channel)	920@1.8 V ^{a)}	$\approx 10^4$	N.A.	750	[223]
Few-layer bP (Exfoliated)	0.1 (channel)	480@−2 V	$\approx 10^4$	N.A.	N.A.	[224]
Few-layer Te (Hydrothermal)	0.3 (channel)	1000@−1.4 V	$\approx 10^2$	N.A.	N.A.	[76]
Few-layer Te (Hydrothermal)	3 (channel)	200@3 V	$\approx 10^3$	N.A.	4300	[97]
Multilayer Te (CVD)	≈ 10 (channel)	27@0.5 V ^{a)}	$\approx 10^2$	N.A.	N.A.	[80]
Te thin film (Thermal evaporation)	3.7 (channel)	120@−10 V	$\approx 10^5$	2700	N.A.	[90]
Te thin film (Magnetron sputtering)	20 (channel)	−20@−50 V	$> 10^4$	6500	N.A.	[95]
Te nanomesh (PVD ^{b)})	≈ 17 (channel)	≈ 50 @5 V ^{a)}	$\approx 10^3$	N.A.	N.A.	[85]
Te nanowire array (Solution-phase)	20 (channel)	−7@−20 V	$\approx 10^4$	N.A.	N.A.	[159]
Te nanowire (MBE)	6 (channel)	≈ 200 @0.5 V ^{a)}	$> 10^2$	N.A.	N.A.	[93]

MOCVD, metal–organic chemical vapor deposition; N.A., not applicable; ^{a)} Although the highest I_{on} was obtained at a positive bias, the polarity of the reported transistor is *p*-type.

bandgap from 0.31 eV (Te) to 1.87 eV (Se) (Figure 7h).^[201] Although the on/off current ratio reached 10^4 , the effective mobilities dropped to $1.2 \text{ cm}^2 \text{ V}^{-1} \text{ s}^{-1}$, likely due to enhanced carrier scattering caused by the polycrystalline nature of the samples. In 2024, Huang et al. developed the precursor-confined CVD growth method for producing single-crystalline $\text{Se}_x\text{Te}_{1-x}$ nanosheets for high-performance *p*-type FETs.^[202] The fabricated transistors (inset in Figure 7i) achieved a good balance between on/off current ratios and room-temperature field-effect hole mobilities. After optimizing the Se composition ($x \approx 0.3$), the $\text{Se}_{0.3}\text{Te}_{0.7}$ nanosheet-based FET exhibited a considerable on/off current ratio of 4×10^5 and a room-temperature field-effect hole mobility of up to $120 \text{ cm}^2 \text{ V}^{-1} \text{ s}^{-1}$, as shown in Figure 7i. The authors

also illustrated the thickness-dependent on/off current ratio and μ_{hole} in $\text{Se}_{0.3}\text{Te}_{0.7}$ FETs (Figure 7j), with results similar to those reported for Te FETs.

To benchmark the development of Te FETs, we have summarized the performance of FETs enabled by various vdW semiconductors in Table 3. In this table, the highest on-state current obtained at a negative bias indicates the polarity of that reported FET is *p*-type unless otherwise stated. We also recommend readers to refer to McClellan et al.'s work for updates on the latest developments in 2D FETs.^[203] Five dimensions—channel length, highest on-state current (I_{on}), on/off current ratio ($I_{\text{on}}/I_{\text{off}}$), sub-threshold swing (SS), and contact resistance—are used in Table 3 to evaluate FET performance. From these data, it is evident that

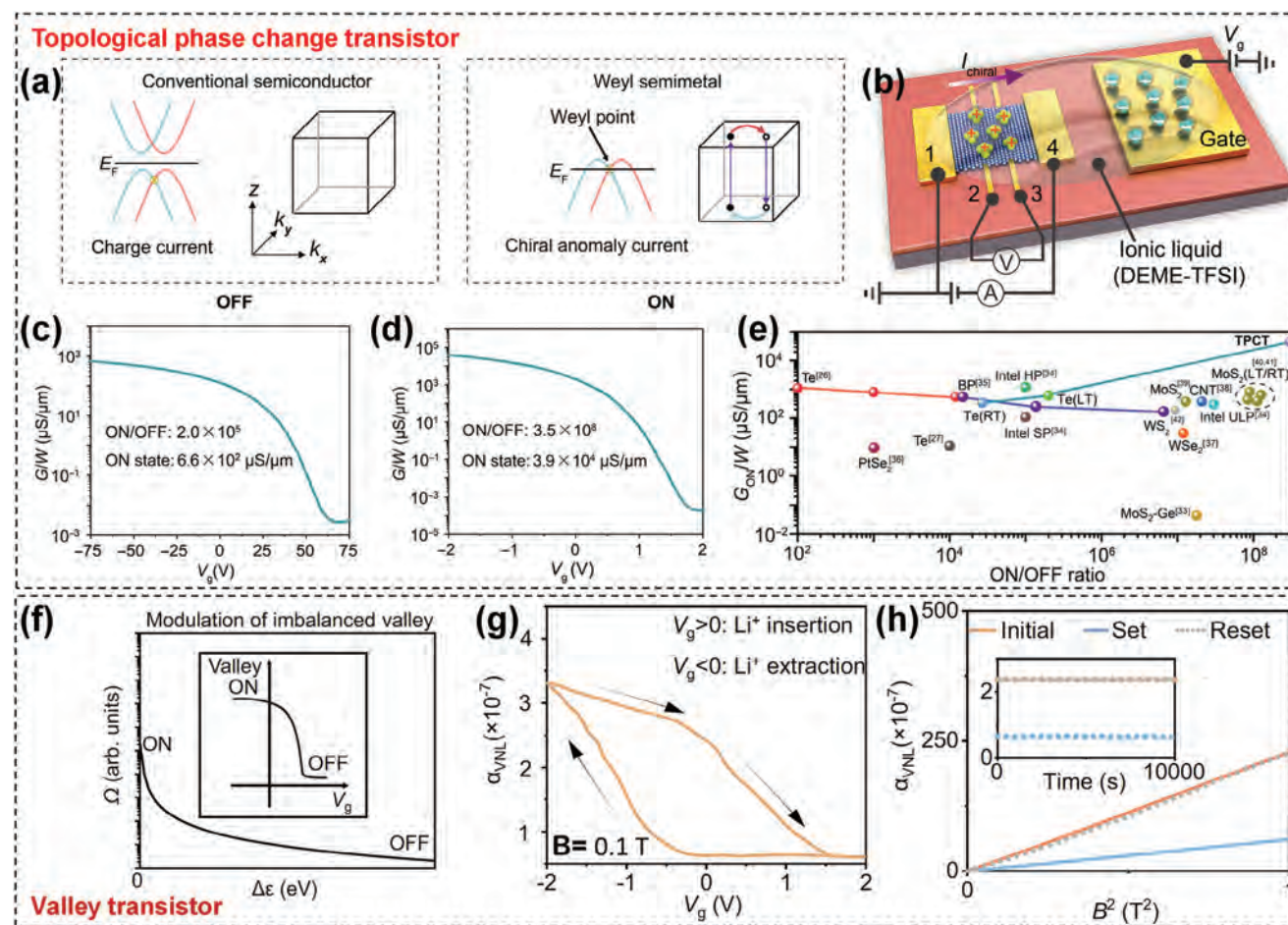


Figure 8. TPCT and valley transistor enabled by hydrothermal-synthesized Te nanoflakes. TPCT: a) Comparison of the energy band diagram of Te nanoflakes in conventional semiconductor and Weyl semimetal topological phases. b) Schematic illustration of a TPCT enabled by Te nanoflake with ionic gating. c) B^2 -dependent chiral anomaly conductance measured under different V_g . d) Transfer curve measured on a Te TPCT. e) Benchmark of Te TPCT performance compared with other 2D FETs. Reproduced under the terms of the Creative Commons CC BY-NC 4.0 license.^[102] Copyright 2022, The American Association for The Advancement of Science. Valley transistor: f) Schematic illustration of resistance state modulation in Te valley transistors. $\Delta\epsilon$ denotes the energy separation between the Fermi level and the Weyl point. g) Dual-sweep transfer curves measured at $B = 0.1$ T. h) B^2 -dependent output curves measured at different states. Inset: Long-time retention of two non-volatile valley states. Reproduced under the terms of the Creative Commons CC BY license.^[103] Copyright 2022, Nature Publishing Group.

the on-state current, with the standard voltage supply in the commercial Si 10-nm node (0.7 V), in the most advanced 2D FETs can surpass that of state-of-the-art Si FETs. However, compared with those widely studied FETs based on other vdW semiconductors, particularly MoS_2 and InSe thin films, a systematic and comprehensive exploration of high-performance Te FETs is still lacking. Moreover, the channel length, on/off current ratio, and SS in Te FETs are significantly inferior to those in the most advanced n -type vdW FETs. On the other hand, considering that Te is a unique air-stable p -type vdW semiconductor with high room-temperature hole mobility, more resources should be dedicated to further exploiting the potential of Te FETs. Additionally, it is worth noting that an n -type Te FET has also been demonstrated by Qiu et al., as mentioned earlier.^[97] Although its highest on-state current reaches $200 \mu\text{A} \cdot \mu\text{m}^{-1}$ with a promising on/off current ratio of 10^3 , comparable to that of p -type Te FETs, this performance still has considerable room for improvement to match the state-of-the-art progress of 2D n -type FETs based on MoS_2 .

4.3. Topological Phase Change Transistors

The narrow bandgap of Te FETs results in low on/off current ratios at room temperature, which hinders their application in high-performance logic circuits. On the other hand, as a Weyl semiconductor with the Fermi level close to the Weyl point, Te can undergo a topological phase transition between a conventional semiconductor and a Weyl semimetal through electrostatic gate modulation, as illustrated in Figure 8a.^[102,103,148] The working mechanism of Te-based TPCT arises from the chiral anomaly current in Te crystals, which can be evidenced by typical magneto-transport signatures, including angle-dependent negative longitudinal magnetoresistance, planar Hall effect, and non-local transport.^[225] Under a positive gate voltage, the Fermi level moves away from the Weyl point, causing the Te TPCT to exhibit a low-conductance state similar to that of a conventional semiconductor, corresponding to the “OFF” state (left panel in Figure 8a). Conversely, when the Fermi level is near the Weyl

points under negative gate voltage, the TPCT displays the high-conductance state characteristic of Weyl semimetals, corresponding to the “ON” state (right panel in Figure 8a). Since the phase transition occurs only at a high carrier density under an intense external electric field, Chen et al. employed ionic electrolyte gating, using a solid-state polyethylene oxide (PEO)/LiClO₄ system, to design Te TPCTs (Figure 8b).^[102] Figure 8c,d compares the transfer curves of conventional Te FETs and Te TPCTs. When the temperature is reduced to 10 K, the conventional Te FET shows an on/off conductance ratio of 2.1×10^4 and an on-state conductance of $443 \mu\text{S} \cdot \mu\text{m}^{-1}$. In contrast, the Te TPCT, under a constant magnetic field of ≈ 5 T, achieves an extremely large on/off conductance ratio of 3.5×10^8 and an on-state conductance of $39 \text{ mS} \cdot \mu\text{m}^{-1}$ at a low operation voltage (≤ 2 V). These two performance metrics are significantly superior to those of monolayer MoS₂-based FETs and Si FinFETs (Figure 8e).^[226,227]

Leveraging the unique electronic structure of Te, Chen et al. also developed a valley transistor for low-power neuromorphic computing.^[103] Unlike TPCTs, in Te valley transistors, the shift of Fermi level close to the Weyl point, modulated by a negative gate voltage, generates high valley resistance. Conversely, moving the Fermi level away from the Weyl point under a positive gate voltage results in low valley resistance (Figure 8f). The nonvolatile valley states are achieved by ion insertion/extraction between the solid-state electrolyte and the Te channel, and the device exhibits a large hysteresis window under a low magnetic field of 0.1 T (Figure 8g). The linear curves clearly demonstrate two distinct set and reset states, and these nonvolatile valley states can persist for more than 10 000 s (Figure 8h). It is important to note that while solid-state electrolyte gating can induce a much higher external electric field than traditional MOSFET architectures, it typically operates at the cost of increased gate-source leakage current.

4.4. Other Electronics

In addition to its widespread use as a channel material in transistors, Te has also been applied in various other electronic devices, including the FG memory devices,^[116,117] piezoelectric/wearable nanogenerators,^[62,104–106,179] RF diodes,^[109] electrical switches,^[107,108,111] and more. The high carrier density and unique band structure of Te make it an ideal material for constructing FG memory devices. In 2023, Zha et al. reported a MoS₂/h-BN/Te vdW heterostructure-based FG memory device that exhibited a large ratio of 95.1% between the memory window range and the control gate sweeping range (Figure 9a), an impressive switching speed of ≈ 100 ns (Figure 9b), and high cycle endurance (>4000 cycles) along with retention stability (>4000 s) (Figure 9c and d).^[116] These performances are comparable to the most advanced flash memory devices enabled by vdW layered materials.^[228,229] The smallest constitutional unit of 1D helical molecular chains in Te nanostructures gives it a highly asymmetric crystal structure, which contributes to its strong piezoelectric effect.

In 2013, Lee et al. explored the design and fabrication of a piezoelectric nanogenerator (NG) based on Te nanowires.^[104] They first theoretically confirmed that piezoelectric voltage could only be generated when tensile stress was applied in the radial direction of the Te nanowires. Subsequently, the piezoelec-

tric nanogenerator was fabricated by embedding well-aligned Te nanowires in an SU8 layer and encapsulating them with two aluminum electrodes on a PI substrate. Experimental results demonstrated that as the number of Te nanowire layers increased, the output voltage and current rose from 0.3 to 1.0 V and from 15 to 60 nA, respectively (Figure 9e,f). Similarly, He et al. reported flexible and wearable nanogenerators based on ultrathin Te nanoflakes (Figure 9g).^[105] When attached to a human arm, these devices successfully harvested bioenergy by converting mechanical energy from repeated bending and straightening motions into electrical power. In addition to its piezoelectric applications, Te is also suitable for high-frequency electronics due to its high carrier mobilities. In 2023, Askar et al. studied the RF applications of Te nanoflakes.^[109] Their work involved the fabrication of two RF diodes: a passive RF mixer based on a Te-insulator-metal (TIM) diode and a zero-bias millimeter-wave power detector based on a Te-metal (TM) diode. When used as an upconverter, the TIM-based mixer demonstrated the capability to operate at frequencies even higher than the predicted (Figure 9h). For the TM-based detector, the responsivity at -20 dBm measured at 1 GHz reached $257 \text{ V} \cdot \text{W}^{-1}$ (Figure 9i). Although this research is still in its infancy, these results clearly demonstrate the significant application potential of Te in high-speed electronics. In Te FETs, avoiding a high Schottky barrier is crucial because it reduces carrier injection efficiency, consequently lowering the on-state current. However, Shen et al. developed a high-performance volatile switch centered around the Te-TiN contact, where the high Schottky barrier of ≈ 0.95 eV results in a low OFF-state current (Figure 9j).^[107] Unlike conventional chalcogenide-based selector switches, which often suffer from the chemical complexity of diverse chalcogenide compositions, the reported single-element Te switch exhibits a large drive current density ($>11 \text{ MA cm}^{-2}$) induced by the voltage pulse-triggered crystal-liquid melting transition of Te, an ultrafast switching speed (<20 ns), and a considerable on/off current ratio ($\approx 10^3$). The cycle endurance, tested by square voltage pulses, can reach 2×10^8 cycles (Figure 9k). In addition to vertical memristor, Li et al. also fabricated horizontal memristors based on 2D Te thin films, which hold potential for use as artificial synapses in neuromorphic computing.^[111] In summary, as a vdW semiconductor, the high carrier density, asymmetric crystal structure, and high carrier mobilities of Te ensure its suitability for a wide range of electronic applications.

As a brief summary of this section, Te's unique structural features and outstanding properties make it a promising material for the development of advanced electronics. The Te-based application discussed in this section clearly demonstrates its significant potential in shaping the future of electronic devices.

5. Optoelectronics

Optoelectronics is another important application branch for semiconductors, where the separation of photogenerated electron-hole pairs under an external or built-in electric field drives conductance changes or energy harvesting. Compared with traditional bulk semiconductors, vdW layered semiconductors typically exhibit stronger light-matter interactions, immunity to surface-induced performance degradation, and easier heterojunction construction due to the absence of

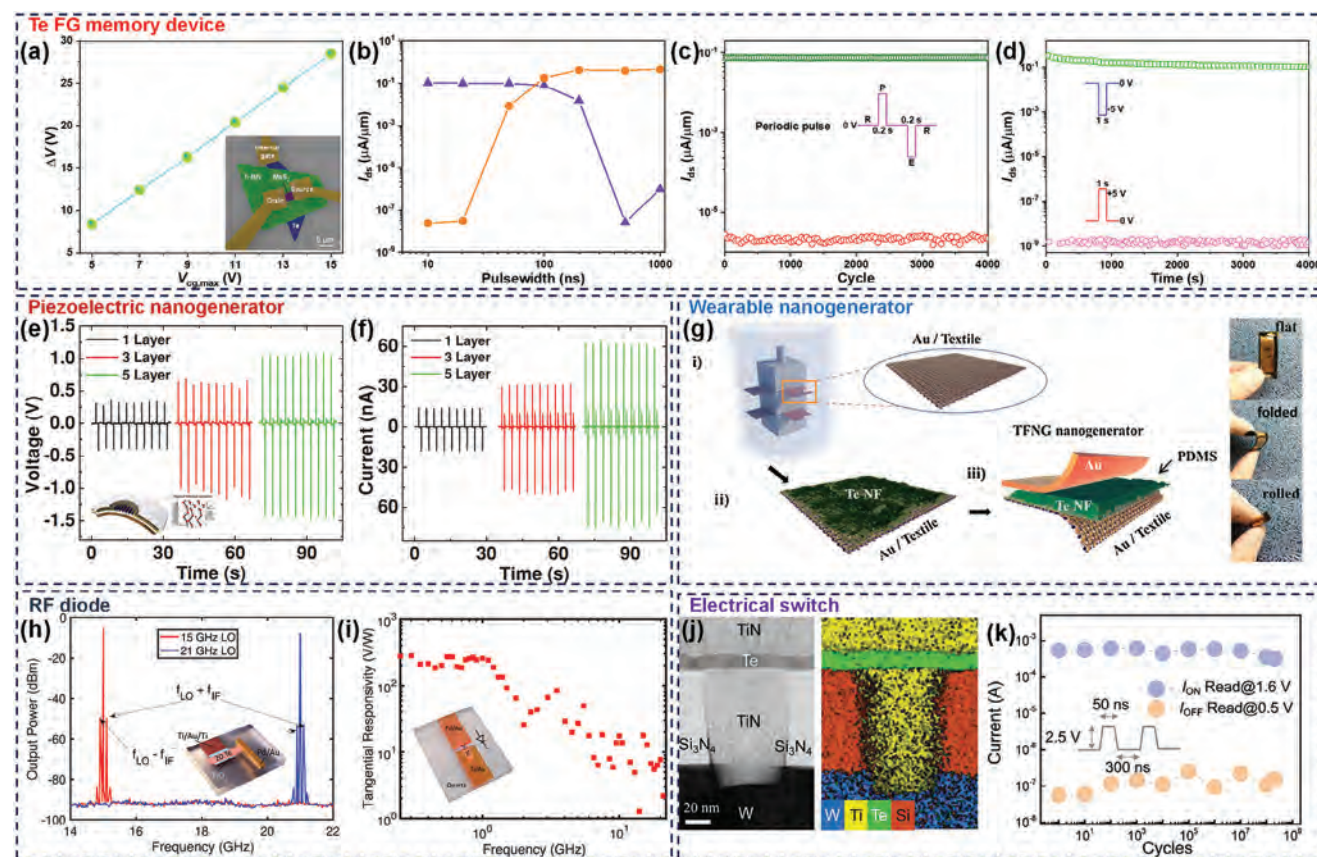


Figure 9. Other electronics enabled by Te nanostructures. Te FG memory device: a) Memory window as a function of maximum control gate voltage extracted from dual-sweep transfer curves. Inset: False-color SEM image of a Te FG memory device. b) Switching speed characterization of a Te FG device. c) Cycle endurance and d) retention stability of a Te FG device. Reproduced with permission.^[116] Copyright 2024, John Wiley & Sons, Inc. Piezoelectric generator: e) Output voltage and f) current measured on piezoelectric nanogenerators based on 1, 3, 5-layer Te nanowire thin films. Inset of (e) depicts a bent NG consisting of well-aligned t-Te nanowires. Reproduced with permission.^[104] Copyright 2013, John Wiley & Sons, Inc. Wearable generator: g) Schematic illustration of the wearable generator enabled by Te nanoflake (left) and optical images of the flat, folded, and rolled device (right). Reproduced with permission.^[105] Copyright 2017, Elsevier. RF diode: h) Output spectrum under a bias of -1.5 V for the TIM-based upconverter mixer enabled by Te. Inset: Schematic illustration of the TIM diode. i) Frequency-dependent tangential responsivity at -20 dBm measured on a TM diode enabled by a Te nanoflake. Inset: Schematic illustration of the TM diode. Reproduced under the terms of the Creative Commons CC BY license.^[109] Copyright 2023, Nature Publishing Group. Electrical switch: j) Cross-section TEM image and corresponding energy-dispersive spectroscopy elemental mapping of a single Te electrical switch. k) Cycle endurance of a single Te electrical switch. Reproduced with permission.^[107] Copyright 2021, The American Association for The Advancement of Science.

dangling bonds, which mitigates lattice mismatch issues.^[230–232] As Te nanocrystals transition from bulk to the monolayer limit, their bandgap increases from 0.31 to 1.04 eV, covering the short-wave infrared (SWIR: 1–3 μm) to mid-wave infrared (MWIR: 3–5 μm) range, thus opening avenues for their application in IR photodetectors.^[77,83,87,115,118,138,151,233–235] Additionally, the high carrier mobilities of Te can endow these IR photodetectors with fast switching speeds. Moreover, stacking or epitaxial growth of Te on other semiconductors can further broaden its operational spectrum.^[81,94,113,114,123,236–241] Leveraging its thermoelectric properties, Te-enabled photodetectors can also be designed to respond to broadband light.^[55,112,242] With the rise of the Internet of Things, Te nanocrystals are also being explored for use in developing advanced edge computing systems.^[116,117,124,243,244] Te-based optoelectronics is not limited to information technology applications; they also have potential in energy harvesting, particularly through the design and fabri-

cation of solar cells.^[119–122,245,246] In this section, we will explore Te-based optoelectronics and highlights its potential in future advanced optoelectronic devices.

5.1. Photodetectors

Photodetectors are ubiquitous in modern society, with their operational spectra largely determined by the bandgaps of the photoactive materials. Constructing IR detectors is particularly challenging because narrow bandgaps make them susceptible to thermal perturbations at room temperature, resulting in significant noise. Commercially available IR photodetectors are often made from complex compounds such as $\text{Hg}_x\text{Cd}_{1-x}\text{Te}$ and $\text{In}_x\text{Ga}_{1-x}\text{As}$, which typically involve expensive synthesis processes and require bulky cryogenic systems to suppress thermal noise for high specific detectivity.^[247] Despite these

challenges, high-performance IR photodetectors are crucial for a wide range of applications, including night vision, medical imaging, optical communication, and thermography.^[248] Compared with traditional materials, narrow-bandgap Te nanocrystals offer advantages for fabricating IR photodetectors, including straightforward synthesis methods, high immunity to thermal noise, and high carrier mobilities. Depending on their working mechanisms, Te-based photodetectors can generally be categorized into three types: photoconductive,^[44,45,77,83,84,118,151] photovoltaic,^[81,113,114,236,237,240,241,249–251] and photothermoelectric photodetectors.^[112,242,252] In photoconductive photodetectors, the photoconductive effect is the primary mechanism. In these devices, additional photogenerated carriers, stimulated by photons with energy exceeding the bandgap of the semiconductor, are accelerated under an external electric field, producing a photocurrent. In some cases, defect states within the bandgap can also contribute to the generation of photocarriers. In Te photovoltaic photodetectors, Te crystals are typically paired with *n*-type counterparts to form *p*–*n* junctions. The built-in electric field in the depletion region of the *p*–*n* junction helps separate the photo-generated electron-hole pairs, resulting in short-circuit current (I_{SC}) and open-circuit voltage (V_{OC}). This change in conductivity at zero bias, triggered by illumination, is the principle behind the design of photovoltaic photodetectors. Furthermore, the excellent thermoelectric properties of Te make it suitable for use in photothermoelectric photodetectors. In which devices, the temperature gradient induced by non-uniform light illumination or specifically designed metal nanostructures integrated with global light illumination can generate an electrical voltage for photodetection. This photoresponse is not limited by the bandgap, allowing Te photothermoelectric photodetectors to extend their response spectrum into the long-wave infrared (LWIR: 8–12 μm) region.

In 2018, Amani et al. designed a high-performance SWIR photodetector based on hydrothermal synthesized Te nanoflakes.^[77] To further enhance the light absorption, an optical cavity was created by depositing Al_2O_3 onto Au substrate, with the Te nanoflake then transferred onto the Al_2O_3 dielectric. The Au substrate served as both a back reflector and a back gate. After optimizing the Al_2O_3 thickness, the peak responsivity reaches $13 \text{ A}\cdot\text{W}^{-1}$ and $8 \text{ A}\cdot\text{W}^{-1}$ at 1.4 μm and 2.4 μm , respectively (Figure 10a). At an incident light wavelength of 1.7 μm , the specific detectivities are 2.9×10^9 Jones at room temperature and 2.6×10^{11} Jones at 77 K (Figure 10b). For most vdW semiconductor-based IR photodetectors reported at the laboratory stage, these figures of merit have typically been characterized using laser sources. This often leads to an overestimation of device performances due to incorrect calculations of optical power.^[253] In 2021, Peng et al. reported the blackbody response of Te-based IR photodetectors.^[87] Blackbody radiation is a type of source that can closely mimic the actual irradiation of the detected object, providing a more accurate measure of the practical application potential of the devices. Thanks to the fast carrier mobilities of Te, the fabricated IR photodetector exhibits a fast rise/fall time of 31.7/25.5 μs (Figure 10c). As shown by the dotted lines in Figure 10d, the blackbody peak photoresponsivity and specific detectivity reach $5.19 \text{ A}\cdot\text{W}^{-1}$ and 9.6×10^8 Jones at 1550 nm.

Leveraging the thermoelectric properties of Te, Dai et al. demonstrated an LWIR photodetector integrated with Au meta-

materials (Figure 10e).^[112] The polarization sensitivity of the designed metamaterials was first simulated using the Lumerical FDTD Solutions and HEAT packages (Figure 10f). The temperature distribution mapping provided in Figure 10g clearly indicates a significant temperature gradient localized around the device. The specially designed Au microstructure array endows this photothermoelectric photodetector with high polarization sensitivity (Figure 10h), and the responsivity can reach $410 \text{ V}\cdot\text{W}^{-1}$ (Figure 10i). Te can also be stacked with MoS_2 nanoflakes to build a *p*–*n* junction with high photosensitivity in SWIR region.^[113] This heterojunction was fabricated by Yao et al. using an all-dry transfer technique.^[254] Before stacking the MoS_2 and Te nanoflakes, graphene and h-BN nanoflakes were pre-transferred onto the SiO_2/Si substrate to serve as the gate electrode and dielectric, respectively. Under laser irradiation with an intensity of $12.4 \text{ mW}\cdot\text{cm}^{-2}$, the room-temperature responsivities reach 28.4, 4.0, and $0.87 \text{ A}\cdot\text{W}^{-1}$ at wavelengths of 0.98, 1.55 and 3.0 μm , respectively (Figure 10j). The corresponding peak-specific detectivities were 2.7×10^{10} , 3.4×10^9 , and 7.8×10^8 Jones, respectively (Figure 10k). In addition to MoS_2 nanoflake, Tao et al. reported the fabrication of Te/ ReS_2 heterojunction for high-performance phototransistors.^[114] In this work, the *p*-type 1D Te nanowire was stacked with the *n*-type 2D ReS_2 nanoflake to create a built-in electric field, improving the separation efficiency of photo-generated electron-hole pairs. When $V_g = 0 \text{ V}$ and the incident laser intensity was $22.6 \text{ mW}\cdot\text{cm}^{-2}$, the photocurrent approached $\approx 1 \mu\text{A}$ (Figure 10l). The peak responsivity and specific detectivity reached $180 \text{ A}\cdot\text{W}^{-1}$ and 5×10^9 Jones at a wavelength of 632 nm, respectively (Figure 10m).

However, Te photodetectors typically suffer from large dark currents due to their narrow bandgap. In 2023, Wang et al. designed a high-performance SWIR Te photodetector with asymmetric electrical source/drain contacts to address this issue.^[115] The significantly different Te-metal contact areas at the source and drain electrodes create varying degrees of band bending, which induces different photocurrents under light illumination and results in a net photocurrent observed in the device even under zero bias. A notable photocurrent of $\approx 20 \mu\text{A}$ is observed at $V_{ds} = 0 \text{ V}$, as shown in Figure 10n. The peak self-powered specific detectivity reaches 3.24×10^9 Jones (Figure 10o). You et al. reported the epitaxial growth of 1D Te onto 2D TMDs, forming vdW *p*–*n* heterostructures for high-performance self-powered photodetectors.^[81] Under zero source-drain and gate bias ($V_{ds} = V_{gs} = 0 \text{ V}$), the fabricated device exhibits significant photocurrent generation (Figure 10p). The exponent value of ≈ 0.73 in the power-law fitting of the laser intensity-dependent photocurrent is close to unity, indicating that the photoresponsivity of this device is less likely dominated by the photogating effect (Figure 10q).^[255,256] As a vdW narrow-bandgap semiconductor with high carrier mobility, Te holds significant potential for use in IR photodetectors. However, simple yet effective strategies need to be developed to reduce its dark current at room temperature.

In addition to the photodetectors discussed, it is worth noting that circular photogalvanic and photovoltaic effects (CPGE and CPVE) have also been observed in Te crystals.^[70,72,257–259] Both effects stem from the chiral crystal structure of Te. Specifically, in the case of CPGE, the three Weyl cones in the spin-split energy bands, created by strong SOC, result in two transition paths corresponding to wavelengths of 4.0 and 10.6 μm , which are

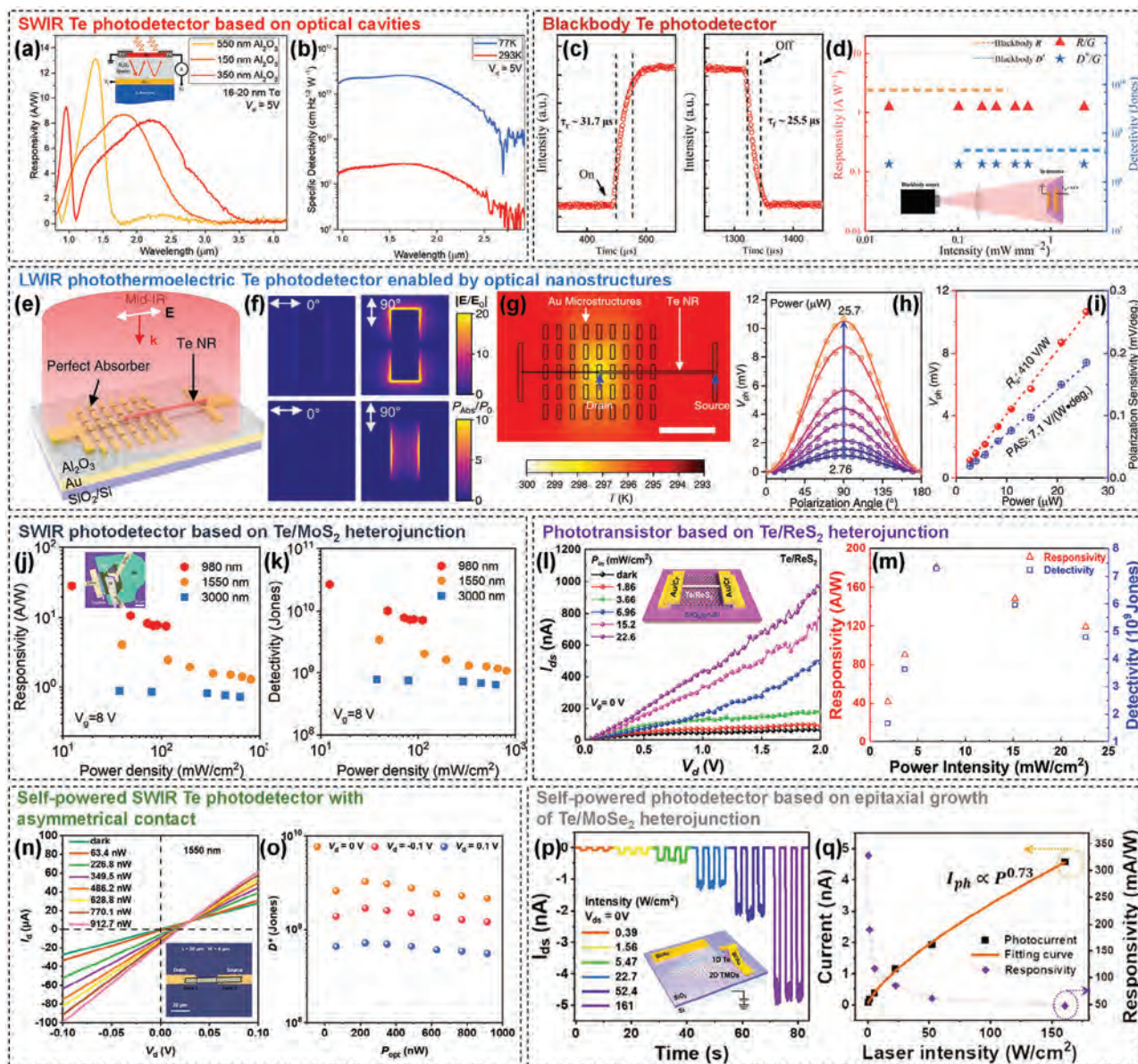


Figure 10. Various advanced photodetectors enabled by Te nanostructures. SWIR Te photodetector based on optical cavity: a) Photoresponsivity measured on Te photodetectors with optical cavities of varying Al_2O_3 thicknesses. Inset: Schematic illustration of the device. b) Specific detectivity of a Te photodetector measured at different temperatures. Reproduced with permission.^[77] Copyright 2018, The American Chemical Society. Blackbody room-temperature IR photodetector based on Te nanobelt: c) Switching speed characterization of a blackbody Te photodetector. d) Responsivity and specific detectivity measured under 1550-nm laser illumination, eliminating the gain (G) (triangle and pentagram) and blackbody calculation (dotted lines), respectively. Inset: Experimental setup. Reproduced under the terms of the Creative Commons CC BY-NC 4.0 license.^[87] Copyright 2021, The American Association for the Advancement of Science. LWIR photothermoelectric Te photodetector enabled by optical nanostructure with high polarization sensitivity: e) Schematic illustration of the device architecture. f) Simulated electric field and adsorption power distribution. g) Stimulated temperature mapping of the device with an input laser power of 30 mW. Scale bar: 10 μm . h) Polarization angle-dependent photoresponse under different light power levels. i) Output photovoltage and polarization sensitivity as a function of input light power. Reproduced under the terms of the Creative Commons CC BY license.^[112] Copyright 2023, Nature Publishing Group. SWIR photodetector based on Te/MoSe₂ heterojunction: j) Responsivity and k) specific detectivity as a function of input laser intensity at different wavelengths, measured on a SWIR photodetector. Inset of (j) shows the optical image of a typical device. Reproduced with permission.^[113] Copyright 2021, The Royal Society of Chemistry. Phototransistor based on Te/ReS₂ heterojunction: l) Output curves of a photodetector with $V_{\text{gs}} = 0$ under different laser intensities. Inset: Schematic illustration of the device. m) Laser intensity-dependent responsivity and specific detectivity. Reproduced with permission.^[114] Copyright 2021, The American Chemical Society. Self-powered SWIR Te photodetector with asymmetric contact: n) Output curves of a Te photodetector illuminated by a 1550-nm laser at different power levels. Inset: Optical image of a typical device. o) Laser power-dependent specific detectivity under different bias conditions. Reproduced with permission.^[115] Copyright 2023, John Wiley & Sons, Inc. Self-powered photodetector based on epitaxial growth of Te/MoSe₂ heterojunction: p) Current evolution of a device under different laser illumination with different intensities at zero bias. Inset: Schematic illustration of the device. q) Laser intensity-dependent photocurrent and photoresponsivity. Reproduced with permission.^[81] Copyright 2024, John Wiley & Sons, Inc.

sensitive to optical chirality.^[70] For CPVE, Niu et al. reported the formation of a *p–n* homojunction in a Te phototransistor by doping the Te channel through ALD of Al₂O₃, while the regions beneath the source/drain electrodes remained *p*-type.^[72] The built-in electric field near the contact region effectively separates photogenerated carriers, leading to a photoresponse at zero bias. The observed photocurrent is sensitive to circular polarization, induced by the interaction between polarized light and the spiral molecular chains in Te. These intriguing phenomena could pave the way for the development of Te-based circularly polarized light (CPL) photodetectors in the future.

5.2. Edge Computing

In conventional von Neumann computer architectures, the heavy data shuttling between computing and memory units limits running speed and leads to significant heat dissipation issues.^[260–263] The emerging concepts of in-sensor and in-memory computing offer promising solutions, particularly in light of the massive data proliferation on sensor-rich platforms like self-driving vehicles and wearable smart electronics. The development of in-sensor computing is therefore both significant and urgent.^[264] VdW layered semiconductors are an ideal material platform due to their high sensitivity to external stimuli, especially optical signals.^[265–275] However, most reported devices are limited to operation in the visible light region, and there is a strong demand for photoactive materials that can respond to IR light to enable in-sensor computing beyond the visible spectrum. Compared with those large bandgap vdW semiconductors, the narrow bandgap of Te covers the SWIR region, and its high IR responsivity makes it a promising candidate for optoelectronic memory devices operating in the IR region. Additionally, the high carrier density in Te offers the possibility of using it as a floating gate in flash memory devices. In 2022, Zha et al. reported an in-sensor reservoir computing (RC) system that operates in the optical communication band (1550 nm).^[124] The fabricated device, based on a Te/h-BN/graphene/CuInP₂S₆ heterostructure, exhibits both long-term potential/depression states triggered by electrical pulse trains and short-term memory behaviors triggered by 1550-nm laser pulse trains (Figure 11a,b). Leveraging the rich dynamics of this device, a fully memristive in-sensor RC system was simulated, achieving a recognition accuracy on Modified National Institute of Standards and Technology (MNIST) hand-written images comparable to the software baseline (Figure 11c). The RC design allows this system to require significantly fewer training operations than conventional artificial neural network (ANN) layers (Figure 11d).

In addition to its use as a channel material, Te can also serve as the floating gate in flash memory devices.^[116,117] Building on this, Zha et al. developed a multifunctional FG memory device based on a MoS₂/h-BN/Te vdW heterostructure for multimodal RC.^[116] This device not only demonstrates exceptional long-term electronic/optoelectronic memory behaviors due to the high charge density in the Te FG layer but also exhibits short-term memory characteristics, resulting from the combined effects of charge trap states in the MoS₂ channel and the Te FG layer (Figure 11e,f). The dual response to both electrical and optical signals enables the design of a multimodal RC system based

on this device (Figure 11g), which achieved a 90.77% recognition accuracy on the Neuromorphic-MNIST (N-MNIST) dataset (Figure 11h). Bach et al. also reported a similar vdW heterostructure for FG memory, where ReS₂ was used as the channel material instead of MoS₂.^[117] Compared with the study reported by Zha et al., this device exhibits a broader response spectrum extending into the NIR range, but it has smaller ratios between the memory window range and the sweeping range (Figure 11i). This difference can be attributed to the lack of overlap between the source/drain electrodes and the Te FG layer.^[276,277] Given that the bandgap of the RSe₂ nanoflake is 1.5 eV, the NIR response of this device is likely due to the photoresponse of the narrow-bandgap Te FG layer (Figure 11j). By applying electrical pulses and laser pulses at 532/980 nm as inputs, reconfigurable OR/AND logic gates were realized (Figure 11k,l).

Te can also be integrated with other layered materials for in-sensor computing. Yan et al. combined Te with α -In₂Se₃ to create a vdW heterojunction for neuromorphic computing (Figure 11m).^[123] The reported device functions as both a high-performance photodetector and an optoelectronic synapse. As a photodetector, it achieves high specific detectivities of 2.6×10^{11} and 7.5×10^{10} Jones at wavelengths of 1550 and 1940 nm, respectively. As an optoelectronic synapse, the device exhibits symmetric multi-bit long-term potential/depression (LTP/LTD) states with high linearity and repeatability (Figure 11n). A simulated neuromorphic computing model based on this device achieved recognition accuracy of over 90% even at a noise level of 60% (Figure 11o). These proof-of-concept studies highlight the potential of Te in future edge computing systems.

5.3. Photovoltaic Solar Cells

Te nanostructures have also been applied in the construction of photovoltaic solar cells for energy harvesting.^[59,119–122,245,246,278] Pokhrel et al. leveraged the advantages of Te nanowires, such as low defect density and enhanced photoconductivity, to design a high-performance photovoltaic device.^[119] The reported thin-film solar cell was developed from the existing CdTe photovoltaic technology, using a Te nanowire thin film as a buffer layer for the back contact of CdTe. To demonstrate the superiority of using Te nanowire thin films, *J–V* curves of solar cells with different back contacts—Cu/Au, Cu/Te nanowires/Au, CuCl₂/Au, and CuCl₂/Te nanowires/Au—were compared. The results revealed that the device based on CuCl₂/Te nanowires/Au exhibited the highest performance, with an open-circuit voltage of 846 mV, a short-circuit current density of 22.3 mA•cm^{−2}, a fill factor of 75.4%, and an efficiency of 14.6% (Figure 12a). Moreover, the external quantum efficiencies (EQE) of these devices exceeded 80% at a wavelength of ≈ 600 nm (Figure 12b). In 2019, Wu et al. conducted simulations integrating monolayer Te with TMDs for high-efficiency solar cells.^[120] In their first-principles DFT calculations, the bandgap of tellurene was set at 1.47 eV, with a mobility of up to 2.87×10^3 cm²•V^{−1}•s^{−1}. The results revealed that Te/MoTe₂ and Te/WTe₂ heterojunctions exhibit a broader optical absorption range and higher absorption coefficient than bare Te, MoTe₂, and WTe₂ (Figure 12c). The power conversion efficiency (PCE) of Te/TMDs heterojunctions was predicted to be 22.5% for WTe₂ and 20.1% for MoTe₂ (Figure 12d). These findings suggest

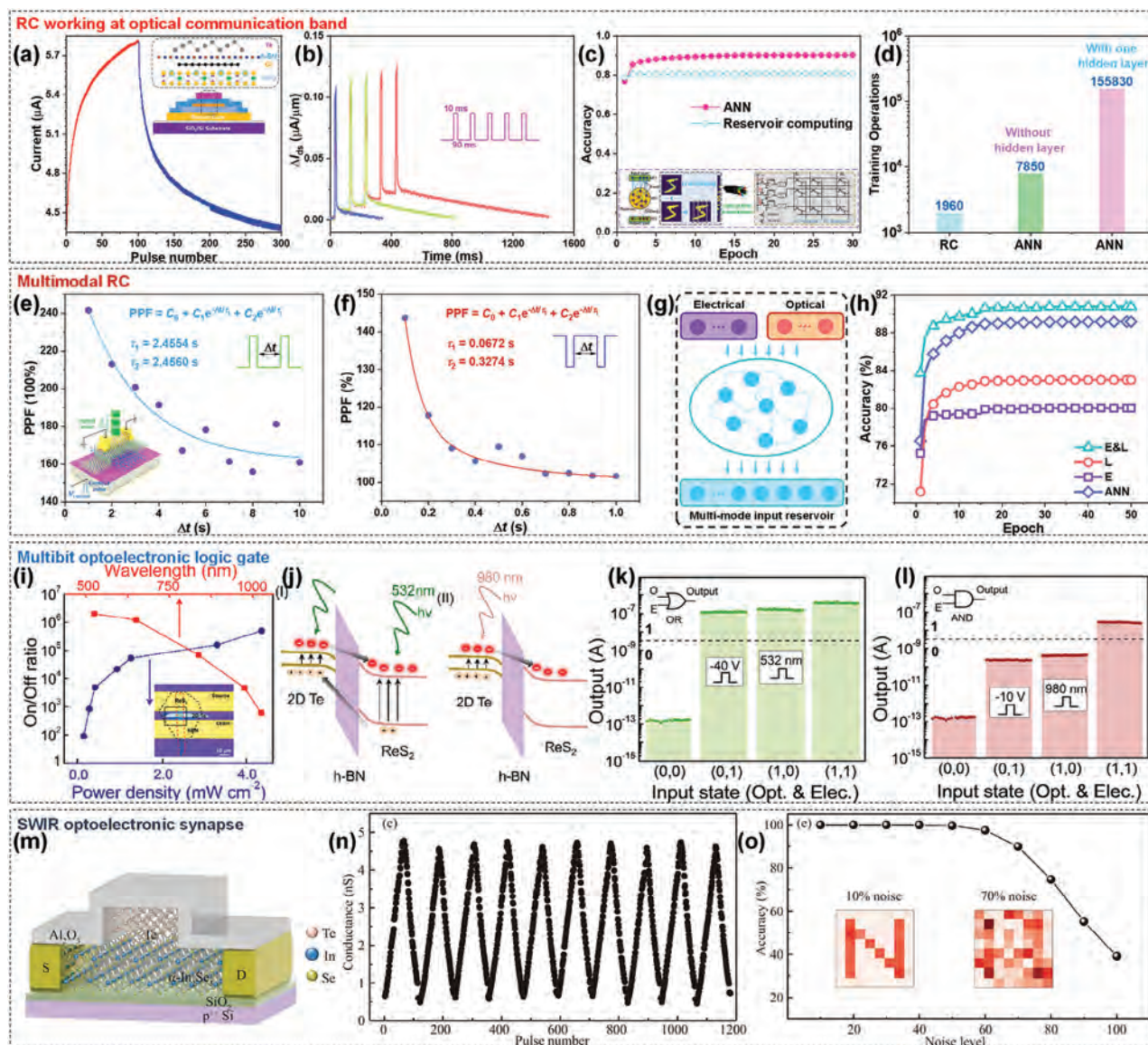


Figure 11. Te-based optoelectronics for edge computing. Te-based optoelectronic memory device for RC working at the optical communication band: a) Multibit memory states modulated by electrical pulse trains. Inset: Schematic illustration of the Te-based optoelectronic memory device. b) Short-term optoelectronic memory triggered by 1550-nm laser pulse trains. c) Comparison of recognition accuracy of MNIST hand-written digits between the stimulated RC network based on the device and software baseline. d) Comparison of the number of operations needed for RC, ANN without, and with one hidden layer. Reproduced with permission.^[124] Copyright 2023, John Wiley & Sons, Inc. Te FG optoelectronic memory device for multimodal RC: PPF triggered by e) 532-nm laser pulse pairs and f) electrical pulse pairs with different interval. Inset of (e) depicts the device architecture. g) Schematic illustration of multimodal RC with both electrical and optical pulses as inputs. h) Comparison of N-MNIST digit recognition accuracy for RC operating in different modes and the software baseline. Reproduced with permission.^[116] Copyright 2024, John Wiley & Sons, Inc. Multibit optoelectronic logic gate based on Te FG optoelectronic memory device: i) On/off current ratios as functions of laser intensity and wavelength. Inset: Optical image of a typical device. j) Energy band diagram of the device under 532-nm laser illumination (left panel) and 980-nm laser illumination (right panel). Output current using the device as k) an OR and l) an AND gate, with the electrical pulse and 532-nm/980-nm laser pulses as inputs. Reproduced with permission.^[117] Copyright 2024, The American Chemical Society. NIR optoelectronic synapse made from Te: m) Schematic illustration of the device architecture. n) LTP/LTD triggered by 1550-nm laser pulse and electrical pulse trains, respectively. o) Noise level-dependent recognition accuracy. Insets: Output images of 10% and 70% noise level, respectively. Reproduced with permission.^[123] Copyright 2023, Science Press (China).

that monolayer Te could be a promising candidate for future solar cells.

Te nanowires can also replace noble metals like Pt or Au in expensive, high-performance Si nanowire-based liquid-junction solar cells (LJSCs) (Figure 12e).^[121] By tethering Te nanowires

over Si nanowires and coating them with carbon, the power conversion efficiency of LJSCs reaches $\approx 67\%$ (Figure 12f). Mousavi-Kamazani et al. also reported a simple sonochemical strategy for synthesizing Te nanoparticles, with sizes ranging from 15 to 40 nm, for solar cell applications.^[122] Interestingly, after

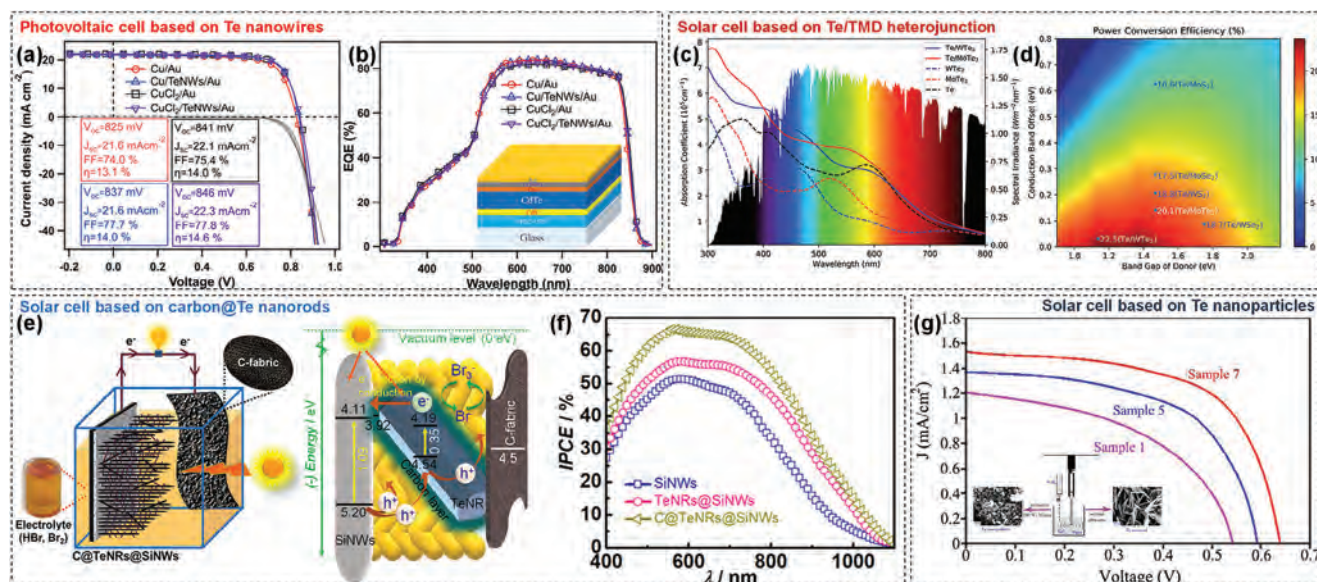


Figure 12. Different Te nanostructures for photovoltaic applications. Photovoltaic cell based on Te nanowires: a) Comparison of J - V curves and b) EQE of CdTe photovoltaic cells with Cu/Au, Cu/Te nanowires/Au, CuCl₂/Au, and CuCl₂/Te nanowires/Au back contacts. Inset of (a) summarizes the open-circuit voltage, short-circuit current, fill factor, and efficiency of the corresponding devices. Inset of (b) shows the device architecture. Reproduced under the terms of the Creative Commons CC BY-NC 3.0 license.^[119] Copyright 2020, The Royal Society of Chemistry. Solar cell based on Te/TMD heterojunction demonstrated by first-principle DFT calculations: c) Calculated absorption spectra of Te, MoTe₂, WTe₂, Te/MoTe₂, and Te/WTe₂. d) Calculated power conversion efficiency of solar cells based on Te/TMDs heterojunctions. Reproduced with permission.^[120] Copyright 2019, The Royal Society of Chemistry. Solar cell made from carbon@Te nanorods anchored to a Si nanowire scaffold: e) Schematic illustration of the solar cell under measurement with solar illumination and the corresponding band diagram. f) Comparison of wavelength-dependent power conversion efficiency in solar cells based on Si nanowires, Te nanorods anchored to a Si nanowire scaffold, and carbon@Te nanorods anchored to a Si nanowire scaffold. Reproduced with permission.^[121] Copyright 2019, The American Chemical Society. Solar cell based on sonochemical-synthesized Te nanoparticles: g) Comparison of J - V curves measured on solar cells made from Te nanoparticles with different morphologies. Sample 1: Te nanorod; Sample 5: sphere-like Te nanoparticle; Sample 7: Rice-like nanoparticle. Reproduced with permission.^[122] Copyright 2017, Elsevier.

evaluating the J - V curves of quantum dot-sensitized solar cells fabricated with Te nanoparticles of different morphologies—including Te nanorod (sample 1), sphere-like Te nanoparticle (sample 5), and rice-like Te nanoparticle (sample 7)—the authors found that the morphology of the Te nanoparticles significantly impacts device performance (Figure 12g). The high conductivity and appropriate bandgap of Te nanoparticles make them an appealing candidate for high-performance photovoltaic devices.

Electronics and optoelectronics are the two most critical application areas for semiconductors. Compared with traditional 3D semiconductors, vdW layered semiconductors offer advantages such as reduced short-channel effect, immunity to surface-induced performance degradation, and stronger light-matter interactions. Additionally, this unique material platform is highly compatible with conventional CMOS technology, making it a valuable supplement to the Si industry. Among various vdW semiconductors, Te has been increasingly attracted the attention of researchers due to its p -type semiconducting nature, high hole mobility, air stability, and narrow bandgap that covers the SWIR and MWIR regions. These appealing properties are likely to make Te a prominent material in the coming decades.

6. Sensors

In addition to photodetectors, other sensors—including chemical sensors, physical sensors, and gas sensors—play an indis-

pensable role in our daily lives. Unlike the electronics discussed in the previous section, where conductance is primarily modulated by an external electric field, the response of the sensors illustrated in this section is mainly reflected by resistance changes triggered by environmental stimuli such as metal ions, acid or alkaline solutions, strain, and toxic gases. The selection of an active material is crucial for developing high-sensitivity sensors. Te nanocrystals, composed of 1D molecular chains, possess a unique crystal structure that provides an extremely large surface-to-volume ratio with abundant surface-active sites, leading to high surface activity, making them ideal for use in chemical and gas sensors.^[125,126,132–135,279–285] Additionally, the piezoelectric properties arising from the helical molecular chains in Te expand its applications into nanoforce sensing.^[128–131] This section focuses on studies related to various sensors based on Te nanostructures.

6.1. Chemical Sensors

Given that gas sensors typically operate based on chemical reactions, “chemical sensors” in this review refer to Te-based devices that respond to metal ions in solution, as well as to acidic solutions. This distinguishes them from Te-based gas sensors, which will be discussed in detail in section 6.3. In 2013, Wei et al. synthesized Te nanotubes for detecting and removing Hg²⁺

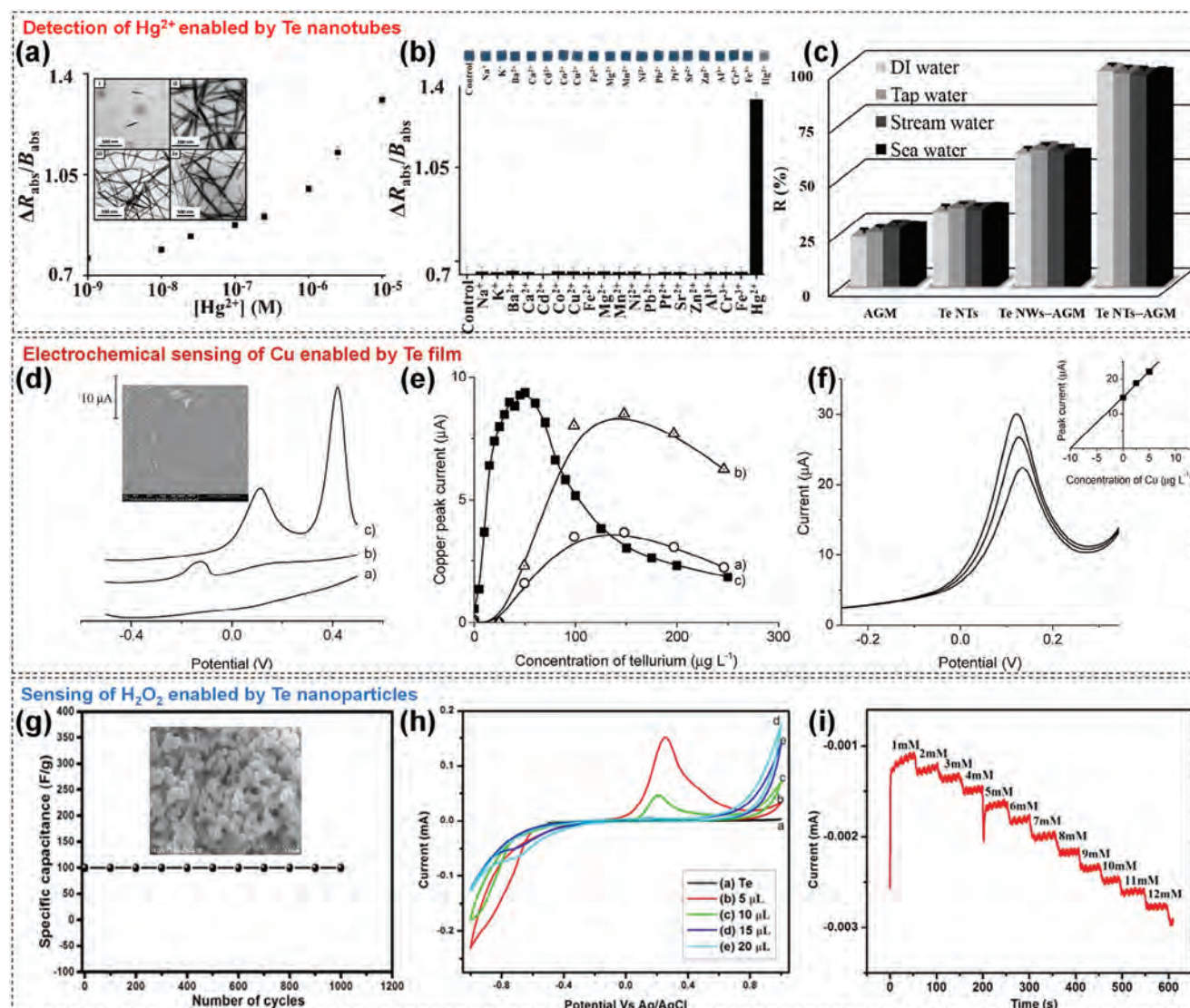


Figure 13. Various chemical sensors enabled by Te nanostructures. Detection of Hg^{2+} enabled by Te nanotubes: a) Ratio of the blue component to the red component of the Te nanotubes-modified agarose gel membrane as a function of Hg^{2+} concentration. Inset: TEM images of Te nanotubes synthesized under different experimental conditions. b) Detection selectivity towards Hg^{2+} . c) Comparison of Hg^{2+} removal efficiency in DI water, tap water, stream water, and sea water by AGM, Te nanotubes, Te nanowires-modified agarose gel membrane, and Te nanotubes-modified agarose gel membrane. Reproduced with permission.^[125] Copyright 2013, The Royal Society of Chemistry. Electrochemical sensing of Cu enabled by Te film: d) Effect of the Te film on Cu response, recorded as square wave voltammograms in different examined solutions. (a: 0.1 M HCl; b: 0.1 M HCl and 60 $\mu\text{g}\cdot\text{L}^{-1}$ of Cu; c: 0.1 M HCl, 60 $\mu\text{g}\cdot\text{L}^{-1}$ of Cu, and 150 $\mu\text{g}\cdot\text{L}^{-1}$ of Te) Inset: SEM image of the glassy carbon surface after depositing Te films. e) Cu peak current as a function of Te concentration in different examined solutions. f) Detection of Cu in mineral water. Inset: Corresponding standard addition plot. Reproduced with permission.^[126] Copyright 2017, Elsevier. Sensing of H_2O_2 enabled by Te nanoparticles: g) Cycle endurance of the supercapacitor enabled by Te nanoparticles at 30 $\text{mA}\cdot\text{cm}^{-2}$. Inset: Field emission scanning electron microscopy (FESEM) image of the synthesized Te nanoparticles. h) Current–voltage curves for the glassy carbon electrode (GCE)/Te/Nf with different H_2O_2 concentration. i) Current evolution with the addition of H_2O_2 . Reproduced with permission.^[127] Copyright 2017, Elsevier.

ions.^[125] The sensor, which was constructed using Te nanotubes-modified agarose gel membrane (AGM), operated based on the strong hybridization and galvanic replacement reaction between Te and Hg. The performance of the device was evaluated using a color analysis strategy developed with ImageJ software. The detection limit, determined by a signal/noise ratio of 3, was ≈ 10 nM for Hg^{2+} (Figure 13a), and the device demonstrated high selectivity for Hg^{2+} , as shown in Figure 13b. In addition to its de-

tection capabilities, the Te nanotube-based membrane achieved a removal efficiency of $>97\%$ for Hg^{2+} in deionized (DI) water (Figure 13c). Subsequently, Bobrowski et al. introduced an electrochemical technique called anodic stripping voltammetry (ASV) for detecting Cu ions.^[126] Figure 13d illustrates the response of a Te thin film deposited on a glassy carbon electrode (Te/GC electrode) in square wave voltammograms across different solutions, confirming the effectiveness of this approach for

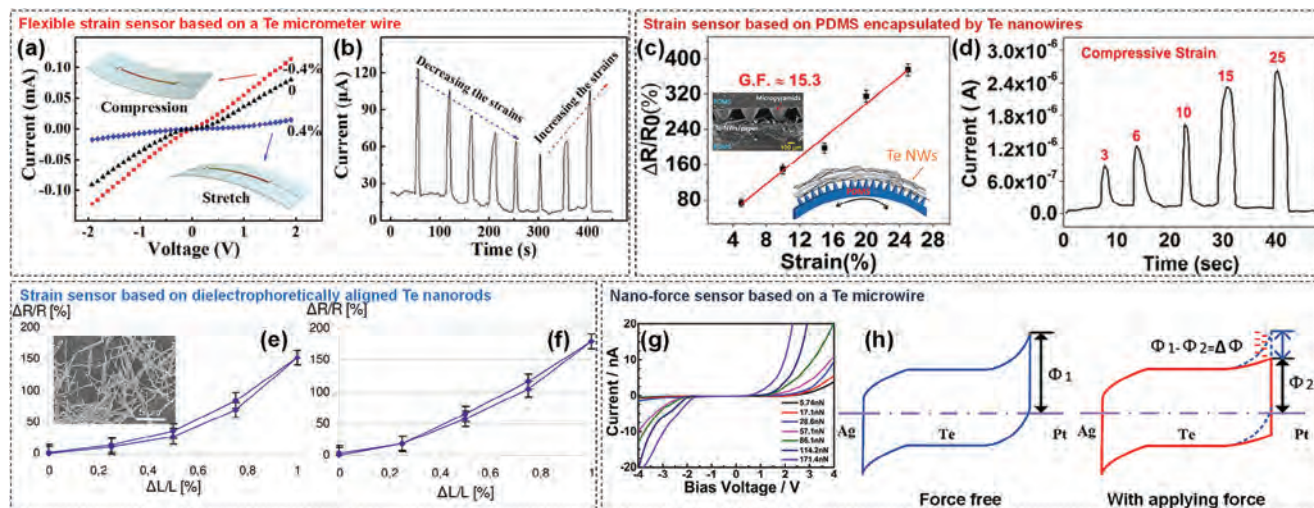


Figure 14. Various physical sensors enabled by Te nanostructures. Flexible strain sensor based on a Te micrometer wire: a) I – V curves of a Te micrometer wire measured under different strain forces. Insets: Schematic illustration of the bending movements. b) Current evolution with decreasing/increasing strain. Reproduced with permission.^[128] Copyright 2014, IOP Publishing, Ltd. Strain sensor based on PDMS encapsulated by Te nanowires: c) Strain-dependent resistance variation. Insets: Cross-section TEM image of PDMS film encapsulated by Te nanowires (top) and schematic illustration of the sensor architecture (bottom). d) Current evolution under compressive strain. Reproduced with permission.^[129] Copyright 2021, IOP Publishing, Ltd. Strain sensor based on dielectrophoretically aligned Te nanorods: Strain-dependent resistance variation measured on sensors fabricated on e) PI-foil and f) PET-foil. Inset of (e) provides the SEM image of the synthesized Te nanorods. Reproduced with permission.^[130] Copyright 2009, Elsevier. Nanoforce sensor based on a Te microwire: g) I – V curves measured on a Te microwire under different forces. h) Energy band diagram of the Te microwire without (left)/with (right) applied force. Reproduced with permission.^[131] Copyright 2017, IOP Publishing, Ltd.

Cu ion detection. Since this method relies on the chemical reaction between Te and Cu, the peak current measured by the Te/GC electrode is highly dependent on the Te concentration in the electrolyte (Figure 13e). The reliability of this technique was further validated by accurately determining a Cu concentration of $9.3 \pm 0.8 \mu\text{g}\cdot\text{L}^{-1}$ in a mineral water sample (Figure 13f). Manikandan et al. integrated Te nanoparticles into a high-performance supercapacitor designed as a non-enzymatic H_2O_2 sensor.^[127] The fabricated supercapacitor demonstrated high cycle endurance, featuring graphite foil and glassy carbon electrodes coated with Te nanoparticles (Figure 13g). The linear decrease of peak current values at ~ -0.8 V in the I – V curves, observed with the successive addition of H_2O_2 , highlights the sensitivity of this supercapacitor to H_2O_2 (Figure 13h). This sensitivity is further confirmed by the current evolution curve (Figure 13i). Beyond Te-based supercapacitors for chemical sensing, Manoharen et al. developed wearable supercapacitors through the electrochemical deposition of vertically aligned Te nanorods on flexible carbon cloth.^[286] This energy storage device, which exhibits high capacitance, significant energy density, and remarkable endurance, has potential applications in powering portable electronic devices. The abundant surface-active sites in Te nanostructures contribute to a high chemical reaction efficiency, resulting in the high sensitivity to target chemicals observed in these devices.

6.2. Physical Sensors

Sharing the same physical mechanism as previously introduced nanogenerators centered around Te nanostructures, the piezoelectric properties of Te enable physical sensors to convert

nanoforces into electrical signals, making them highly effective for strain sensing.^[128–131] Liang et al. reported a flexible strain sensor based on a single ultralong Te nanowire.^[128] In fabricating this device, the Te nanowire, measuring several millimeters in length, was placed on a polystyrene (PS) substrate with its ends fixed using silver paste. After annealing the structure at 80°C in vacuum for 10 h, the entire device was encapsulated in PDMS to enhance its stability. The device exhibited a negative current response under tensile strain and a positive current response under compressive strain, compared with the unstrained condition (Figure 14a). The effectiveness of the device was further validated by observing current variations with increasing or decreasing compressive strains (Figure 14b). Selamneni et al. designed a highly sensitive strain sensor by patterning PDMS with a micropillar structure using a laser-assisted engraving process and integrating it with Te nanowires.^[129] The linear relationship between resistance variation and applied strain (Figure 14c), as extracted from the current evolution under different compressive strains (Figure 14d), corroborates the responsivity of the device to strain forces. Nocke et al. developed a novel strain sensor by employing a dielectrophoretically align strategy to create Te nanorod thin films, which were then embedded in polymer elastic substrates.^[130] The resistance variation under different strain forces was compared for devices using PI and PET foils as substrates (Figure 14e,f). As revealed by Kou et al., the distinct I – V characteristics observed under varying strains in Te-based strain sensors are attributed to nanoforce-induced variations in Schottky barrier height (Figure 14g,h). The piezoelectric properties, derived from the highly asymmetric crystal structure and high conductance of Te nanocrystals, grant them significant potential for future applications in advanced strain sensors. However, critical

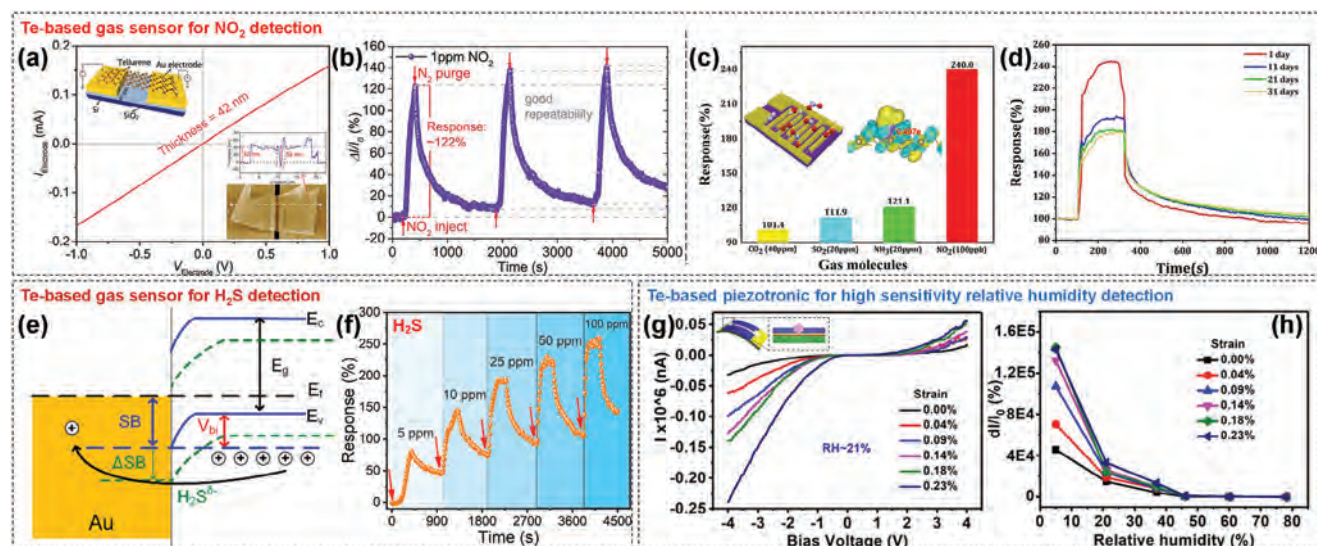


Figure 15. Various gas sensors enabled by Te nanostructures. Te-based gas sensor for NO_2 detection: a) I - V curve measured on a Te gas sensor. Insets: Schematic illustration of the device architecture (top) and AFM characterization of the Te nanoflake (bottom). b) Current response to NO_2 . Reproduced with permission.^[132] Copyright 2019, The Royal Society of Chemistry. c) NO_2 selectivity of a Te gas sensor. Insets: Schematic illustration of the device architecture (left) and electron transfer between Te and NO_2 atoms (right). d) Long-term stability of the Te gas sensor. Reproduced with permission.^[133] Copyright 2020, The American Chemical Society. Te-based gas sensor for H_2S detection: e) Energy band diagram depicting the charge transfer between Te and H_2S . f) Current evolution in response to different concentrations of H_2S . Reproduced with permission.^[134] Copyright 2020, The American Chemical Society. Te-based piezotronics for water molecule detection: g) I - V curves measured at 21% humidity under different strains. h) Relative humidity-dependent current change under different strains. Reproduced with permission.^[135] Copyright 2019, IOP Publishing, Ltd.

issues such as device endurance need further exploration for successful commercialization.

6.3. Gas Sensors

Similar to their application in chemical sensors, the abundant surface-active sites in 1D vdW Te semiconductors make them ideal candidates for fabricating gas sensors as well.^[132–135,280–285] Chemiresistive-type 2D gas sensors generally operate based on electron transfer between the active material and gas molecules. The electrical resistivity of the 2D channel can be effectively altered by oxidizing gas molecules (e.g., NO_2 and NO) that withdraw electrons, or by reducing gas molecules (e.g., NH_3 and CH_4) that donate electrons.^[287] As a p -type vdW semiconductor, the conductivity of Te crystals typically increases with oxidizing gas molecules and decreases with reducing gas molecules. Additionally, the electron donation or acceptance by gas molecules modulates the Fermi level position, which in turn alters the Schottky barrier height at the contact between the Te channel and the metal electrode, further impacting device conductivity. In 2019, Wang et al. designed Te-based conductors for NO_2 sensing.^[132] The 42-nm thick Te channel demonstrated high conductivity (Figure 15a), and the conductance evolution triggered by NO_2 injection showed high repeatability (Figure 15b). Thanks to the high air stability of Te nanoflakes, the gas sensor fabricated by Cui et al. not only exhibited high selectivity for NO_2 (Figure 15c) but also maintained excellent long-term stability over one month (Figure 15d). In addition to NO_2 , Te also responds to H_2S through charge transfer, as demonstrated by Wang et al. (Figure 15e).^[134] The reported gas sensor, based on a Te nanoflake with ohmic

contact, exhibited high sensitivity to H_2S even at a low concentration of 1 ppm (Figure 15f). Interestingly, Kou et al. reported strain-enhanced sensitivity to water molecules in Te-based piezotronics.^[135] This device had a similar device architecture to the previously introduced Te-enabled strain sensor. Under different strain conditions, the device displayed distinct current responses at a humidity of $\approx 21\%$ (Figure 15g), with the highest humidity sensitivity observed under a strain of 0.23% (Figure 15h).

In summary, Te nanostructures have shown significant potential for application in various sensor devices, including chemical, physical, and gas sensors, thanks to their high surface-volume ratios and asymmetric crystal structures. While many challenges remain to be addressed on the path to the commercialization of Te-based sensors, Te, as an emerging 1D vdW semiconductor with numerous intriguing properties, warrants further research and development to advance its applications in this field.

7. Large-Scale Circuits

The preparation of large-scale polycrystalline Te thin films was first reported over half a century ago,^[40,167,174,288,289] but it did not become central to the fabrication of large-scale circuits until its recent resurgence.^[89,91,95,136,137] As a unique p -type vdW semiconductor with high air stability, significant carrier mobility, and impressive IR response, Te is poised to play a crucial role in the development of future advanced integrated circuits and IR imaging systems. At the time of writing, preliminary explorations of Te thin films in applications such as logic circuits,^[89] large-scale vertically interconnected CMOS,^[91] oscillation ring,^[136] large-scale Te FET array,^[95] and NIR imaging array^[137] have shown promising progress.

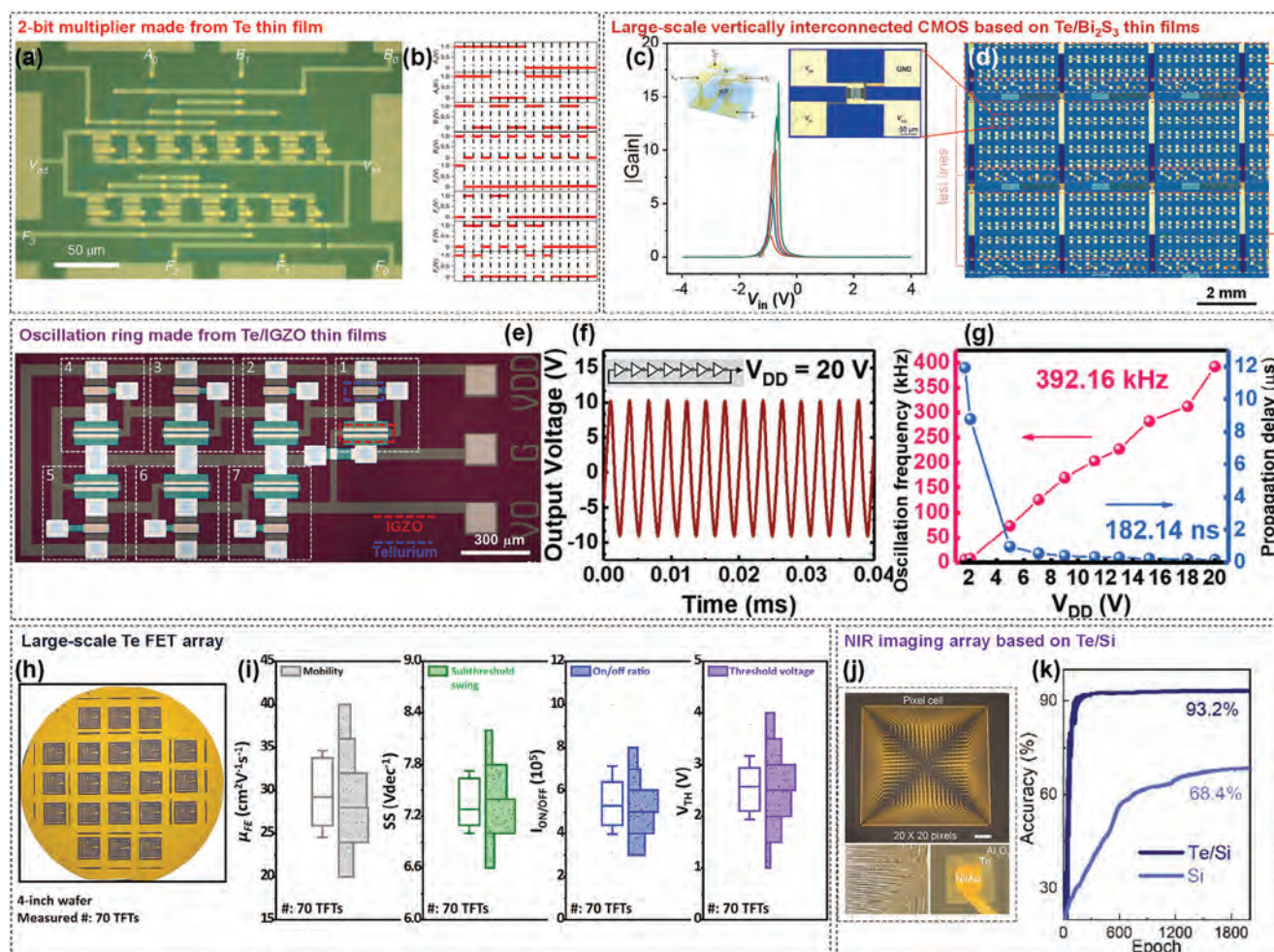


Figure 16. Large-scale circuits based on Te thin film. 2-bit multiplier made from Te thin film: a) Optical image and b) output voltage of a 2-bit Te-based multiplier. Reproduced with permission.^[89] Copyright 2020, Nature Publishing Group. Large-scale vertically interconnected CMOS based on Te/Bi₂S₃ thin films: c) Voltage gain curves measured on a vertically interconnected CMOS under different supply bias. Insets: Schematic illustration of the device architecture (left) and an optical image of a CMOS device (right). d) Optical image of the CMOS array. Reproduced with permission.^[91] Copyright 2023, John Wiley & Sons, Ltd. Oscillation ring made from Te/IGZO thin films: e) Optical image of an oscillation ring consisting of 7 CMOS circuits. f) Output voltage of the seven-stage ring oscillator. g) Oscillation frequency and propagation delay as a function of supply bias. Reproduced with permission.^[136] Copyright 2023, Elsevier. Large-scale Te FET array: h) Photograph of the large-scale Te FET array on a 4-inch wafer. i) Statistics of the mobility, SS, on/off current ratio, and threshold voltage measured on 70 Te FETs from the wafer-scale Te FET array. Reproduced under the terms of the Creative Commons CC BY license.^[95] Copyright 2022, Nature Publishing Group. NIR imaging array based on CMOS-compatible Te/Si: j) Photograph of the NIR imaging array (top panel) and optical images of the connection wires and a single pixel (bottom panel). k) Comparison of image recognition accuracy between Te/Si arrays and Si arrays. Reproduced with permission.^[137] Copyright 2023, John Wiley & Sons, Ltd.

In 2020, Zhao et al. developed a low-temperature (−80 °C) evaporation method for the growth of large-scale polycrystalline Te thin films, which enabled the demonstration of complex logic circuits.^[89] Figure 16a shows the optical image of a 2-bit multiplier consisting of 39 p-MOS made from Te thin films. The output curves measured from this circuit block indicate that the fabricated multiplier functions effectively, with a maximum output voltage loss of just 3% (Figure 16b). Thanks to the low deposition temperature, Te thin films can be deposited not only on rigid SiO₂/Si substrate but also on polymer substrates, enabling the development of flexible electronics. Compared with the large-scale logic circuits composed of single-polarity transistors used as both load and driver—known as pseudo-*n/p*-MOS architectures—CMOS technology, which utilizes two channel

materials with different majority carrier types, offers significant energy efficiency due to its greatly reduced static current.^[290–295] Ran et al. reported the fabrication of large-scale vertically interconnected CMOS circuits based on thermally evaporated Te and Bi₂S₃ thin films (Figure 16c,d).^[91] The fabrication process begins with the deposition of patterned Bi₂S₃ channels on a SiO₂/Si substrate. Electron beam evaporation (EBE) was then used to deposit Ti/Au (10/15 nm) electrodes at both ends of the *n*-type Bi₂S₃ thin film channel. Next, a 20-nm Al₂O₃ layer was deposited via ALD as the dielectric. On top of this layer, In/Au (5/15 nm) was deposited via EBE to serve as the common gate, followed by the deposition of another 20-nm Al₂O₃ layer as the dielectric for the top *p*-type Te FET. Subsequently, the *p*-type Te channel was prepared through thermal evaporation. Finally, Pd/Au (5/30 nm) was chosen as

the source/drain electrodes for the Te FETs. The connection between the B_2S_3 and Te FET was achieved through a hole filled with Ti/Au. The constructed 3D CMOS circuit demonstrated a high voltage gain of 17 at $V_{dd} = 4$ V. In another study, Kim et al. connected seven Te-indium gallium zinc oxide (IGZO) CMOS inverters end to end to design an oscillation ring. This ring operates stably within a voltage range of up to 20 V, achieving a working frequency of 392.16 kHz at this driven voltage, with a propagation delay of 182.14 ns (Figure 16e–g). Kim et al. also achieved wafer-scale uniformity of polycrystalline Te thin films by depositing them via magnetron sputtering at room temperature on 4-inch wafers, ensuring the integrity of Te FETs (Figure 16h).^[95] An investigation of 70 devices from the Te FET array demonstrated high performance uniformity, with an average field-effect carrier mobility of $\approx 30 \text{ cm}^2 \cdot \text{V}^{-1} \cdot \text{s}^{-1}$, an SS of $\approx 7 \text{ V} \cdot \text{dec}^{-1}$, an on/off current ratio of $\approx 10^5$, and a threshold voltage of ≈ 2.5 V (Figure 16i). Beyond electronic circuits, Te has also been utilized in constructing large-scale IR imaging arrays. Recently, Li et al. developed a Te/Si NIR photodetector using CMOS-compatible technology.^[137] In this work, high-quality Te thin films were deposited onto an *n*-type Si substrate via magnetron sputtering to form a type II Te/Si heterojunction. Using the prepared *p*–*n* junction, a 20×20 pixel NIR imaging array was demonstrated, achieving high-contrast photoelectric imaging (Figure 16j). By integrating the imaging array with an ANN, the researchers created an artificially simulated vision system that achieved significantly higher imaging recognition accuracy than Si-based imaging array (Figure 16k). In 2024, Zhang et al. extended the spectrum of Te-based imaging array to the terahertz (THz) band.^[296] The authors demonstrated a mixed-dimensional homojunction based on 1D Te nanowires and 2D Te nanofilms for dynamic large-array multi-color displays, successfully producing painting colors under specific pump conditions.

Although still in its early stages, the successful demonstration of large-scale circuits based on Te thin films, as introduced in this section, is of significant reference value and paves the way for the future design and fabrication of Te-based large-scale circuits.

8. Conclusions and Outlooks

The past few decades have seen rapid advancements in artificial intelligence, which have greatly enhanced our daily lives but also introduced new demands for advanced electronics and optoelectronics hardware. As the Si industry approaches its physical limits, the solving of Moore's law is driving researchers to explore new material platforms and develop novel computing diagrams beyond the von Neumann architecture, aiming to improve both computing and energy efficiency. In this context, the emergence of vdW layered materials offers a promising alternative. Unlike conventional bulk semiconductors, vdW layered materials, due to their atomically thin nature and lack of dangling bonds at the surfaces, typically exhibit stronger light-matter interaction per volume, greater immunity to short-channel effects and surface-induced performance degradation, and easier heterostructure construction. However, most commonly used air-stable vdW layered semiconductors exhibit *n*-type or *n*-type dominated transport behaviors. The absence of a *p*-type counterpart with comparable performances has become a significant limitation, hindering researchers from fully exploring the potential ap-

plications of the vdW material family in advanced electronics and optoelectronics.

The recently rediscovered vdW semiconductor Te offers a promising solution. As a naturally *p*-type semiconductor with high air stability and room-temperature carrier mobilities, Te is well-suited for constructing high-performance *p*-FETs and CMOS circuits when paired with *n*-type semiconductors like MoS_2 . These could serve as the foundational building blocks for future integrated circuits. Additionally, the thickness-dependent bandgap of Te covers the SWIR to MWIR range, making it highly promising for designing and fabricating high-performance IR photodetectors. These photodetectors have potential applications in various fields, including optical communication, night vision, and medical imaging. Given these exceptional properties, we present this comprehensive Review themed on Te and its applications in advanced electronics and optoelectronics, hoping to inspire readers to explore and develop this novel material to shape the future of electronics and optoelectronics together with us. This Review begins with a detailed introduction to the basic crystal structures of Te, which are fundamental to many of its intriguing properties. Following this, we explore the band structure of Te and its intrinsic properties, including carrier mobilities, optical, piezoelectric, thermoelectric, and ferroelectric properties. These properties form the foundation for its diverse device applications. The Review then covers mainstream synthesis methods for producing high-quality Te nanostructures. These methods range from solution-phase-based techniques, such as hydrothermal and ultrasonic exfoliation (primarily for Te nanoflakes), to vapor-phase methods like CVD/PVD in tubular furnaces (mainly for Te nanobelts, nanorods, and nanomeshes), and other PVD techniques including thermal evaporation, magnetron sputtering, and MBE for Te thin films. Each synthesis route yields Te nanostructures with different morphologies, enabling various novel device designs. We then provide a comprehensive summary of the latest research on device applications involving Te nanostructures. The papers reviewed are categorized by application area, covering electronics (such as FETs, TPCTs, memory devices, nanogenerators, RF diodes, and electrical switches), optoelectronics (including photodetectors, in-sensor computing devices, and photovoltaic cells), sensors (encompassing chemical/physical and gas sensors), and large-scale circuits. Finally, we share our insights into potential future research directions for Te.

Although a wide range of device applications based on Te have been demonstrated, there is still a need for significant efforts to address the remaining challenges in this research field. 1) Thermal instability. While Te exhibits high air stability at room temperature, Te devices often suffer from severe performance degradation and even failure at temperatures above 200 °C. This issue is believed to stem from the sublimation of the Te channel due to its high vapor pressure and contact degradation caused by interdiffusion between Te and metal electrodes.^[185] Thermal instability presents a significant challenge for practical applications of Te in FETs and IR photodetectors, considering that FETs rely on high device repeatability and IR photodetector must manage the strong thermal effects of IR light, respectively. 2) Low on/off current ratios. Although the narrow bandgap of Te ensures high photoresponsivity in IR region, it also results in low on/off current ratios, which limits its performance as a channel material in electronics, particularly in basic FETs. Additionally, the high

thermally excited current density at room temperature leads to a high dark current in Te-based IR photodetectors, resulting in low specific detectivity. While decreasing the thickness of Te can increase the bandgap and thus improve the on/off current ratios, this comes at the cost of reduced hole mobility and consequently lower on-state current. 3) Preparation of single-crystalline Te thin films on a large scale. As introduced in this Review, methods such as thermal evaporation, magnetron sputtering, and MBE have been developed to synthesize wafer-scale Te thin films, but these samples remain polycrystalline. The abundance of grain boundaries increases the probability of carrier scattering, reducing carrier mobility and causing additional heat dissipation. The polycrystalline nature of Te thin films also affects device performance uniformity in large-scale production. Currently, the statistic performance of wafer-scale Te device arrays made from these Te thin films is significantly inferior to that of their *n*-type counterparts made from wafer-scale, high-quality MoS₂ thin films.^[189,297]

Given that the application of Te in advanced devices is still in its infancy but holds significant potential for shaping future electronics and optoelectronics, several research directions in device design and material growth could be pursued to advance this field in the near future. 1) Developing strategies to improve the thermal stability of Te device. To address the thermal instability of Te devices caused by channel sublimation due to its high vapor pressure, proper encapsulation layers can be deposited onto Te to mitigate its sublimation. However, unlike conventional Si technology, the absence of dangling bonds on the surfaces of vdW materials makes it challenging to deposit high-quality traditional insulating metal oxides (e.g., Al₂O₃, HfO₂, and ZrO₂) via ALD as encapsulation layers for Te. Additionally, high-temperature annealing should be avoided after deposition. Novel high- κ dielectric, such as perovskite membranes and vdW dielectrics, could offer promising solutions.^[298,299] As for the contact issue, metallic vdW materials like graphene could be used as electrodes instead of conventional metal to prevent interdiffusion at the contacts. 2) Designing new device architectures to squeeze out the performance limit of Te FET. The narrow bandgap of Te provides high carrier density but results in low on/off current ratios at room temperature. To enhance gate controllability while maintaining a large on-state current in Te FETs, new transistor architectures, such as GAA structure, could be explored to achieve high-performance Te FETs with both large on/off current ratios and high on-state current.^[198–200] Moreover, the current shortest channel length of Te FETs remains in the hundreds of nanometers; developing ultrashort-channel Te FETs in the future could push the technology to its quantum limit. These explorations could help fairly assess the application potential of Te and promote its stable development. 3) Synthesizing single-crystalline Te thin films on a wafer scale. Single-crystalline vdW semiconductor thin films offer superior device performance and uniformity, but its synthesis remains a significant challenge. To grow high-quality Te thin films, different material growth strategies, such as substrate engineering, should be explored. Using substrate with atomically flat surface could promote the uniform nucleation of target thin films.^[300–303] Additionally, growth parameters should be carefully tuned to control the thickness of Te thin films and achieve the desired bandgap. Theoretical calculations should be conducted concurrently to uncover the growth physics and optimize the material growth process. 4) Designing and fabricat-

ing Te-based in-sensor/in-memory computing systems for the IR region. The superior IR response of Te makes it a strong candidate for in-sensor computing systems operating in the long-wavelength region, complementing systems that operate in the visible range. Our group has previously reported the fabrication of vdW heterostructure enabled by Te for in-sensor computing systems in the optical communication band, though this work remains at the single-device level.^[124] In the future, with the successful growth of high-quality Te thin films, hardware/software codesign for Te-based in-sensor computing architectures is likely to become a prominent research spot. Additionally, given the demonstration of high-performance electrical switches enabled by Te,^[107] developing high-performance in-memory computing systems could also be a promising research direction. 5) Exploiting its intrinsic chirality to develop chiral devices based on Te. Chirality is another intriguing property of Te, but chiral devices based on Te have been rarely explored. For instance, CPL detection is crucial in many fields and conventional CPL detection systems rely on redundant optical components.^[304–307] Te nanostructures with different chirality hold great promise for enabling a highly compact CPL detection system. It is important to note that the helical Te chains align along the *c*-axis, which is often perpendicular to the substrate surface during growth. Therefore, designing an effective CPL light-matter coupling strategy is a critical technical challenge that requires more thinking.

Acknowledgements

J.Z. and D.D. contributed equally to this work. C.T. thanks the funding support from the National Natural Science Foundation of China – Excellent Young Scientists Fund (Hong Kong and Macau) (52122002), ECS Scheme (21201821), and General Research Fund (11200122) from the Research Grant Council of Hong Kong. Y.C. Thanks the funding support from the General Research Fund (15301322) from the Research Grant Council of Hong Kong. C.Z. declares this as a non-Huawei service achievement.

Conflict of Interest

The authors declare no conflict of interest.

Keywords

electronics, optoelectronics, synthesis methods, tellurium, van der Waals materials

Received: June 23, 2024

Revised: August 28, 2024

Published online: September 16, 2024

- [1] M. E. Weeks, *J. Chem. Educ.* **1932**, 9, 474.
- [2] M. E. Weeks, *J. Chem. Educ.* **1935**, 12, 403.
- [3] H. E. Suess, H. C. Urey, *Rev. Mod. Phys.* **1956**, 28, 53.
- [4] A. V. Hippel, *J. Chem. Phys.* **1948**, 16, 372.
- [5] Z. Zhu, X. Cai, S. Yi, J. Chen, Y. Dai, C. Niu, Z. Guo, M. Xie, F. Liu, J. H. Cho, Y. Jia, Z. Zhang, *Phys. Rev. Lett.* **2017**, 119, 106101.
- [6] S. Khatun, A. Banerjee, A. J. Pal, *Nanoscale* **2019**, 11, 3591.
- [7] J. Chen, Y. Dai, Y. Ma, X. Dai, W. Ho, M. Xie, *Nanoscale* **2017**, 9, 15945.

- [8] J. Zhou, G. Zhang, W. Wang, Q. Chen, W. Zhao, H. Liu, B. Zhao, Z. Ni, J. Lu, *Nat. Commun.* **2024**, *15*, 1435.
- [9] C. Yan, C. Wang, L. Zhou, P. Guo, K. Liu, Z. Y. Lu, Z. Cheng, Y. Chai, A. Pan, W. Ji, *Chin. Phys. B* **2020**, *29*, 097103.
- [10] C. Wang, X. Zhou, J. Qiao, L. Zhou, X. Kong, Y. Pan, Z. Cheng, Y. Chai, W. Ji, *Nanoscale* **2018**, *10*, 22263.
- [11] A. K. Geim, I. V. Grigorieva, *Nature* **2013**, *499*, 419.
- [12] C. Tan, X. Cao, X. J. Wu, Q. He, J. Yang, X. Zhang, J. Chen, W. Zhao, S. Han, G. H. Nam, M. Sindoro, H. Zhang, *Chem. Rev.* **2017**, *117*, 6225.
- [13] Y. Liu, N. O. Weiss, X. Duan, H. C. Cheng, Y. Huang, X. Duan, *Nat. Rev. Mater.* **2016**, *1*, 16042.
- [14] K. S. Novoselov, A. Mishchenko, A. Carvalho, A. H. Castro Neto, *Science* **2016**, *353*, aac9439.
- [15] Y. Cao, V. Fatemi, S. Fang, K. Watanabe, T. Taniguchi, E. Kaxiras, P. Jarillo-Herrero, *Nature* **2018**, *556*, 43.
- [16] Y. Cao, V. Fatemi, A. Demir, S. Fang, S. L. Tomarken, J. Y. Luo, J. D. Sanchez-Yamagishi, K. Watanabe, T. Taniguchi, E. Kaxiras, R. C. Ashoori, P. Jarillo-Herrero, *Nature* **2018**, *556*, 80.
- [17] C. Xu, J. Zeng, Y. Wang, X. Jiang, X. Wang, *SmartMat* **2023**, *4*, e1109.
- [18] Z. Zan, X. Li, X. Gao, J. Huang, Y. Luo, L. Han, *Acta Phys.-Chim. Sin* **2023**, *39*, 2209016.
- [19] S. B. Desai, S. R. Madhupathy, A. B. Sachid, J. P. Llinas, Q. Wang, G. H. Ahn, G. Pitner, M. J. Kim, J. Bokor, C. Hu, H. S. P. Wong, A. Javey, *Science* **2016**, *354*, 99.
- [20] M. Y. Li, S. K. Su, H. S. P. Wong, L. J. Li, *Nature* **2019**, *567*, 170.
- [21] F. Wu, H. Tian, Y. Shen, Z. Hou, J. Ren, G. Gou, Y. Sun, Y. Yang, T. L. Ren, *Nature* **2022**, *603*, 259.
- [22] G. Fiori, F. Bonaccorso, G. Iannaccone, T. Palacios, D. Neumaier, A. Seabaugh, S. K. Banerjee, L. Colombo, *Nat. Nanotechnol.* **2014**, *9*, 768.
- [23] Y. Liu, X. Duan, H. J. Shin, S. Park, Y. Huang, X. Duan, *Nature* **2021**, *591*, 43.
- [24] X. Hou, T. Jin, Y. Zheng, W. Chen, *SmartMat* **2024**, *5*, e1236.
- [25] S. Manzeli, D. Ovchinnikov, D. Pasquier, O. V. Yazyev, A. Kis, *Nat. Rev. Mater.* **2017**, *2*, 17033.
- [26] Q. H. Wang, K. Kalantar-Zadeh, A. Kis, J. N. Coleman, M. S. Strano, *Nat. Nanotechnol.* **2012**, *7*, 699.
- [27] M. Chhowalla, H. S. Shin, G. Eda, L. J. Li, K. P. Loh, H. Zhang, *Nat. Chem.* **2013**, *5*, 263.
- [28] X. Kong, C. Fu, V. Gladikh, F. Ding, *SmartMat* **2023**, *4*, e1152.
- [29] L. Li, Y. Yu, G. J. Ye, Q. Ge, X. Ou, H. Wu, D. Feng, X. Chen, Y. Zhang, *Nat. Nanotechnol.* **2014**, *9*, 372.
- [30] J. R. Reitz, *Phys. Rev.* **1957**, *105*, 1233.
- [31] A. Nussbaum, *Phys. Rev.* **1954**, *94*, 337.
- [32] H. B. Callen, *J. Chem. Phys.* **1954**, *22*, 518.
- [33] P. Bhaskar, A. W. Achtstein, M. J. W. Vermeulen, L. D. A. Siebbeles, *J. Phys. Chem. C* **2019**, *123*, 841.
- [34] Y. Liu, Y. W. W. u., W. A. Goddard III, *J. Am. Chem. Soc.* **2018**, *140*, 550.
- [35] F. Liang, H. Qian, *Mater. Chem. Phys.* **2009**, *113*, 523.
- [36] S. Berweger, G. Qiu, Y. Wang, B. Pollard, K. L. Genter, R. Tyrrell-Ead, T. M. Wallis, W. Wu, P. D. Ye, P. Kabos, *Nano Lett.* **2019**, *19*, 1289.
- [37] L. Rothkirch, R. Link, W. Sauer, F. Manglus, *Phys. Stat. Sol. (b)* **1969**, *31*, 147.
- [38] A. S. Epstein, H. Fritzsche, K. Lark-Horovitz, *Phys. Rev.* **1957**, *107*, 412.
- [39] A. Coker, T. Lee, T. P. Das, *Phys. Rev. B* **1980**, *22*, 2968.
- [40] R. W. Dutton, R. S. Muller, *Proc. IEEE* **1971**, *59*, 1511.
- [41] Y. Sun, T. Gotoh, B. Li, H. Li, M. Zhu, *Phys. Status Solidi RRL* **2024**, *2300414*.
- [42] V. B. Anzin, M. I. Eremets, Y. V. Kosichkin, A. I. Nadezhdinskii, A. M. Shirokov, *Phys. Stat. Sol. (a)* **1977**, *42*, 385.
- [43] J. Peng, Y. Pan, Z. Yu, J. Wu, J. Wu, Y. Zhou, Y. Guo, X. Wu, C. Wu, Y. Xie, *Angew. Chem., Int. Ed.* **2018**, *57*, 13533.
- [44] J. W. Liu, J. H. Zhu, C. L. Zhang, H. W. Liang, S. H. Yu, *J. Am. Chem. Soc.* **2010**, *132*, 8945.
- [45] D. A. Nguyen, S. Cho, S. Park, D. Y. Park, H. C. Suh, M. S. Jeong, T. P. A. Bach, H. Kim, H. Im, *Nano Energy* **2023**, *113*, 108552.
- [46] J. J. Loferski, *Phys. Rev.* **1954**, *93*, 707.
- [47] Y. Wang, S. Jin, Q. Wang, M. Wu, S. Yao, P. Liao, M. J. Kim, G. J. Cheng, W. Wu, *Nano-Micro Lett.* **2020**, *12*, 160.
- [48] A. Zhao, L. Zhang, Y. Pang, C. Ye, *Appl. Phys. A* **2005**, *80*, 1725.
- [49] C. S. Lin, W. D. Cheng, G. L. Chai, H. Zhang, *Phys. Chem. Chem. Phys.* **2018**, *20*, 24250.
- [50] S. Q. Lin, Z. Chen, J. Shen, B. Ge, Y. Pei, *Nat. Commun.* **2016**, *7*, 10287.
- [51] C. Dun, C. A. Hewitt, H. Huang, D. S. Montgomery, J. Xu, D. L. Carroll, *Phys. Chem. Chem. Phys.* **2015**, *17*, 8591.
- [52] S. Sharma, N. Singh, U. Schwingenschlogl, *ACS Appl. Energy Mater.* **2018**, *1*, 1950.
- [53] D. K. Sang, T. Ding, M. N. Wu, Y. Li, J. Li, F. Liu, Z. Guo, H. Zhang, H. Xie, *Nanoscale* **2019**, *11*, 18116.
- [54] H. Peng, N. Kioussis, G. J. Snyder, *Phys. Rev. B* **2014**, *89*, 195206.
- [55] G. Qiu, S. Huang, M. Segovia, P. K. Venuthurumilli, Y. Wang, W. Wu, X. Xu, P. D. Ye, *Nano Lett.* **2019**, *19*, 1955.
- [56] S. Kong, Z. Huang, Y. Hu, Y. Jiang, Y. Lu, W. Zhao, Q. Shi, M. Yuan, B. Dai, J. Li, W. Yang, Y. Xie, *Nano Energy* **2023**, *115*, 108708.
- [57] H. Xu, Y. Guo, B. Wu, C. Hou, Q. Zhang, Y. Li, H. Wang, *ACS Appl. Mater. Interfaces* **2020**, *12*, 33297.
- [58] C. Li, F. Jiang, C. Liu, W. Wang, X. Li, T. Wang, J. Xu, *Chem. Eng. J* **2017**, *320*, 201.
- [59] Y. Liu, X. Lan, J. Xu, W. Zhou, C. Liu, C. Liu, P. Liu, M. Li, F. Jiang, *ACS Appl. Mater. Interfaces* **2021**, *13*, 43155.
- [60] J. D. Zook, *Phys. Rev.* **1964**, *136*, A869.
- [61] D. Royer, E. Dieulesaint, *J. Appl. Phys.* **2008**, *50*, 4042.
- [62] Y. Wang, R. Wang, S. Wan, Q. Wang, M. J. Kim, D. Ding, W. Wu, *Nano Futures* **2019**, *3*, 011001.
- [63] M. Wu, Y. Wang, S. Gao, R. Wang, C. Ma, Z. Tang, N. Bao, W. Wu, F. Fan, W. Wu, *Nano Energy* **2019**, *56*, 693.
- [64] S. Dang, S. D. Kang, T. Dai, X. Y. Ma, H. W. Li, W. Q. Zhou, G. L. Wang, P. Hu, Y. Sun, Z. H. He, F. M. Yu, X. Zhou, S. X. Wu, S. W. Li, *Nanotechnology* **2020**, *31*, 095502.
- [65] M. Hirayama, R. Okugawa, S. Ishibashi, S. Murakami, T. Miyake, *Phys. Rev. Lett.* **2015**, *114*, 206401.
- [66] G. Qiu, C. Niu, Y. Wang, M. Si, Z. Zhang, W. Wu, P. D. Ye, *Nat. Nanotechnol.* **2020**, *15*, 585.
- [67] G. Jnawali, Y. Xiang, S. M. Linser, I. A. Shaojaei, R. Wang, G. Qiu, C. Lian, B. M. Wong, W. Wu, P. D. Ye, Y. Leng, H. E. Jackson, L. M. Smith, *Nat. Commun.* **2020**, *11*, 3991.
- [68] C. Niu, G. Qiu, Y. Wang, Z. Zhang, M. Si, W. Wu, P. D. Ye, *Phys. Rev. B* **2020**, *101*, 205414.
- [69] G. Qiu, Y. Wang, Y. Nie, Y. Zheng, K. Cho, W. Wu, P. D. Ye, *Nano Lett.* **2018**, *18*, 5760.
- [70] J. Ma, B. Cheng, L. Li, Z. Fan, H. Mu, J. Lai, X. Song, D. Yang, J. Cheng, Z. Wang, C. Zeng, D. Sun, *Nat. Commun.* **2022**, *13*, 5425.
- [71] C. Niu, G. Qiu, Y. Wang, P. Tan, M. Wang, J. Jian, H. Wang, W. Wu, P. D. Ye, *Nano Lett.* **2023**, *23*, 8445.
- [72] C. Niu, S. Huang, N. Ghosh, P. Tan, M. Wang, W. Wu, X. Xu, P. D. Ye, *Nano Lett.* **2023**, *23*, 3599.
- [73] F. Calavalle, M. Suárez-Rodríguez, B. Martín-García, A. Johansson, D. C. Vaz, H. Yang, I. V. Maznichenko, S. Ostanin, A. Mateo-Alonso, A. Chuvilín, I. Mertig, M. Gobbi, F. Casanova, L. E. Hueso, *Nat. Mater.* **2022**, *21*, 526.
- [74] A. Ben-Moshe, A. Silva, A. Müller, A. Abu-Odeh, P. Harrison, J. Waelder, F. Niroui, C. Ophus, A. M. Minor, M. Asta, W. Theis, P. Ercius, A. P. Alivisatos, *Science* **2021**, *372*, 729.

- [75] L. A. Agapito, N. Kiousis, W. A. Goddard, N. P. Ong, *Phys. Rev. Lett.* **2013**, *110*, 176401.
- [76] Y. Wang, G. Qiu, R. Wang, S. Huang, Q. Wang, Y. Liu, Y. Du, W. A. Goddard III, M. J. Kim, X. Xu, P. D. Ye, W. Wu, *Nat. Electron.* **2018**, *1*, 228.
- [77] M. Amani, C. Tan, G. Zhang, C. Zhao, J. Bullock, X. Song, H. Kim, V. R. Shrestha, Y. Gao, K. B. Crozier, M. Scott, A. Javey, *ACS Nano* **2018**, *12*, 7253.
- [78] J. Qi, Y. Dai, C. Ma, C. Ke, W. Wang, Z. Wu, X. Wang, K. Bao, Y. Xu, H. Huang, L. Wang, J. Wu, G. Luo, Y. Chen, Z. Lin, Q. He, *Adv. Mater.* **2024**, *36*, 2306962.
- [79] Z. Xie, C. Xing, W. Huang, T. Fan, Z. Li, J. Zhao, Y. Xiang, Z. Guo, J. Li, Z. Yang, B. Dong, J. Qu, D. Fan, H. Zhang, *Adv. Funct. Mater.* **2018**, *28*, 1705833.
- [80] P. Yang, J. Zha, G. Gao, L. Zheng, H. Huang, Y. Xia, S. Xu, T. Xiong, Z. Zhang, Z. Yang, Y. Chen, D. K. Ki, J. J. Liou, W. Liao, C. Tan, *Nano-Micro Lett.* **2022**, *14*, 109.
- [81] J. You, Z. Jin, Y. Li, T. Kang, K. Zhang, W. Wang, M. Xu, Z. Gao, J. Wang, J. K. Kim, Z. Luo, *Adv. Funct. Mater.* **2024**, *34*, 2311134.
- [82] C. Zhao, H. Batiz, B. Yasar, W. Ji, M. C. Scott, D. C. Chrzan, A. Javey, *Adv. Mater. Interfaces* **2022**, *9*, 2101540.
- [83] X. Wei, S. Wang, N. Zhang, Y. Li, Y. Tang, H. Jing, J. Lu, Z. Xu, H. Xu, *Adv. Funct. Mater.* **2023**, *33*, 2300141.
- [84] X. Zhang, J. Jiang, A. Aji, Suleiman, B. J., X. Hu, X. Zhou, T. Zhai, *Adv. Funct. Mater.* **2019**, *29*, 1906585.
- [85] Y. Meng, X. Li, X. Kang, W. Li, W. Wang, Z. Lai, W. Wang, Q. Quan, X. Bu, S. Yip, P. Xie, D. Chen, D. Li, F. Wang, C. F. Yeung, C. Lan, C. Liu, L. Shen, Y. Lu, F. Chen, C. Y. Wong, J. C. Ho, *Nat. Commun.* **2023**, *14*, 2431.
- [86] S. Yang, B. Chen, Y. Qin, Y. Zhou, L. Liu, M. Durso, H. Zhuang, Y. Shen, S. Tongay, *Phys. Rev. Mater.* **2018**, *2*, 104002.
- [87] M. Peng, R. Xie, Z. Wang, P. Wang, F. Wang, H. Ge, Y. Wang, F. Zhong, P. Wu, J. Ye, Q. Li, L. Zhang, X. Ge, Y. Ye, Y. Lei, W. Jiang, Z. Hu, F. Wu, X. Zhou, J. Miao, J. Wang, H. Yan, C. Shan, J. Dai, C. Chen, X. Chen, W. Lu, W. Hu, *Sci. Adv.* **2021**, *7*, eabf7358.
- [88] C. Wang, C. Xu, X. Guo, N. Zhang, J. Yan, J. Chen, W. Yu, J. K. Qin, Y. Zhu, L. J. Li, Y. Chai, *Nano Res.* **2022**, *15*, 5712.
- [89] C. Zhao, C. Tan, D. H. Lien, X. Song, M. Amani, M. Hettick, H. Y. Y. Nyein, Z. Yuan, L. Li, M. C. Scott, A. Javey, *Nat. Nanotechnol.* **2020**, *15*, 53.
- [90] C. Zhao, H. Batiz, B. Yasar, H. Kim, W. Ji, M. C. Scott, D. C. Chrzan, A. Javey, *Adv. Mater.* **2021**, *33*, 2100860.
- [91] Y. Ran, Y. Song, X. Jia, P. Gu, Z. Cheng, Y. Zhu, Q. Wang, Y. Pan, Y. Li, Y. Gao, Y. Ye, *Small* **2024**, *20*, 2309953.
- [92] X. Huang, J. Guan, Z. Lin, B. Liu, S. Xing, W. Wang, J. Guo, *Nano Lett.* **2017**, *17*, 4619.
- [93] G. Zhou, R. Addou, Q. Wang, S. Honari, C. R. Cormier, L. Cheng, R. Yue, C. M. Smyth, A. Laturia, J. Kim, W. G. Vandenberghe, M. J. Kim, R. M. Wallace, C. L. Hinkle, *Adv. Mater.* **2018**, *30*, 1803109.
- [94] B. Zheng, Z. Wu, F. Guo, R. Ding, J. Mao, M. Xie, S. P. Lau, J. Hao, *Adv. Optical Mater.* **2021**, *9*, 2101052.
- [95] T. Kim, C. H. Choi, P. Byeon, M. Lee, A. Song, K. B. Chung, S. Han, S. Y. Chung, K. S. Park, J. K. Jeong, *npj 2D Mater. Appl.* **2022**, *6*, 4.
- [96] S. H. Lim, T. I. Kim, I. J. Park, H. I. Kwon, *ACS Appl. Electron. Mater.* **2023**, *5*, 4816.
- [97] G. Qiu, M. Si, Y. Wang, X. Lyu, W. Wu, P. D. Ye, presented at 76th Device Research Conference (DRC), Santa Barbara, CA, USA, June **2018**.
- [98] X. Zhang, H. Yu, W. Tang, X. Wei, L. Gao, M. Hong, Q. Liao, Z. Kang, Z. Zhang, Y. Zhang, *Adv. Mater.* **2022**, *34*, 2109521.
- [99] Z. Lin, J. Wang, J. Chen, C. Wang, J. Liu, W. Zhang, Y. Chai, *Adv. Electron. Mater.* **2022**, *8*, 2200380.
- [100] F. Qin, Y. Hu, P. Hu, W. Feng, *Nanotechnology* **2019**, *31*, 115204.
- [101] W. Jiang, X. Wang, Y. Chen, S. Wu, B. Wu, X. Yang, T. Lin, H. Shen, X. Meng, X. Wu, J. Chu, J. Wang, *ACS Appl. Mater. Interfaces* **2021**, *13*, 6.
- [102] J. Chen, T. Zhang, J. Wang, L. Xu, Z. Lin, J. Liu, C. Wang, N. Zhang, S. P. Lau, W. Zhang, M. Chhowalla, Y. Chai, *Sci. Adv.* **2022**, *8*, eabn3837.
- [103] J. Chen, Y. Zhou, J. Yan, J. Liu, L. Xu, J. Wang, T. Wan, Y. He, W. Zhang, Y. Chai, *Nat. Commun.* **2022**, *13*, 7758.
- [104] T. Lee II, S. Lee, E. Lee, S. Sohn, Y. Lee, S. Lee, G. Moon, D. Kim, Y. S. Kim, J. M. Myoung, Z. L. Wang, *Adv. Mater.* **2013**, *25*, 2920.
- [105] W. He, H. V. Ngoc, Y. T. Qian, J. S. Hwang, Y. P. Yan, H. Choi, D. J. Kang, *Appl. Surf. Sci.* **2017**, *392*, 1055.
- [106] G. Rao, H. Fang, T. Zhou, C. Zhao, N. Shang, J. Huang, Y. Liu, X. Du, P. Li, X. Jian, L. Ma, J. Wang, K. Liu, J. Wu, X. Wang, J. Xiong, *Adv. Mater.* **2022**, *34*, 2204697.
- [107] J. Shen, S. Jia, N. Shi, Q. Ge, T. Gotoh, S. Lv, Q. Liu, R. Dronskowski, S. R. Elliott, Z. Song, M. Zhu, *Science* **2021**, *374*, 1390.
- [108] Y. Yang, M. Xu, S. Jia, B. Wang, L. Xu, X. Wang, H. Liu, Y. Liu, Y. Guo, L. Wang, S. Duan, K. Liu, M. Zhu, J. Pei, W. Duan, D. Liu, H. Li, *Nat. Commun.* **2021**, *12*, 6081.
- [109] A. M. Askar, P. Palacios, F. Pasadas, M. Saeed, M. R. Mohammadzadeh, R. Negra, M. M. Adachi, *npj 2D Mater. Appl.* **2023**, *7*, 70.
- [110] C. Niu, M. Wang, Z. Zhang, G. Qiu, Y. Wang, D. Zheng, P. Y. Liao, W. Wu, P. D. Ye, *ACS Nano* **2024**, *18*, 15107.
- [111] L. Li, G. Zhang, M. Younis, Y. Luo, L. Yang, W. Jin, H. Wu, B. Xiao, W. Zhang, H. Chang, *ACS Appl. Electron. Mater.* **2024**, *6*, 2161.
- [112] M. Dai, C. Wang, B. Qiang, Y. Jin, M. Ye, F. Wang, F. Sun, X. Zhang, Y. Luo, Q. J. Wang, *Nat. Commun.* **2023**, *14*, 3421.
- [113] J. Yao, F. Chen, J. Li, J. Du, D. Wu, Y. Tian, C. Zhang, J. Yang, X. Li, P. Lin, *J. Mater. Chem. C* **2021**, *9*, 13123.
- [114] J. J. Tao, J. Jiang, S. N. Zhao, Y. Zhang, X. X. Li, X. Fang, P. Wang, W. Hu, Y. H. Lee, H. L. Lu, D. W. Zhang, *ACS Nano* **2021**, *15*, 3241.
- [115] H. Wang, H. Huang, J. Zha, Y. Xia, P. Yang, Y. Zeng, Y. Liu, R. Cao, B. Wang, W. Wang, L. Zheng, Y. Chen, Q. He, X. Chen, K. Jiang, J. H. Lin, Z. Shi, J. C. Ho, H. Zhang, C. Tan, *Adv. Optical Mater.* **2023**, *11*, 2301508.
- [116] J. Zha, Y. Xia, S. Shi, H. Huang, S. Li, C. Qian, H. Wang, P. Yang, Z. Zhang, Y. Meng, W. Wang, Z. Yang, H. Yu, J. C. Ho, Z. Wang, C. Tan, *Adv. Mater.* **2024**, *36*, 2308502.
- [117] T. P. A. Bach, S. Cho, H. Kim, D. A. Nguyen, H. Im, *ACS Nano* **2024**, *18*, 4131.
- [118] C. F. Shen, Y. Liu, J. Wu, C. Xu, D. Cui, Z. Li, Q. Liu, Y. Li, Y. Wang, X. Cao, H. Kumazoe, F. Shimojo, A. Krishnamoorthy, R. K. Kalia, A. Nakano, P. D. Vashishta, M. R. Amer, A. N. Abbas, H. Wang, W. Wu, C. Zhou, *ACS Nano* **2020**, *14*, 303.
- [119] D. Pokhrel, E. Bastola, A. B. Phillips, M. J. Heben, R. J. Ellingson, *Mater. Adv.* **2020**, *1*, 2721.
- [120] K. Wu, H. Ma, Y. Gao, W. Hu, J. Yang, *J. Mater. Chem. A* **2019**, *7*, 7430.
- [121] A. Kolay, D. Maity, P. Ghosal, M. Deepa, *ACS Appl. Mater. Interfaces* **2019**, *11*, 47972.
- [122] M. Mousavi-Kamazani, R. Rahmatollahzadeh, S. Amin Shobeiri, F. Beshkar, *Ultrason. Sonochem.* **2017**, *39*, 233.
- [123] T. Yan, Y. Cai, Y. Wang, J. Yang, S. Li, X. Zhan, F. Wang, R. Cheng, F. Wang, J. He, Z. Wang, *Sci. China Inf. Sci.* **2023**, *66*, 160404.
- [124] J. Zha, S. Shi, A. Chaturvedi, H. Huang, P. Yang, Y. Yao, S. Li, Y. Xia, Z. Zhang, W. Wang, H. Wang, S. Wang, Z. Yuan, Z. Yang, Q. He, H. Tai, E. H. Tong Teo, H. Yu, J. C. Ho, Z. Wang, H. Zhang, C. Tan, *Adv. Mater.* **2023**, *35*, 2211598.
- [125] T. Y. Wei, H. Y. Chang, C. C. Huang, *RSC Adv.* **2013**, *3*, 13983.
- [126] A. Bobrowski, A. Króllicka, J. Śliwa, J. Zarębski, *Electrochim. Acta* **2017**, *252*, 453.

- [127] M. Manikandan, S. Dhanuskodi, N. Maheswari, G. Muralidharan, C. Revathi, R. T. Rajendra Kumar, G. Mohan Rao, *Sens. Bio-Sens. Res.* **2017**, *13*, 40.
- [128] T. Liang, J. W. Zha, D. R. Wang, Z. M. Dang, *J. Phys. D: Appl. Phys.* **2014**, *47*, 505103.
- [129] V. Selamneni, T. Akshaya, V. Adepu, P. Sahatiya, *Nanotechnology* **2021**, *32*, 455201.
- [130] A. Nocke, S. Richter, M. Wolf, G. Gerlach, *Procedia Chem* **2009**, *1*, 1151.
- [131] J. Kou, Y. Zhang, Y. Liu, K. Zhang, W. Liu, J. Zhai, *Semicond. Sci. Technol.* **2017**, *32*, 074001.
- [132] D. Wang, A. Yang, T. Lan, C. Fan, J. Pan, Z. Liu, J. Chu, H. Yuan, X. Wang, M. Rong, N. Koratkar, *J. Mater. Chem. A* **2019**, *7*, 26326.
- [133] H. Cui, K. Zheng, Z. Xie, J. Yu, X. Zhu, H. Ren, Z. Wang, F. Zhang, X. Li, L. Q. Tao, H. Zhang, X. Chen, *ACS Appl. Mater. Interfaces* **2020**, *12*, 47704.
- [134] D. Wang, J. Pan, T. Lan, J. Chu, C. Fan, H. Yuan, Y. Wu, A. Yang, X. Wang, M. Rong, *ACS Appl. Nano Mater* **2020**, *3*, 7587.
- [135] J. Kou, A. Yu, Y. Liu, M. Jia, J. Guo, R. Wen, Y. Lei, Y. Zhu, Y. Zhang, J. Zhai, *Semicond. Sci. Technol.* **2019**, *34*, 075011.
- [136] G. H. Kim, S. H. Kang, J. M. Lee, M. Son, J. Lee, H. Lee, I. Chung, J. Kim, Y. H. Kim, K. Ahn, S. K. Park, M. G. Kim, *Appl. Surf. Sci.* **2023**, *636*, 157801.
- [137] L. Li, H. Xu, Z. Li, L. Liu, Z. Lou, L. Wang, *Small* **2023**, *19*, 2303114.
- [138] S. Deckoff-Jones, Y. Wang, H. Lin, W. Wu, J. Hu, *ACS Photonics* **2019**, *6*, 1632.
- [139] Y. Du, G. Qiu, Y. Wang, M. Si, X. Xu, W. Wu, P. D. Ye, *Nano Lett.* **2017**, *17*, 3965.
- [140] J. Qiao, Y. Pan, F. Yang, C. Wang, Y. Chai, W. Ji, *Sci. Bull.* **2018**, *63*, 159.
- [141] B. Wu, X. Liu, J. Yin, H. Lee, *Mater. Res. Express* **2017**, *4*, 095902.
- [142] Y. Xiang, S. Gao, R. G. Xu, W. Wu, Y. Leng, *Nano Energy* **2019**, *58*, 202.
- [143] W. Zhang, Q. Wu, O. V. Yazyev, H. Weng, Z. Guo, W. D. Cheng, G. L. Chai, *Phys. Rev. B* **2018**, *98*, 115411.
- [144] L. Xian, A. P. Paz, E. Bianco, P. M. Ajayan, A. Rubio, *2D Mater.* **2017**, *4*, 041003.
- [145] S. Yi, Z. Zhu, X. Cai, Y. Jia, J. H. Cho, *Inorg. Chem.* **2018**, *57*, 5083.
- [146] H. H. Choi, K. Cho, C. D. Frisbie, H. Sirringhaus, V. Podzorov, *Nat. Mater.* **2018**, *17*, 2.
- [147] J. R. Hook, H. E. Hall, *Solid state physics*, John Wiley & Sons, xx **2013**.
- [148] X. Ren, Y. Wang, Z. Xie, F. Xue, C. Leighton, C. D. Frisbie, *Nano Lett.* **2019**, *19*, 4738.
- [149] E. Bianco, R. Rao, M. Snure, T. Back, N. R. Glavin, M. E. McConney, P. M. Ajayan, E. Ringe, *Nanoscale* **2020**, *12*, 12613.
- [150] J. Qiao, X. Kong, Z. X. Hu, F. Yang, W. Ji, *Nat. Commun.* **2014**, *5*, 4475.
- [151] L. Tong, X. Huang, P. Wang, L. Ye, M. Peng, L. An, Q. Sun, Y. Zhang, G. Yang, Z. Li, F. Zhong, F. Wang, Y. Wang, M. Motlag, W. Wu, G. J. Cheng, W. Hu, *Nat. Commun.* **2020**, *11*, 2308.
- [152] J. Lu, Y. He, C. Ma, Q. Ye, H. Yi, Z. Zheng, J. Yao, G. Yang, *Adv. Mater.* **2023**, *35*, 2211562.
- [153] X. Cai, Y. Ren, M. Wu, D. Xu, X. Luo, *Nanoscale* **2020**, *12*, 167.
- [154] A. Apte, S. Kouser, F. S. Samghabadi, L. Chang, L. M. Sassi, D. Litvinov, B. I. Yakobson, A. B. Puthirath, P. M. Ajayan, *Mater. Today* **2021**, *44*, 40.
- [155] J. He, T. M. Tritt, *Science* **2017**, *357*, eaak9997.
- [156] W. Jones, N. H. March, *Theoretical solid state physics*, Wiley, xx **1973**.
- [157] C. Kittel, P. McEuen, *Introduction to solid state physics*, John Wiley & Sons, xx **2018**.
- [158] Y. Wang, C. Xiao, M. Chen, C. Hua, J. Zou, C. Wu, J. Jiang, S. A. Yan, Y. Lu, W. Ji, *Mater. Horiz.* **2018**, *5*, 521.
- [159] Y. Zhao, S. Zhao, X. Pang, A. Zhang, C. Li, Y. Lin, X. Du, L. Cui, Z. Yang, T. Hao, C. Wang, J. Yin, W. Xie, J. Zhu, *Sci. Adv.* **2024**, *10*, eadm9322.
- [160] A. Guermoune, T. Chari, F. Popescu, S. S. Sabri, J. Guillemette, H. S. Skulason, T. Szkopek, M. Sijaj, *Carbon* **2011**, *49*, 4204.
- [161] X. Li, L. Colombo, R. S. Ruoff, *Adv. Mater.* **2016**, *28*, 6247.
- [162] S. Bhaviripudi, X. Jia, M. S. Dresselhaus, J. Kong, *Nano Lett.* **2010**, *10*, 4128.
- [163] Y. H. Lee, X. Q. Zhang, W. Zhang, M. T. Chang, C. T. Lin, K. D. Cahng, Y. C. Yu, J. T. W. Wang, C. S. Chang, L. J. Li, T. W. Lin, *Adv. Mater.* **2012**, *24*, 2320.
- [164] X. Wang, H. Feng, Y. Wu, L. Jiao, *J. Am. Chem. Soc.* **2013**, *135*, 5304.
- [165] A. Apte, E. Bianco, A. Krishnamoorthy, S. Yazdi, R. Rao, N. Glavin, H. Kumazoe, V. Varshney, A. Roy, F. Shimojo, E. Ringe, R. K. Kalia, A. Nakano, C. S. Tiwary, P. Vashishta, V. Kochat, P. M. Ajayan, *2D Mater.* **2019**, *6*, 015013.
- [166] Q. Wang, M. Safdar, K. Xu, M. Mirza, Z. Wang, J. He, *ACS Nano* **2014**, *8*, 7497.
- [167] K. Okuyama, Y. Kumagai, *J. Appl. Phys.* **1975**, *46*, 1473.
- [168] J. Tao, J. Chai, X. Lu, L. M. Wong, T. I. Wong, J. Pan, Q. Xiong, D. Chi, S. Wang, *Nanoscale* **2015**, *7*, 2497.
- [169] H. Samassekou, A. Alkabsh, M. Wasala, M. Eaton, A. Walber, A. Walker, O. Pitkänen, K. Kordas, S. Talapatra, T. Jayasekera, D. Mazumdar, *2D Mater.* **2017**, *4*, 021002.
- [170] V. Stankus, A. Vasiliauskas, A. Guobienė, M. Andrulevičius, Š. Meškiniš, *Surf. Coat. Technol.* **2022**, *437*, 128361.
- [171] J. M. Garcia, U. Wurstbauer, A. Levy, L. N. Pfeiffer, A. Pinczuk, A. S. Plaut, L. Wang, C. R. Dean, R. Buizza, A. M. V. D. Zande, J. Hone, K. Watanabe, T. Taniguchi, *Solid State Commun.* **2012**, *152*, 975.
- [172] E. Moreau, S. Godey, F. J. Ferrer, D. Vignaud, X. Wallart, J. Avila, M. C. Asensio, F. Bournel, J. J. Gallet, *Appl. Phys. Lett.* **2010**, *97*, 241907.
- [173] H. C. Diaz, R. Chaghi, Y. Ma, M. Batzill, *2D Mater.* **2015**, *2*, 044010.
- [174] P. K. Weimer, *Proc. IEEE* **1964**, *52*, 608.
- [175] J. Yan, H. Pang, L. Xu, J. Yang, R. Quhe, X. Zhang, Y. Pan, B. Shi, S. Liu, L. Xu, J. Yang, F. Pan, Z. Zhang, J. Lu, *Adv. Electron. Mater.* **2019**, *5*, 1900226.
- [176] H. Ying, M. Xu, X. Xu, L. Wen, Z. Liu, X. Wang, X. Zheng, W. Huang, *Device* **2023**, *1*, 100069.
- [177] X. Qin, W. Hu, J. Yang, *Phys. Chem. Chem. Phys.* **2019**, *21*, 23611.
- [178] P. Dasika, D. Samantaray, K. Murali, N. Abraham, K. Watanbe, T. Taniguchi, N. Ravishankar, K. Majumdar, *Adv. Funct. Mater.* **2021**, *31*, 2006278.
- [179] S. Gao, Y. Wang, R. Wang, W. Wu, *Semicond. Sci. Technol.* **2017**, *32*, 104004.
- [180] H. Liu, Y. Du, Y. Deng, P. D. Ye, *Chem. Soc. Rev.* **2015**, *44*, 2732.
- [181] T. Doi, K. Nakao, H. Kamimura, *J. Phys. Soc. Japan* **1970**, *28*, 36.
- [182] *IEEE International Roadmap for Devices and Systems*, <https://irds.ieee.org/editions/2023>.
- [183] R. Honig, D. Kramer, *Pressure Curves of the Elements*, RCA laboratories, xx **1968**.
- [184] L. Brooks, *J. Am. Chem. Soc.* **1952**, *74*, 227.
- [185] C. Zhao, L. Hurtado, A. Javey, *Appl. Phys. Lett.* **2020**, *117*, 192104.
- [186] Z. Zhang, M. Passlack, G. Pitner, S. Natani, S. K. Su, T. A. Chao, S. L. Liew, V. D. H. Hou, C. F. Hsu, W. E. Shipley, N. Safron, G. Doornbos, T. E. Lee, I. Radu, A. C. Kummel, P. Bandaru, H. S. P. Wong, *Nat. Electron.* **2023**, *6*, 999.
- [187] H. Kamata, K. Kita, *Appl. Phys. Lett.* **2017**, *110*, 102106.
- [188] Y. Zhang, M. Choi, Z. Wang, C. Choi, *Appl. Surf. Sci.* **2023**, *609*, 155295.
- [189] W. Li, X. Gong, Z. Yu, L. Ma, W. Sun, S. Gao, Ç. Köroğlu, W. Wang, L. Liu, T. Li, H. Ning, D. Fan, Y. Xu, X. Tu, T. Xu, L. Sun, W. Wang, J. Lu,

- Z. Ni, J. Li, X. Duan, P. Wang, Y. Nie, H. Qiu, Y. Shi, E. Pop, J. Wang, X. Wang, *Nature* **2023**, 613, 274.
- [190] Y. Wang, J. C. Kim, R. J. Wu, J. Martinez, X. Song, J. Yang, F. Zhao, A. Mkhoyan, H. Y. Jeong, M. Chhowalla, *Nature* **2019**, 568, 70.
- [191] P. C. Shen, C. Su, Y. Lin, A. S. Chou, C. C. Cheng, J. H. Park, M. H. Chiu, A. Y. Lu, H. L. Tang, M. M. Tavakoli, G. Pitner, X. Ji, Z. Cai, N. Mao, J. Wang, V. Tung, J. Li, J. Bokor, A. Zettl, C. I. Wu, T. Palacios, L. J. Li, J. Kong, *Nature* **2021**, 593, 211.
- [192] L. Wang, I. Meric, P. Y. Huang, Q. Gao, H. Tran, T. Taniguchi, K. Watanabe, L. M. Campos, D. A. Muller, J. Guo, P. Kim, J. Hone, K. L. Shepard, C. R. Dean, *Science* **2013**, 342, 614.
- [193] Z. Cheng, Y. Yu, S. Singh, K. Price, S. G. Noyce, Y. C. Lin, L. Cao, A. D. Franklin, *Nano Lett.* **2019**, 19, 5077.
- [194] X. Cai, Z. Wu, X. Han, Y. Chen, S. Xu, J. Lin, T. Han, P. He, X. Feng, L. An, R. Shi, J. Wang, Z. Ying, Y. Cai, M. Hua, J. Liu, D. Pan, C. Cheng, N. Wang, *Nat. Commun.* **2022**, 13, 1777.
- [195] T. Y. T. Hung, S. Y. Wang, C. P. Chuu, Y. Y. Chung, A. S. Chou, F. S. Huang, T. Chen, M. Y. Li, C. C. Cheng, J. Cai, C. H. Chien, W. H. Chang, H. S. P. Wong, L. J. Li, presented at 2020 IEEE International Electron Devices Meeting (IEDM), San Francisco, USA, December **2020**.
- [196] Z. Yang, C. Kim, K. Y. Lee, M. Lee, S. Appalakondaiah, C. H. Ra, K. Watanabe, T. Taniguchi, K. Cho, E. Hwang, J. Hone, W. J. Yoo, *Adv. Mater.* **2019**, 31, 1808231.
- [197] K. P. O'Brien, C. H. Naylor, C. Dorow, K. Maxey, A. V. Penumatcha, A. Vyatskikh, T. Zhong, A. Kitamura, S. Lee, C. Rogan, W. Mortelmans, M. S. Kavrik, R. Steinhardt, P. Buragohain, S. Dutta, T. Tronic, S. Clendenning, P. Fischer, E. S. Putna, M. Radosavljevic, M. Metz, U. Avci, *Nat. Commun.* **2023**, 14, 6400.
- [198] Y. Y. Chung, B. J. Chou, C. F. Hsu, W. S. Yun, M. Y. Li, S. K. Su, Y. T. Liao, M. C. Lee, G. W. Huang, S. L. Liew, Y. Y. Shen, W. H. Chang, C. W. Chen, C. C. Kei, H. Wang, H. S. P. Wong, T. Y. Lee, C. H. Chien, C. C. Cheng, I. P. Radu, presented at 2022 International Electron Devices Meeting (IEDM), San Francisco, USA, December **2022**.
- [199] C. J. Dorow, A. Penumatcha, A. Kitamura, C. Rogan, K. P. O'Brien, S. Lee, R. Ramamurthy, C. Y. Cheng, K. Maxey, T. Zhong, T. Tronic, B. Holybee, J. Richards, A. Oni, C. C. Lin, C. H. Naylor, N. Arefin, M. Metz, R. Bristol, S. B. Clendenning, U. Avci, presented at 2022 International Electron Devices Meeting (IEDM), San Francisco, USA, December **2022**.
- [200] T. Y. T. Hung, M. Z. Li, W. S. Yun, S. A. Chou, S. K. Su, E. Chen, S. L. Liew, Y. M. Yang, K. I. Lin, V. Hou, T. Y. Lee, H. Wang, A. Cheng, M. T. Lin, H. S. P. Wong, I. P. Radu, presented at 2022 International Electron Devices Meeting (IEDM), San Francisco, USA, December **2022**.
- [201] C. Tan, M. Amani, C. Zhao, M. Hettick, X. Song, D. H. Lien, H. Li, M. Yeh, V. R. Shrestha, K. B. Crozier, M. C. Scott, A. Javey, *Adv. Mater.* **2020**, 32, 2001329.
- [202] H. Huang, J. Zha, S. Xu, P. Yang, Y. Xia, H. Wang, D. Dong, L. Zheng, Y. Yao, Y. Zhang, Y. Chen, J. C. Ho, H. P. Chan, C. Zhao, C. Tan, *ACS Nano* **2024**, 18, 17293.
- [203] C. J. McClellan, S. V. Suryavanshi, C. D. English, K. K. H. Smithe, C. S. Bailey, R. W. Grady, E. Pop, "2D Device Trends", http://2d.stanford.edu/2D_Trends.html (accessed: July 2024).
- [204] J. Jiang, L. Xu, L. Du, L. Li, G. Zhang, C. Qiu, L. M. Peng, *Nat. Electron.* **2024**, 7, 545.
- [205] A. S. Chou, T. Wu, C. C. Cheng, S. S. Zhan, I. C. Ni, S. Y. Wang, Y. C. Chang, S. L. Liew, E. Chen, W. H. Chang, C. I. Wu, J. Cai, H. S. P. Wong, H. Wang, presented at 2021 IEEE International Electron Devices Meeting (IEDM), San Francisco, USA, December **2021**.
- [206] S. B. Desai, S. R. Madhupathy, A. B. Sachid, J. P. Llinas, Q. Wang, G. H. Ahn, G. Pitner, M. J. Kim, J. Bokor, C. Hu, H. S. Wong, A. Javey, *Science* **2016**, 354, 99.
- [207] Z. Sun, C. S. Pang, P. Wu, T. Y. T. Hung, M. Y. Li, S. L. Liew, C. C. Cheng, H. Wang, H. S. P. Wong, L. J. Li, I. Radu, Z. Chen, J. Appenzeller, *ACS Nano* **2022**, 16, 14942.
- [208] X. Shi, X. Li, Q. Guo, M. Zeng, Y. Han, S. Yan, Y. Wu, *Nano Lett.* **2022**, 22, 7667.
- [209] L. Yang, K. Majumdar, H. Liu, Y. Du, H. Wu, M. Hatzistergos, P. Y. Hung, R. Tieckelmann, W. Tsai, C. Hobbs, P. D. Ye, *Nano Lett.* **2022**, 14.
- [210] D. Lin, X. Wu, D. Cott, D. Verreck, B. Groven, S. Sergent, Q. Smets, S. Sutar, I. Asselberghs, I. Radu, presented at 2021 IEEE International Electron Devices Meeting (IEDM), San Francisco, USA, December **2020**.
- [211] D. Somvanshi, E. Ber, C. S. Bailey, E. Pop, E. Yalon, *ACS Appl. Mater. Interfaces* **2020**, 12, 36355.
- [212] C. C. Chiang, H. Y. Lan, C. S. Pang, J. Appenzeller, Z. Chen, *IEEE Electron. Device Lett.* **2022**, 43, 319.
- [213] W. Liu, J. Kang, D. Sarkar, Y. Khatami, D. Jena, K. Banerjee, *Nano Lett.* **2013**, 13, 1983.
- [214] N. Haratipour, S. J. Koester, presented at 72nd Device Research Conference, Santa Barbara, USA, June **2014**.
- [215] M. J. Mleczko, A. C. Yu, C. M. Smyth, V. Chen, Y. C. Shin, S. Chatterjee, Y. C. Tsai, Y. Nishi, R. M. Wallace, E. Pop, *Nano Lett.* **2019**, 19, 6352.
- [216] D. De, J. Manongdo, S. See, V. Zhang, A. Guloy, H. Peng, *Nanotechnology* **2012**, 24, 025202.
- [217] J. Liu, M. Zhong, X. Liu, G. Sun, P. Chen, Z. Zhang, J. Li, H. Ma, B. Zhao, R. Wu, *Nanotechnology* **2018**, 29, 474002.
- [218] C. M. Corbet, S. S. Sonde, E. Tutuc, S. K. Banerjee, *Appl. Phys. Lett.* **2016**, 108, 162104.
- [219] J. Jiang, L. Xu, C. Qiu, L. M. Peng, *Nature* **2023**, 616, 470.
- [220] L. Li, M. Engel, D. B. Farmer, S. J. Han, H. S. P. Wong, *ACS Nano* **2016**, 10, 4672.
- [221] C. H. Wang, J. A. C. Incorvia, C. J. McClellan, A. C. Yu, M. J. Mleczko, E. Pop, H. S. P. Wong, *Nano Lett.* **2018**, 18, 2822.
- [222] H. Liu, A. T. Neal, Z. Zhu, Z. Luo, X. Xu, D. Tománek, P. D. Ye, *ACS Nano* **2014**, 8, 4033.
- [223] D. He, Y. Wang, Y. Huang, Y. Shi, X. Wang, X. Duan, *Nano Lett.* **2019**, 19, 331.
- [224] T. Li, Z. Zhang, X. Li, M. Huang, S. Li, S. Li, Y. Wu, *Appl. Phys. Lett.* **2017**, 110, 163507.
- [225] N. P. Ong, S. Liang, *Nat. Rev. Phys.* **2021**, 3, 394.
- [226] X. Li, L. Yang, M. Si, S. Li, M. Huang, P. Ye, Y. Wu, *Adv. Mater.* **2015**, 27, 1547.
- [227] S. Natarajan, M. Agostinelli, S. Akbar, M. Bost, A. Bowonder, V. Chikarmane, S. Chouksey, A. Dasgupta, K. Fischer, Q. Fu, T. Ghani, M. Giles, S. Govindaraju, R. Grover, W. Han, D. Hanken, E. Haralson, M. Haran, M. Heckscher, R. Heussner, P. Jain, R. James, R. Jhaveri, I. Jin, H. Kam, E. Karl, C. Kenyon, M. Liu, Y. Luo, R. Mehanadru, et al., presented at 2014 International Electron Devices Meeting (IEDM), San Francisco, USA, December **2014**.
- [228] L. Wu, A. Wang, J. Shi, J. Yan, Z. Zhou, C. Bian, J. Ma, R. Ma, H. Liu, J. Chen, Y. Huang, W. Zhou, L. Bao, M. Ouyang, S. J. Pennycook, S. T. Pantelides, H. J. Gao, *Nat. Nanotechnol.* **2021**, 16, 882.
- [229] L. Liu, C. Liu, L. Jiang, J. Li, Y. Ding, S. Wang, Y. G. Jiang, Y. B. Sun, J. Wang, S. Chen, D. W. Zhang, P. Zhou, *Nat. Nanotechnol.* **2021**, 16, 874.
- [230] K. F. Mak, J. Shan, *Nat. Photonics* **2016**, 10, 216.
- [231] P. V. Pham, S. C. Bodepudi, K. Shehzad, Y. Liu, Y. Xu, B. Yu, X. Duan, *Chem. Rev.* **2022**, 122, 6514.
- [232] X. Zhou, X. Hu, J. Yu, S. Liu, Z. Shu, Q. Zhang, H. Li, Y. Ma, H. Xu, T. Zhai, *Adv. Funct. Mater.* **2018**, 28, 1706587.
- [233] J. Zha, M. Luo, M. Ye, T. Ahmed, X. Yu, D. H. Lien, Q. He, D. Lei, J. C. Ho, J. Bullock, K. B. Crozier, C. Tan, *Adv. Funct. Mater.* **2022**, 32, 2111970.

- [234] G. H. Ahn, A. D. White, H. Kim, N. Higashitarumizu, F. M. Mayor, J. F. Herrmann, W. Jiang, K. K. S. Multani, A. H. Safavi-Naeini, A. Javey, J. Vučković, *Optica* **2023**, *10*, 349.
- [235] J. Yu, H. Mu, P. Wang, H. Li, Z. Yang, J. Ren, Y. Li, L. Mei, J. Zhang, W. Yu, N. Cui, J. Yuan, J. Wu, S. Lan, G. Zhang, S. Lin, *ACS Nano* **2024**, *18*, 19099.
- [236] Y. Hu, X. Song, D. Jia, W. Su, X. Lv, L. Li, X. Li, Y. Yan, Y. Jiang, C. Xia, *Opt. Express* **2023**, *31*, 19804.
- [237] H. Cao, T. Hu, J. Zhang, D. Zhao, Y. Chen, X. Wang, J. Yang, Y. Zhang, X. Tang, W. Bai, H. Shen, J. Wang, J. Chu, *Adv. Sci.* **2024**, 2400018.
- [238] H. Peng, H. Li, E. Guo, T. Zhai, *Adv. Funct. Mater.* **2024**, 2314743.
- [239] J. Xiong, Q. Yu, X. Hou, B. Liu, S. Li, H. Deng, Z. Yang, J. Leng, S. Zhu, Y. Sun, Z. Jiang, N. Huo, J. Wu, P. Zhou, *Adv. Funct. Mater.* **2024**, 2314972.
- [240] P. Wang, Z. Li, X. Xia, J. Zhang, Y. Lan, L. Zhu, Q. Ke, H. Mu, S. Lin, *Small* **2024**, 2401216.
- [241] T. Zheng, M. Yang, Y. Sun, L. Han, Y. Pan, Q. Zhao, Z. Zheng, N. Huo, W. Gao, J. Li, *J. Mater. Chem. C* **2022**, *10*, 7283.
- [242] M. Zhang, Y. Liu, F. Guo, B. Zhang, B. Hu, S. Li, W. Yu, L. Hao, *ACS Appl. Mater. Interfaces* **2024**, *16*, 6152.
- [243] Y. Yang, H. Li, *Adv. Electron. Mater.* **2022**, *8*, 2200094.
- [244] J. Yoon, B. You, Y. Kim, J. Bak, M. Yang, J. Park, M. G. Hahm, M. Lee, *ACS Appl. Mater. Interfaces* **2023**, *15*, 18463.
- [245] M. Panahi-Kalamuei, F. Mohandes, M. Mousavi-Kamazani, M. Salavati-Niasari, Z. Fereshteh, M. Fathi, *Mater. Sci. Semicond. Process.* **2014**, *27*, 1028.
- [246] K. R. Mikeska, M. Lu, W. Liao, *Prog. Photovolt* **2019**, *27*, 1071.
- [247] A. Rogalski, *Opto-Electron. Rev.* **2006**, *14*, 84.
- [248] A. Rogalski, *Opto-Electron. Rev.* **2012**, *20*, 279.
- [249] T. U. Tran, D. A. Nguyen, N. T. Duong, D. Y. Park, D. H. Nguyen, P. H. Nguyen, C. Park, J. Lee, B. W. Ahn, H. Im, S. C. Lim, M. S. Jeong, *Appl. Mater. Today* **2022**, *26*, 101285.
- [250] Z. Luo, H. Xu, W. Gao, M. Yang, Y. He, Z. Huang, J. Yao, M. Zhang, H. Dong, Y. Zhao, Z. Zheng, J. Li, *Small* **2023**, *19*, 2207615.
- [251] H. Yu, Y. Wang, H. Zeng, Z. Cao, Q. Zhang, L. Gao, M. Hong, X. Wei, Y. Zheng, Z. Zhang, X. Zhang, Y. Zhang, *ACS Nano* **2024**, *18*, 17100.
- [252] R. Wang, Z. He, J. L. Wang, J. Y. Liu, J. W. Liu, S. H. Yu, *Nano Lett.* **2022**, *22*, 5929.
- [253] F. Wang, T. Zhang, R. Xie, Z. Wang, W. Hu, *Nat. Commun.* **2023**, *14*, 2224.
- [254] H. W. Guo, Z. Hu, Z. B. Liu, J. G. Tian, *Adv. Funct. Mater.* **2021**, *31*, 2007810.
- [255] H. Fang, W. Hu, *Adv. Sci.* **2017**, *4*, 1700323.
- [256] H. Kind, H. Yan, B. Messer, M. Law, P. Yang, *Adv. Mater.* **2002**, *14*, 158.
- [257] D. Spirito, S. Marras, B. Martín-García, *J. Mater. Chem. C* **2024**, *12*, 2544.
- [258] V. M. Asnin, A. A. Bakun, A. M. Danishevskii, E. L. Ivchenko, G. E. Pikus, A. A. Rogachev, *Solid State Commun.* **1979**, *30*, 565.
- [259] M. D. Moldavskaya, L. E. Golub, S. N. Danilov, V. V. Bel'kov, D. Weiss, S. D. Ganichev, *Phys. Rev. B* **2023**, *108*, 235209.
- [260] A. Sebastian, M. L. Gallo, R. Khaddam-Aljameh, E. Eleftheriou, *Nat. Nanotechnol.* **2020**, *15*, 529.
- [261] J. J. Yang, D. B. Strukov, D. R. Stewart, *Nat. Nanotechnol.* **2013**, *8*, 13.
- [262] F. Zhou, Y. Chai, *Nat. Electron.* **2020**, *3*, 664.
- [263] W. Zhang, B. Gao, J. Tang, P. Yao, S. Yu, M. F. Chang, H. J. Yoo, H. Qian, H. Wu, *Nat. Electron.* **2020**, *3*, 371.
- [264] Y. Chai, *Nature* **2020**, *579*, 32.
- [265] G. Wu, X. Zhang, G. Feng, J. Wang, K. Zhou, J. Zeng, D. Dong, F. Zhu, C. Yang, X. Zhao, D. Gong, M. Zhang, B. Tian, C. Duan, Q. Liu, J. Wang, J. Chu, M. Liu, *Nat. Mater.* **2023**, *22*, 1499.
- [266] Y. Zhou, J. Fu, Z. Chen, F. Zhuge, Y. Wang, J. Yan, S. Ma, L. Xu, H. Yuan, M. Chan, X. Miao, Y. He, Y. Chai, *Nat. Electron.* **2023**, *6*, 870.
- [267] D. Kwak, D. K. Polyushkin, T. Mueller, *Nat. Commun.* **2023**, *14*, 4264.
- [268] C. Liu, H. Chen, X. Hou, H. Zhang, J. Han, Y. G. Jiang, X. Zeng, D. W. Zhang, P. Zhou, *Nat. Nanotechnol.* **2019**, *14*, 662.
- [269] D. Jayachandran, A. Oberoi, A. Sebastian, T. H. Choudhury, B. Shankar, J. M. Redwing, S. Das, *Nat. Electron.* **2020**, *3*, 646.
- [270] T. Li, J. Miao, X. Fu, B. Song, B. Cai, X. Ge, X. Zhou, P. Zhou, X. Wang, D. Jariwala, W. Hu, *Nat. Nanotechnol.* **2023**, *18*, 1303.
- [271] J. Chen, Z. Zhou, B. J. Kim, Y. Zhou, Z. Wang, T. Wan, J. Yan, J. Kang, J. H. Ahn, Y. Chai, *Nat. Nanotechnol.* **2023**, *18*, 882.
- [272] K. Liu, T. Zhang, B. Dang, L. Bao, L. Xu, C. Cheng, Z. Yang, R. Huang, Y. Yang, *Nat. Electron.* **2022**, *5*, 761.
- [273] L. Mennel, J. Symonowicz, S. Wachter, D. K. Polyushkin, A. J. Molina-Mendoza, T. Mueller, *Nature* **2020**, *579*, 62.
- [274] F. Liao, Z. Zhou, B. J. Kim, J. Chen, J. Wang, T. Wan, Y. Zhou, A. T. Hoang, C. Wang, J. Kang, J. H. Ahn, Y. Chai, *Nat. Electron.* **2022**, *5*, 84.
- [275] L. Sun, Z. Wang, J. Jiang, Y. Kim, B. Joo, S. Zheng, S. Lee, W. J. Yu, B. S. Kong, H. Yang, *Sci. Adv.* **2021**, *7*, eabg1455.
- [276] T. Sasaki, K. Ueno, T. Taniguchi, K. Watanabe, T. Nishimura, K. Nagashio, *Small* **2020**, *16*, 2004907.
- [277] T. Sasaki, K. Ueno, T. Taniguchi, K. Watanabe, T. Nishimura, K. Nagashio, *ACS Nano* **2021**, *15*, 6658.
- [278] C. Ma, J. Yan, Y. Huang, C. Wang, G. Yang, *Sci. Adv.* **2018**, *4*, eaas9894.
- [279] M. Walidiya, D. Bhagat, N. R., S. Singh, A. Kumar, A. Ray, I. Mukhopadhyay, *Biosens. Bioelectron.* **2019**, *132*, 319.
- [280] S. Sen, M. Sharma, V. Kumar, K. P. Muthe, P. V. Satyam, U. M. Bhatta, M. Ray, N. K. Gaur, S. K. Gupta, J. V. Yakhmi, *Talanta* **2009**, *77*, 1567.
- [281] T. Siciliano, E. Filippo, A. Genga, G. Micocci, M. Siciliano, A. Tepore, *Sens. Actuators B: Chem.* **2009**, *142*, 185.
- [282] D. Tsiulyanu, I. Stratian, A. Tsiulyanu, H. D. Liess, I. Eisele, *Sens. Actuators B: Chem.* **2017**, *121*, 406.
- [283] D. Tsiulyanu, S. Marian, V. Miron, H. D. Liess, *Sens. Actuators B: Chem.* **2001**, *73*, 35.
- [284] D. Tsiulyanu, S. Marian, H. D. Liess, I. Eisele, *Sens. Actuators B: Chem.* **2004**, *100*, 380.
- [285] M. L. Zhang, H. C. Su, Y. Rheem, C. M. Hangarter, N. V. Myung, *J. Phys. Chem. C* **2012**, *116*, 20067.
- [286] S. Manoharan, K. Krishnamoorthy, V. K. Mariappan, D. Kesavan, S. J. Kim, *Chem. Eng. J.* **2021**, *421*, 129548.
- [287] S. J. Choi, I. D. Kim, *Electron. Mater. Lett.* **2018**, *14*, 221.
- [288] R. W. Dutton, R. S. Muller, *Thin Solid Films* **1972**, *11*, 229.
- [289] K. Okuyama, H. Yamamoto, Y. Kumagai, *J. Appl. Phys.* **1975**, *46*, 105.
- [290] X. Wei, X. Zhang, H. Yu, L. Gao, W. Tang, M. Hong, Z. Chen, Z. Kang, Z. Zhang, Y. Zhang, *Nat. Electron.* **2024**, *7*, 138.
- [291] A. Pezeshki, S. H. H. Shokouh, P. J. Jeon, I. Shackery, J. S. Kim, I. I. K. Oh, S. C. Jun, H. Kim, S. Im, *ACS Nano* **2016**, *10*, 1118.
- [292] S. Wachter, D. K. Polyushkin, O. Bethge, T. Mueller, *Nat. Commun.* **2017**, *8*, 14948.
- [293] Z. Lin, Y. Liu, U. Halim, M. Ding, Y. Liu, Y. Wang, C. Jia, P. Chen, X. Duan, C. Wang, F. Song, M. Li, C. Wan, Y. Huang, X. Duan, *Nature* **2018**, *562*, 254.
- [294] H. Zhang, C. Li, J. Wang, W. Hu, D. W. Zhang, P. Zhou, *Adv. Funct. Mater.* **2018**, *28*, 1805171.
- [295] X. Chen, Y. Xie, Y. Sheng, H. Tang, Z. Wang, Y. Wang, Y. Wang, F. Liao, J. Ma, X. Guo, L. Tong, H. Liu, H. Liu, T. Wu, J. Cao, S. Bu, H. Shen, F. Bai, D. Huang, J. Deng, A. Riaud, Z. Xu, C. Wu, S. Xing, Y. Lu, S. Ma, Z. Sun, Z. Xue, Z. Di, X. Gong, et al., *Nat. Commun.* **2021**, *12*, 5953.
- [296] P. Zhang, X. Hao, Q. Zhou, G. She, J. Chen, X. Zhang, W. Liang, Y. Deng, T. Ning, W. Shi, L. Zhang, C. Zhang, *APL Photonics* **2024**, *9*, 031301.

- [297] L. Liu, T. Li, L. Ma, W. Li, S. Gao, W. Sun, R. Dong, X. Zou, D. Fan, L. Shao, C. Gu, N. Dai, Z. Yu, X. Chen, X. Tu, Y. Nie, P. Wang, J. Wang, Y. Shi, X. Wang, *Nature* **2022**, 605, 69.
- [298] J. K. Huang, Y. Wan, J. Shi, J. Zhang, Z. Wang, W. Wang, N. Yang, Y. Liu, C. H. Lin, X. Guan, L. Hu, Z. L. Yang, B. C. Huang, Y. P. Chiu, J. Yang, V. Tung, D. Wang, K. Kalantar-Zadeh, T. Wu, X. Zu, L. Qiao, L. J. Li, S. Li, *Nature* **2022**, 605, 262.
- [299] K. Liu, B. Jin, W. Han, X. Chen, P. Gong, L. Huang, Y. Zhao, L. Li, S. Yang, X. Hu, J. Duan, L. Liu, F. Wang, F. Zhuge, T. Zhai, *Nat. Electron.* **2021**, 4, 906.
- [300] T. Li, W. Guo, L. Ma, W. Li, Z. Yu, Z. Han, S. Gao, L. Liu, D. Fan, Z. Wang, Y. Yang, W. Lin, Z. Luo, X. Chen, N. Dai, X. Tu, D. Pan, Y. Yao, P. Wang, Y. Nie, J. Wang, Y. Shi, X. Wang, *Nat. Nanotechnol.* **2021**, 16, 1201.
- [301] J. S. Lee, S. H. Choi, S. J. Yun, Y. I. Kim, S. Boandoh, J. H. Park, B. G. Shin, H. Ko, S. H. Lee, Y. M. Kim, Y. H. Lee, K. K. Kim, S. M. Kim, *Science* **2018**, 362, 817.
- [302] W. Pacuski, M. Grzeszczyk, K. Nogajewski, A. Bogucki, K. Oreszczuk, J. Kucharek, K. E. Połczyńska, B. Seredyński, A. Rodek, R. Bożek, T. Taniguchi, K. Watanabe, S. Kret, J. Sadowski, T. Kazimierczuk, M. Potemski, P. Kossacki, *Nano Lett.* **2020**, 20, 3058.
- [303] C. R. Dean, A. F. Young, I. Meric, C. Lee, L. Wang, S. Sorgenfrei, K. Watanabe, T. Taniguchi, P. Kim, K. L. Shepard, J. Hone, *Nat. Nanotechnol.* **2020**, 5, 722.
- [304] X. Shang, L. Wan, L. Wang, F. Gao, H. Li, *J. Mater. Chem. C* **2022**, 10, 2400.
- [305] Y. Yang, R. C. da Costa, M. J. Fuchter, A. J. Campbell, *Nat. Photonics* **2013**, 7, 634.
- [306] Q. Liu, Q. Wei, H. Ren, L. Zhou, Y. Zhou, P. Wang, C. Wang, J. Yin, M. Li, *Nat. Commun.* **2023**, 14, 7179.
- [307] W. M. He, J. Zha, Z. Zhou, Y. J. Cui, P. Luo, L. Ma, C. Tan, S. Q. Zang, *Angew. Chem., Int. Ed.* **2024**, 63, 202407887.



Jiajia Zha received his B.S. degree in applied physics and M.S. degree in atomic and molecular physics from Southeast University in 2017 and Fudan University in 2020, respectively. He then moved to the Departments of Electrical Engineering and Materials Science and Engineering of the City University of Hong Kong, where he completed his Ph.D. study under the supervision of Prof. Chaoliang Tan in 2023. Since then, he has been working as a Research Fellow in the same group. His research interests focus on the device design/fabrication based on van der Waals semiconductor thin films.



Chaoliang Tan is currently an assistant professor in the Department of Electrical and Electronic Engineering at The University of Hong Kong (HKU). He received his Ph.D. from Nanyang Technological University. After working as a Research Fellow in the same group for about one year, he then worked as a Postdoctoral Researcher at the University of California-Berkeley for two years. He was an assistant professor at the City University of Hong Kong before joining HKU. His research focuses on 2D materials for electronics and optoelectronics, and structural engineering of layered materials for biomedicine, etc.